Dissertation zur Erlangung des Doktorgrades
der Fakultät für Chemie und Pharmazie
der Ludwig-Maximilians-Universität München

Bioresponsive nanocarriers for targeted intracellular delivery of proteins and peptides

Ruth Elisabeth Johanna Röder

aus

Starnberg, Deutschland

2016

Erklärung:

Diese Dissertation wurde im Sinne von § 7 der Promotionsordnung vom 28. November 2011 von Herrn Prof. Dr. Ernst Wagner betreut.

Eidesstattliche Versicherung

Diese Dissertation wurde eigenständig und ohne unerlaubte Hilfe erarbeitet.

München, 29.12.2016

……

Ruth Röder

Dissertation eingereicht am: 29.12.2016

1. Gutachter: Prof. Dr. Ernst Wagner

2. Gutachter: Prof. Dr. Stefan Zahler

Mündliche Prüfung am: 07.02.2017

Table of Contents

1 Introduction

Sections (1.1-1.3) have been partly adapted from: Ruth Röder and Ernst Wagner, "Sequence-defined shuttles for targeted nucleic acid and protein delivery", Therapeutic Delivery (2014) 5(9), 1025–1045.

1.1 Novel molecular therapeutics: in search of the perfect delivery strategy

The rapid progress in medicine is always calling for more effective drugs, which provide satisfactory therapeutic benefits without showing adverse effects. Nucleic acid therapy as well as protein transduction are novel strategies to treat diseases at the point of their very origin. Within the past few years, these kinds of molecular therapies have emerged as very promising treatments for life-threatening diseases resulting from defective genes. With 65% of all ongoing clinical gene therapy trials worldwide, cancer is by far the most common disease treated by gene therapy, followed by monogenic, cardiovascular and infectious diseases (see [1] and The Journal of Gene Medicine Clinical Trial site www.abedia.com/wiley). In July 2012 the first gene therapy product, Glybera (UniQure), was recommended for approval in the EU. It is an adeno-associated viral vector, which expresses lipoprotein lipase in the muscle tissue, to treat patients with severe lipoprotein lipase deficiency [2]. The inherent problems associated with gene therapy include the lack of efficient delivery, the risk of triggering immune responses and the risk of uncontrolled genetic changes, although a lot of already approved drugs hold the same risks [1]. Even though peptides, proteins or nucleic acids are not able to cross cell membranes and enter the intracellular space, this obvious restriction in delivery has been turned into a possible advantage through the development of a number of specific cell targeted shuttles for nucleic acid and protein delivery. Therefore many different synthetic carriers have been designed to overcome the various delivery hurdles. Based on the long experience in liposome technology, lipid-based gene carriers have been developed [3-6]. Cationic lipids of medium and low molecular weight, well accessible in high purity by synthetic routes, are the basis. Alternatively, cationic macromolecules with inherently high binding capacity for nucleic acids were evaluated. Polymers such as polyamidoamine (PAMAM) and polyethylenimine (PEI) are among the most widely investigated carriers for pDNA delivery [7]. PEI, which

has been introduced by the lab of Behr in 1995, is probably the most prominently utilized polymer, based on its relatively high transfection efficiency [8]. It is either used as branched PEI or the more defined linear PEI. To overcome its high toxicity, succinylated PEI [9] or various conjugates can be used. PEI as well as PAMAM dendrimers, which were first reported for transfection by Haensler and Szoka [10], have a very high amine density, but only 15–20% of the amines are protonated under physiological pH. This leads to a very efficient endosomal release due to high buffering capacity, cationization and endosomal membrane lysis (Figure 1b, proton sponge hypothesis) [7, 11, 12]. Although these carriers have been converted by modifications and conjugation into more advanced delivery systems, their most crucial drawback is their inherent polydispersity and heterogeneity, especially with regard to their lack of specific modification sites. Particularly with regard to clinical development, it is important to have chemically precise and well-defined carriers, enabling reproducible manufacturing. A precise chemical structure is required for providing the carrier with defined functions, and it is essential for generating good predictions and correlations between chemical and resulting biological properties. Nature has already provided excellent examples of delivery systems with highly defined macromolecular structures displaying multiple functions in precise positions: currently, the most advanced systems are viral vectors. The most prominent vector systems used in numerous clinical studies are adeno-associated virus systems [2, 13, 14], retroviral [15] and lentiviral vectors [16]. Therapeutic nucleic acids replace most of the virus genome, and the virus proteins (often together with lipid envelopes) mediate the delivery process [17]. However, various disadvantages are also associated with viral vectors; they are limited in their capacities for cargo loading, they carry the risk of insertional mutagenesis, can have a high inflammatory potential and optimization is caught within the limits of their biosynthesis using proteinaceous amino acid sequences [7, 17]. Nevertheless, virus-based delivery systems provide proof that highly efficient sequence-defined macromolecular carriers are reality. The biological clue has been to assemble small units in a defined sequence. Utilizing precise solid-phase-assisted synthesis, researchers recently started to mimic such procedures by designing sequence-defined carriers putting standard building blocks (amino acids, lipids, nucleotides) or artificial building blocks into sequence.

1.2 Nucleic acid versus protein delivery

Delivery requirements differ for the individual molecular therapeutics: pDNA, siRNA or intracellularly active proteins. The different delivery pathways are shown in Figure 1a.

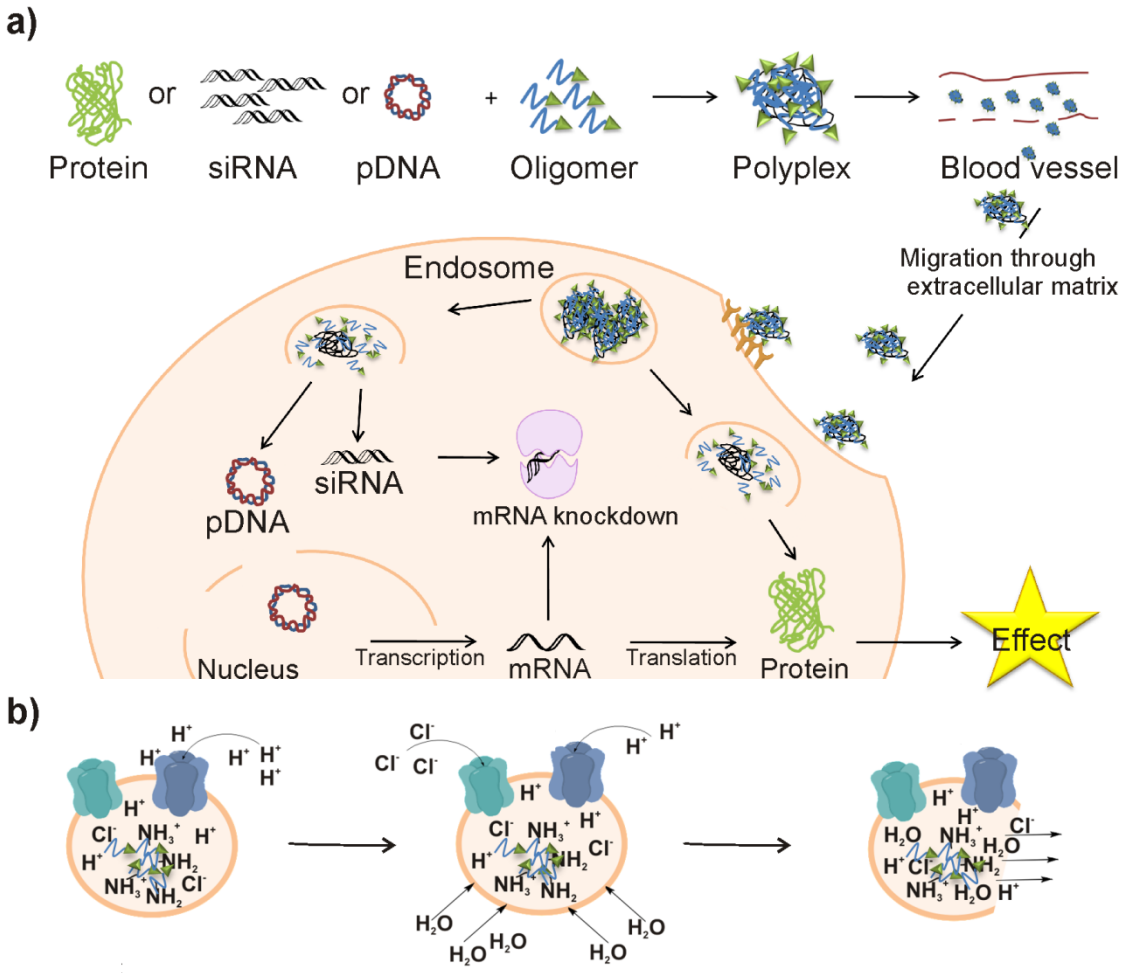

Figure 1: The challenging way into the cell –protein versus nucleic acid delivery. a) Both proteins and nucleic acids have to form stable complexes (polyplexes) with polymers or defined oligomers, including PEG shielding and targeting ligand. After intravenous injection, polyplexes have to extravasate into the tissue and migrate through the extracellular matrix. They are recognized by their specific receptor and endocytosed into the cell. After endosomal escape, siRNAs are processed in the cytosol. The guide strand is bound to the Argonaute protein and the passenger strand is discarded. Target mRNA is cleaved (middle). In contrast, pDNA has to be imported into the nucleus (left), transcribed and translated into a protein to interact with its molecular target. Protein delivery (right) is the most straightforward process of the three. After endosomal escape, the protein has to find its molecular target to induce signaling cascades, leading to the desired effect (right). b) Endosomal escape can be explained by the proton sponge hypothesis: protonation of the oligomer causes increased influx of chloride counterions and H_2O, leading to osmotic pressure, interaction of cationic oligomer residues with endosomal membrane and rupture of the endosome [17-19].

As both pDNA and siRNA are double- stranded nucleic acids with anionic phosphodiester backbones, one would assume that their deliveries require similar elements. Both types of nucleic acids are highly negatively charged, which allows

electrostatic interactions with positively charged delivery agents. In reality, very significant differences for optimum transfer have been observed [20]. First of all, their different structural, chemical and biological properties need to be considered. Due to the much smaller size of siRNA, it shows far less electrostatic interaction with polycations. Therefore special attention has to be paid to the polyplex stability. In terms of hydrolysis, siRNA due to its 2′-hydroxy group is more fragile than pDNA [21]. Moreover, RNA is more prone to degradation by nucleases, which can be avoided through the introduction of stabilizing modifications such as 2′-fluorine and 2′-methoxy. These modifications do not only improve the stability of siRNA, but they can also reduce off-target effects and even improve the specificity for the target mRNA [20, 22]. When introduced into the cytosol of cells, siRNAs are processed by natural mechanisms into the so-called RNA-induced silencing complex. The guide strand, where the first nucleotides comprise the seed sequence and initialize binding to the target mRNA, is bound to the Argonaute protein and the passenger strand is discarded. Most commonly, mRNA and siRNA are perfectly matching in sequence, leading to cleavage of target mRNA in the presence of the catalytic Argonaute protein Ago2. If not, such as in the case of endogenous miRNAs, silencing can also be achieved via pre- or post initiation translational repression and deadenylation, followed by degradation of the mRNA [23]. Compared to the cytosolic delivery of siRNA, pDNA has to overcome another obstacle after endosomal escape: the import into the nucleus. This presents a limiting factor for transfection as the cytosol impedes the migration of DNA, and the nuclear pore presents an additional barrier for larger nucleic acids. Passive nuclear uptake of pDNA can only take place during cell division. If not sufficient, an active transport mechanism is needed. Coupling of DNA to short peptide sequences such as nuclear localization signals (NLS) has provided only limited success; nuclear entry remains a major limitation [20, 24]. After successful delivery to the nucleus, DNA still presents a prodrug. The delivered pDNA first has to be transcribed into mRNA and translated into the active corresponding protein before it can exhibit its effect. The obstacles of nuclear delivery and transcriptional and translational processing can be overcome by the transduction of bioactive proteins (Figure 1a right). The delivery of therapeutic proteins is regarded as safe because it does not introduce potentially recombinogenic nucleic acid material [1, 25]. In comparison to the delivery of nucleic acids, the delivery of proteins is the most straightforward way to address diseases which result from missing or

mutated forms or misfolded proteins. Regarding siRNA transfer, cytosolic delivery of intact and bioactive molecules is the primary goal. As opposed to nucleic acid cargos, simple electrostatic complexation cannot generally be applied. In addition, proteins display far more variation in biophysical properties than the rather uniform oligonucleotide drugs. Therapeutic protein molecules usually have to be covalently modified, to ensure a robust binding with the carrier in the first steps of their delivery. However, at their intracellular site of action, they must disassemble from the carrier. Thus, bioreversible modifications are in the focus of delivery studies.

1.3 Sequence-defined delivery systems for the delivery of proteins

Protein therapeutics are pharmaceutically well established in applications where their sites of action are targeted to the extracellular environment. In vaccination approaches, pharmaceutical proteins are required to act also intracellularly: specifically immune cells must internalize and process the provided protein antigens. Apart from desired uptake by immune cells upon vaccination, there is an enormous number of intracellular molecular targets where an active, targeted intracellular delivery process termed ‘protein transduction’ would tremendously broaden the scope of therapeutic protein application. Various strategies such as virus like particles [26], silica nanoparticles [27, 28], nanocapsules [29], charge-conversional polyion complex micelles [30-32], liposomal carriers [33], or cell penetrating peptides [34-36] have been applied to deliver therapeutic proteins. Although efficient, most of these carriers are not sequence-defined. The next sections will describe different sequence-defined protein delivery agents in more detail.

1.3.1 Protein delivery using cell penetrating peptides

Based on the knowledge of existing natural intracellular protein delivery, the most widely investigated tools are cell penetrating peptides (CPPs) [37-39]. CPPs are water-soluble, polybasic and/or amphipathic peptides which are usually less than 30 amino acids in length with a net positive charge at physiological pH [40]. A prominent field in which CPPs have been applied is the generation of induced pluripotent stem cells (iPS). Kim *et al.* [41] as well as Yu *et al*. [42] succeeded in efficient delivery of

four reprogramming factors Oct4, Sox2, Klf4 and c-Myc into human newborn fibroblasts or chicken embryonic stem cells resulting in successful maintenance and differentiation of these cells.

Liu *et al.* [43] presented an application of protein delivery to circumvent the delivery of pDNA or mRNA in a case where it has been proven to be quite challenging, by showing the delivery of functional transcription activator-like effector nucleases (TALENs) into cells using the commercially available CPP (Npys)-$(D\text{-}Arg)_9$. A disadvantage of using CPPs might be that the irreversible modification of a protein with a CPP domain can disturb its tertiary structure leading to a permanent inactivation, especially in the case of enzymes. To overcome this problem, Dowdy and co-workers [44] designed a system where they developed a pH-sensitive CPP. In this approach they made use of the fact that thousands of recombinant proteins are carrying a hexahistidine (H_6)- tag for purification. A fact on which will also be played on in the second part of this thesis (Chapter 3.2). At pH >6, in the presence of a metal ion, a coordinate bond can be formed between two imidazole rings on adjacent histidine residues and one molecule of nitrilotriacetic acid (NTA). In the work of June *et al.* [44], the coupling of the CPP TAT with three NTAs enables the pH-sensitive coupling of H_6-tagged proteins or other H_6-tagged macromolecular cargos to any NTA-tagged CPP. Applying this system they showed the transduction of H_6-β-Galactosidase, as well as H_6-Cre recombinase into CHO reporter cells, as well as the *in vivo* delivery, upon intravenous injection of Cre recombinase in ROSA26 loxP-Stop-loxP luciferase mice [44].

A quite novel alternative approach is the utilization of sequence-defined oligoaminoamides. The development of these oligomers will be further described in the next section.

1.3.2 Development of sequence-defined oligomers

Due to the various extra- and intracellular barriers, a defined carrier has to accomplish numerous activities. One strategy to design oligomer-based carriers meeting all the above-described requirements involves the use of solid-phase supported synthesis, thus putting the smaller delivery subdomains into defined precise sequences. It is a very elegant approach to assemble sequence-defined and therefore also activity-defined, macromolecular carriers. In contrast to standard

peptides, artificial non amino acid building blocks are also incorporated. Polyamidoamines (PAAs) were usually generated through polyaddition reactions, leading to polydisperse products, making the design of precise multifunctional oligomers difficult. To circumvent this problem, Hartmann *et al.* applied solid-phase supported synthesis to generate sequence-defined multifunctional PAAs [45]. Using this method, the synthesis of larger oligomers failed, due to unexpected cross-links which block further oligomer extension [46]. Schaffert *et al.* introduced novel artificial Fmoc/Boc-protected amino acids which contain short defined repeats of the diaminoethane motif [46] (Figure 2a). Like PEI, this motif provides protonable amines for proton sponge capacity, which are considered to be responsible for the high transfection efficiency of PEI [47]. Using these building blocks, linear polycations, with or without modification as well as branched structures were synthesized.

Confirming this strategy, oligomers synthesized with full control of their chemical composition and structure resulted in equally high transfection levels as those achieved with PEI. In addition, these medium-sized precise carriers displayed far higher biocompatibility than PEI both *in vitro* and *in vivo* [48]. Development of novel building blocks for such strategies is an interesting area of ongoing research. For example, Wojcik *et al.* [49] introduced a new set of building blocks, allowing separate building of the main and side chain leading to asymmetrically branched PAAs [49]. Martin *et al.* [47] reported the first description of the synthesis of PEG-shielded, sequence-defined monodisperse PAAs containing targeting ligands [47]. The schematic structure of a sequence-defined oligomaminoamide carrier is depicted in Figure 2b. Carriers comprise different diaminoethane building blocks and α,ε-amidated lysines as branching points. Optionally histidines as protonable buffering units or oleic acids to enhance endosomal escape, as well as cysteines which are supposed to serve as bioreversible crosslinkage of oligomers, to stabilize the polyplexes [50]. Ligand-PEG can be included as functional shielding and cell targeting domain and glutamic acid or succinic acid as non-functional subunits (Figure 2).

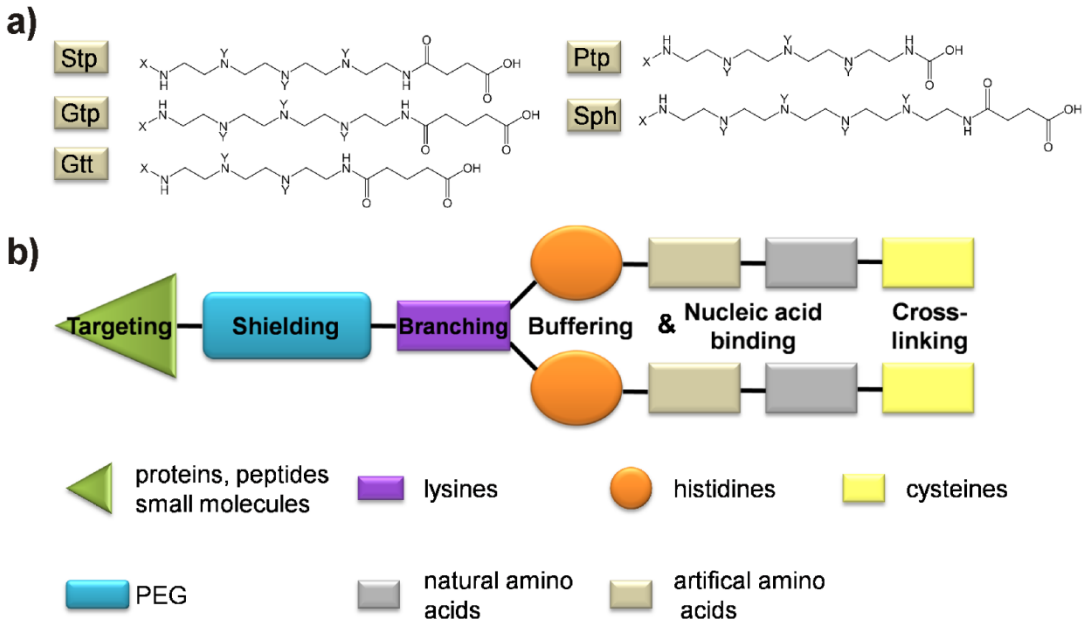

Figure 2: Building blocks and general structure of a sequence-defined oligomer. a) Succinoyl tetraethylene pentamine (Stp) (three protonatable amines within an oligomer chain); glutaroyl tetraethylene pentamine (Gtp) (three protonatable amines), glutaroyl triethylene tetramine (Gtt) (two protonatable amines), phthaloyl tetraethylene pentamine (Ptp) (three protonatable amines), succinoyl pentaethylene hexamine (Sph) (four protonatable amines) [46, 48, 51]. b) Schematic structure of a sequence-defined oligoaminoamide carrier, including different units for targeting such as proteins, peptides, small molecules (green), shielding such as polyethyleneglycol (PEG) (blue), branching such as lysines (purple), buffering and nucleic acid binding such as histidines, and other natural or artificial amino acids (orange, brown, grey) and cross-linking such as cysteines (yellow).

1.3.3 Delivery of proteins using sequence-defined oligomers

Polyplexes built out of oligomers and nucleic acids are usually held together by electrostatic interactions. As proteins exhibit a much lower charge density than nucleic acids, oligomers usually have to be covalently attached. The protein can be coupled bioreversibly either through an acid labile or a reducible disulfide linker to a sequence-defined carrier. Maier *et al.* [52] modified amino groups of nlsEGFP (enhanced green fluorescence protein containing a nuclear targeting sequence, NLS) as well as β-Galactosidase with N-succinimidyl 3-(2-pyridyldithio)propionate (SPDP), followed by covalent attachement of a cationic three-arm transfection oligomer (***386***) to the activated thiol groups of the linker through a disulfide bond. Successful transduction and effective delivery to the nucleus in 3T3 fibroblasts and Neuro2A cells could be shown for ***386***-SS-nlsEGFP. β-Galactosidase-SS-***386***, was able to hydrolyze X-Gal or C12-FDG, which led to fluorescence after transduction into Neuro2A. The same approach was applied by Zhang *et al.* [53] leading to the effective folate receptor dependent delivery of active RNAse and GFP using a three-

arm oligomer (***729***) including oleic acid to enhance endosomal escape, PEG as shielding domain and folate to enable receptor dependent cellular uptake. A drawback of this approach is that the SPDP linker still results in thiol-modified amino groups after cleavage. To overcome this problem, and to achieve an acid labile release, the azidomethyl-methylmaleic anhydride (AzMMMan) linker was designed [54]. Again, amino groups of nlsEGFP, β-Galactosidase and also human serum albumin were modified and acidic- and time dependent release was displayed for covalent coupled Dye or PEG. Successful transduction and effective delivery to the nucleus in human cervical cancer cells, HeLa, could be shown for ***386***-AzMMMan-nlsEGFP compared with irreversible thioether linkage using succinimidyl 4-(N-maleimidomethyl)cyclohexane-1-carboxylate (SMCC) [54]. A similar pH-sensitive system for protein delivery was developed by the group of Kataoka. They used charge-conversional polyion complex (PIC) micelles to deliver proteins. Here, the charge density of proteins is increased to result in more stable PIC [30]. Positively charged lysines of IgG or cytochromeC are converted into negatively charged carboxylic groups by modifying them with citraconic acid amide (Cit) or cis-aconitic acid amide (Aco) to form stable PIC micelles with cationic block copolymers such as PEG–poly[N-{N'- (2-aminoethyl)-2-aminoethyl aspartamide] (PEGpAsp(DET)). After internalization into the cells, the Cit and Aco amide linkages rapidly hydrolyze at the endosomal pH of 5.5, leading to dissociation of the PIC micelle. The original protein is regenerated, releasing the cationic block copolymer, which induces the pH-dependent destabilization of the endosomal membrane to aid the endosomal escape of the protein into the cytoplasm [30, 31]. This approach also functions in reverse, by forming PICs containing a highly negatively charged block copolymer and a highly positively charged protein such as lysozyme [55].

1.4 Nanobodies as therapeutic agents or imaging tools

Nanobodies (Figure 3) are single domain- antibody fragments (V_{HH}) derived from heavy-chain only camelid antibodies (HcAb) [56]. HcAbs which, compared to conventional IgG antibodies, are devoid of the light chains, were first discovered in the 1990s [57] in *Camelidae* (Bactrian camels, dromedaries, vicugnas, and lamas) [58].

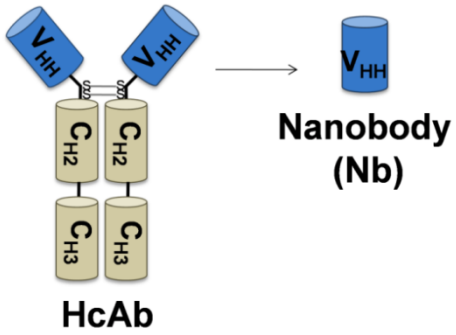

Figure 3: Structure of a nanobody. Camelide heavy chain Antibody (HcAb), which compared to a normal antibody lacks the light chain and the C_{H1} domain and comprises a single antigen binding domain the V_{HH} domain. A Nanobody (Nb) is derived from HcAb and consists of one V_{HH} domain only. Adapted from [59].

Especially with regard to their possible use as biopharmaceuticals [60, 61] or imaging tools [62-64], nanobodies have significant advantages compared to standard antibodies. They can be easily screened for affinity and specificity; due to their compact, single domain structure, they stay chemically active in the reducing environment of the cell; they can be produced in prokaryotic systems in high yield and be easily chemically and genetically modified [65-67]. Additionally, due to their small size (15kDa), nanobodies can better diffuse through tissues or also intracellularly across nuclear pores, and also bind and inhibit targets such as enzymes which are addressed by standard antibodies to a far lesser extend [68, 69]. Until today, nanobodies have been used in a broad field of diverse applications. Rothbauer *et al.* [70] described on the one hand the use of an immobilized GFP binding nanobody (GBP) for the generation of a GFP-nanotrap, enabeling a fast and efficient isolation of GFP fusion proteins as well as their interacting factors. On the other hand they also showed that GBP can be fused with structural proteins to recruit GFP fusion proteins and interacting factors at defined regions in living cells [70]. The usage of nanobodies for a different application has been shown by Heukers *et al*.

[71]. They used albumin nanoparticles decorated with anti hepatocyte growth factor receptor (HGFR, Met) nanobodies to interfere with the Met/HGF pathway for anticancer therapy.

Ekstrand *et al.* [72] used GBPs to tag ribosomes, and engineered this systems to selectively capture translating mRNA from neurons retrogradely labeled with GFP. Like that, they were able to profile neurons projecting to the nucleus accumbens. Leduc *et al.* [73] modified gold nanoparticles with GBP to enable tracking of proteins using photothermal imaging. They were able to label GFP-proteins in very crowded environments such as cytoskeletal structures and adhesion sites both *in vitro* and in live cells. The use of GBP to mediate knockout of fluorescent fusion proteins, by manipulating the ubiquitine pathway, has been described by Caussinus *et al*. [74]. Last but not least, nanobodies have already been used in various clinical applications such as Caplacizumab for acquired thrombotic thrombocytopenic purpura, which was the first nanobody to enter phase III studies [75]. Ozoralizumab and ATN-192 were developed by Ablynx for the therapy of autoimmune diseases with initial focus on rheumatoid arthritis. Ozoralizumab also called ATN-103 is a humanized trivalent, bispecific Nb. It binds with high affinity to Tumor necrocis factor (TNF). ATN-192 with which a Phase I clinical trial was already completed is the PEGylated form of ozoralizumab [76].

1.5 Metal-organic frameworks (MOFs)

Porous coordination polymers or metal-organic frameworks (MOFs) are a relatively new class of nanomaterials which have been discovered in 1989 by Robson and his group [77]. MOFs consist of metal ions or secondary building units (SBUs) or metal oxide clusters, which are coordinatively connected by organic linkers to create porous three-dimensional crystalline frameworks (Figure 4) [78, 79].

These first MOFs consisted of Cu(I) centers and were linked with 4,4′,4″,4‴-tetracyanotetraphenylmethane adopting a tetrahedral geometry [80]. Compared to silica and zeolithes, metal clusters and organic linkers can be varied almost indefinitely, providing innumerable possibilities and great flexibility for creating different well-defined MOF nanoparticles (NPs). Their ultra high porousity together with the exceptional big internal surface area and the variability in design verify their various fields of applications, such as luminescence [81], adsorption and gas storage

[82, 83], catalysis [84] or drug delivery [85, 86]. MOFs can be synthesized via different synthesis methods. Examples are hydrosolvothermal, microwave assisted, atmospheric pressure and reflux, ultrasonic and mechanochemical conditions or reverse phase microemulsions [85, 87].

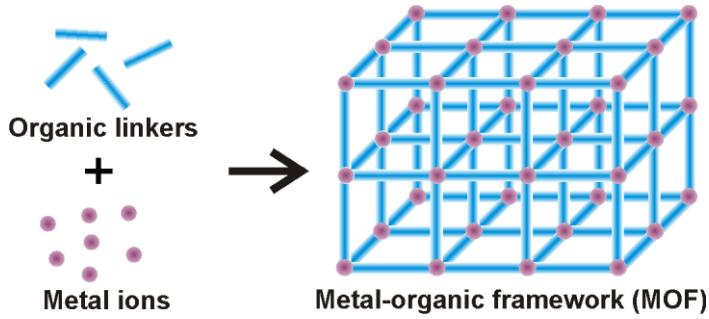

Figure 4: Molecular composition of metal-organic frameworks (MOFs). MOFs consist of metal ions (red) and an organic linker (blue) to create porous three-dimensional crystalline frameworks. Adapted from [158].

Generally MOFs can be built out of two different kinds of linkers. Exogenous linkers such as imidazole, trimesic- or terephtalic acic do not intervene in the body cycle and should be excreted after administration. Here, an advantage depicts the use of already functionalized linkers so-called presynthetic modification, where the linker is altered before the MOF formation [88]. In contrast, the postsynthetic modification process describes the use of already synthesized frameworks with presynthetic modified linkers to which molecules with corresponding functional groups can be introduced; e.g. modification of amino functionalized benzene-1,4-dicarboxylate in MIL-101(Al) with peptide coupling agents [89] or introducing metal-coordinating ligands into MOFs [90]. Endogenous linkers are a constitutive part of the body composition and can be reused after administration, such as fumaric acid in the Krebs cycle decreasing the risk of side effects [85].

The controlled functionalization of the surface of NPs has become more and more popular in recent years. As the surface-to-volume ratio of NPs is quite high, the attachment of functional molecules to the surface is fundamental to control overall properties [91]. Especially in the field of biomedicine, surface modification is of great importance to inhibit agglomeration and to include specifc targeting ligands [92, 93]. Surface modification can occur via a self assembly process; examples are micelle, liposome or polymerosome formation of amphiphilic compounds [94-97], ionic complex formation [98, 99], cyclodextrin-adamantane host-guest interaction [100,

101] and gold-sulfur interaction [102-106]. Another possibility is the covalent modification which has amongst others been described for sequence-defined polyplexes [107, 108], MOF NPs [109-111], silica NPs [112, 113], carbon nanotubes [114], or liposomes [115, 116].

1.5.1 MIL-88A

MIL-88A (MIL stands for Materials from Institute Lavoisier) MOF NPs have a hexagonal symmetry. They correspond to a coordination polymer built from oxocentered trimers of iron (III) octahedra connected by hydrophilic fumarate anions that delimit a three dimensional pore system ($\phi \sim 5–7$ Å) [117, 118]. They consist of fumaric acid as organic linker, which has also been used as food additive, and Fe^{3+} as metal ion.

Until today, the better part of applications of MIL-88A lies in their usage as catalysts. MIL-88A has very high swelling capacities (above 80%) upon exposure to polar solvents. This property is very useful in photocatalytic reaction. Through this large volume swelling, the reactants can be easily adsorbed onto the reaction sites, followed by the redox reaction and desorption of the reaction products [119]. Li *et al.* [120] applied MIL-88A NPs as a heterogenous persulfat catalyst, for the decolorization of the organic pollutant, Rhodamin B, in water, proofing that decolorization does not simply occur via adsorption of Rhodamin B to MIL-88A, but just after the MOF induced activation of persulfate generating sulfate radicals to degrade Rhodamin B [120].

The use of iron based MOFs as potential drug delivery and imaging tool was amongst others investigated by Horcajada *et al.* [121]. First, anticancer or antiviral drugs (busulfan, azidothymidine triphosphate, cidofovir) as well as some cosmetic molecules, such as caffeine (liporeductor), urea (hydrating agent), benzophenone 3 and benzophenone 4 (UVA and UVB filters) were entrapped in different non-toxic iron(III) carboxylate MOFs and for biological applications, the surface was coated with PEG. Long-term stability studies revealed a major degradation of MIL-88A only after 7 days at 37 °C. In *vitro* and in *vivo* toxicity studies showed no toxicity even after prolonged exposure. Further investigations in Wistar female rats revealed that MIL-88A can also be used as contrast agents. Upon PEGylation of MIL-88A MOF NPs,

slightly higher relaxivity values were obtained compared to the usage of non-PEGylated ones [121].

1.5.2 HKUST-1

HKUST-1 (HKUST stands for Hong Kong University of Science and Technology) was among the first synthesized and characterized MOFs in 1999 [122]. It is one of the few MOFs that is already produced by BASF at large scale and is commercially available (Basolite C300) [122]. This MOF forms face-centered-cubic crystals that contain an intersecting three-dimensional (3D) system of large square-shaped pores (9 Å by 9 Å) [122], with a thermal stability up to 240 °C. HKUST-1 were the first open metal site MOFs to be characterized [85]. Compared to the two other MOF NPs used in this work, HKUST-1 is assembled using trimesic acid as an organic linker.
HKUST-1 is one of the best verified MOFs for hydrogen adsorption and storage [123]. Taking advantage of its great adsorption abilities, HKUST-1 MOF NPs can also be used to remove pollutants from water. Conde-González *et al.* successfully investigated their usage as adsorbent to remove silver nanoparticles from water [124].
In terms of drug delivery, Ke *et al.* reported the encapsulation and delivery of the hydrophobic anticancer drug, Nimesulide. They used a magnetic nanocomposite material, prepared by incorporating Fe_3O_4 nanorods in HKUST-1 nanoparticles [125]. Furthermore HKUST-1 is one of the MOF NPs which has the best NO absorption abilities. NO loaded HKUST-1 NPs were able to completely inhibit antiplatelet aggregation in human platelet rich plasma, while HKUST-1 NPs alone did not exhibit any significant effect. Another purpose NO loaded HKSUT-1 NPs can be used for is their antibacterial effect, which could be shown in methicillin resistant *Staphylococcus auereus*, *Pseudomonas aeruginosa* and *Clostridium Difficile* [85].

1.5.3 Zr-*fum*

The Zr-*fum* MOF NPs used in this work are composed of $ZrCl_4$ and, just as MIL-88A, of fumaric acid as a linker [126]. As a modulator formic acid is used. Therefore all components are naturally occurring molecules, thus their usage for biological applications is obvious.

Until today, a variety of different Zr-MOFs have been synthesized. The first were University of Oslo-66 (UiO-66) (with terephtalate as a linker), UiO-67 (with biphenyl dicarboxylate as a linker) and UiO-68 (with terphenyl dicarboxylate as a linker) [127, 128].

In comparison to these MOFs the crystal structure of the Zr-*fum* MOF NPs used in this work can be derived from UiO-66. Zr-*fum* NPs have a primitive cubic lattic with the space group $Pn\bar{3}$ compared to a face-centered one of UiO-66. This stems from the nature of its linker, fumaric acid. The MOF features stability towards aqueous solutions and is stable up to 260 °C. The Zr-*fum* MOFs used in this work were synthesized according to the protocol described by Wißman *et al*. [129], but instead of performing the synthesis in DMF, it was done in water.

To date, Zr^{4+} based MOF NPs have been used in various applications such as the detection and removal of antibiotics and organic explosives in water [130] or also in Photo- [131, 132], Electro- [133], or Lewis acid catalysis [134, 135].

The application of MOFs in the field of drug delivery is difficult as they often exhibit poor chemical and thermal stabilities. In contrast to that, the above described Zr-MOFs are considered to be ideal candidates for drug delivery. Zhu *et al.* [136] for example used UiO-66 to deliver alendronate into cancer cells, leading to growth inhibition after pH dependent release. Fillippousi *et al.* [137] also investigated UiO-66 and UiO-67 for their use as anticancer drug carriers. They adsorbed hydrophobic taxol and hydrophilic cisplatin onto/ into MOFs, which were then encapsulated in biodegradable polymeric matrix (modified poly(ε-caprolactone) with d-α-tocopheryl polyethylene glycol succinate) in order to improve solubility, reduce toxicity and prepare sustained release formulations. The polymer coated drug loaded MOFs exhibited better antitumor activity compared to the free drug solutions [137].

1.6 Aims of the thesis

1.6.1 Delivery of nanobodies for imaging of target proteins

Nowadays, nanobodies are being used in various fields of applications, such as imaging of target proteins or as biopharmaceuticals. A drawback of their use is the access of intracellular molecular targets only upon fixation and permeabilization of cells. The transduction of functional nanobodies into living cells would therefore be a great advancement for functional biological or therapeutic applications. Besides, also labeling of proteins, prior to their delivery would be possible, broadening the scope of dyes which can be used from intracellular expressed fluorescent proteins to any desired marker.

The first aim of this thesis was to establish a system for the efficient delivery of a model nanobody into living cells. A broad screening was to be conducted evaluating different targeted and non-targeted sequence-defined oligoaminoamide carriers from our lab, for their potential to efficiently transduce a GFP binding nanobody into living HeLa_ PCNA-GFP cells.

The second aim was to investigate molecular details of the involved nanoparticles formed by the nanobody and selected oligoaminoamides.

The third aim was to investigate if this approach works in various cell lines and can be extended to other nanobodies. Therefore the delivery of a lamin binding nanobody into KB_*wt* cells had to be evaluated.

As the fourth aim the potential of the newly developed nanobody delivery system for the visualization of intracellular targets in time laps studies had to be evaluated, being able to trace the nanobody through the whole delivery process and the cell cycle.

1.6.2 MOF nanoparticles as a defined carrier system for His-tagged functional units

MOFs are a class of materials synthesized of inorganic building units, metal ions or metal clusters that are coordinatively connected by organic linkers to create porous three-dimensional frame works. Their crystallinity, chemically functionalizable pores and potential systematic structural variation are factors that allow to precisely design these materials for particular purposes. In the thesis, a new functionalization concept

had to be evaluated using the interaction between Lewis bases, such as the imidazole function of histidine and coordinatively unsaturated metal sites present on the external surface of MOF NPs to self-assemble different functional units onto MOF NPs. The versatility of the general assembly concept had already been shown in pilot studies by Dr. Ulrich Lächelt (Pharmaceutical Biotechnology, LMU München). The aim within the current thesis was to evaluate its potential to be used as a carrier for the intracellular delivery of various His-tagged compounds.

The first specific aim was to evaluate the toxicity of the three selected MOF NPs, MIL-88A, HKUST-1 and Zr-*fum* on cells to proof their general feasibility to be used as intracellular carriers.

The second aim was to further investigate the functionalized MOF NPs in terms of size, their behavior under biological conditions as well as the characteristics of the interaction of the His-tagged compounds with the MOF NPs.

The third aim was the actual application of the different MOF NPs to carry proteins as well as small molecules into the cells, including the investigation of various His-tagged units to enhance cellular uptake as well as endosomal escape. For this purpose different endosomolytic peptides, and two lipids DOPC and DOPE had to be evaluated.

The fourth aim was to investigate the applicability of this system to deliver biological active proteins or peptides into cells. Therefore the delivery of H_6-luciferase in order to serve as a reporter system and the ability to deliver three apoptotic membrane impermeable bioactive pro-apoptotic peptides, Bad, Bak and KLK as well as mitochondrial cytochromeC were to be evaluated.

2 Material and Methods

2.1 Chemicals and solvents

Table 1: Chemicals and solvents

Chemical or Solvent (Abbreviation)	Manufacturer
2-Chlorotrityl chloride resin	Iris Biotech (Marktredwitz, Germany)
Atto-647N (NHS ester)	Atto-Tec GmbH (Siegen, Germany)
(Benzotriazol-1-yloxy)-tripyrrolidinophospho-nium hexafluorophosphate (Pybop)	Multisyntech GmbH (Witten, Germany)
Protein Standard, Broad Range	NEB (Frankfurt am Main).
Collagen A	Merck KGaA (Grafing Germany)
Copper(II) nitrate hemipentahydrate	Riedel-de Haën (Seelze, Germany)
DBCO-PEG4-NHS ester	Jena Biosciences (Jena, Germany)
Dimethylsulfoxide (DMSO)	Bernd Kraft GmbH (Duisburg, Germany)
Ethanol (99.9 %)	VWR (Darmstadt, Germany
Fmoc or Boc protected α-amino acids	Iris Biotech (Marktredwitz, Germany)
Fmoc-N-amido-dPEG$_{12}$-acid	Quanta Biodesign (Powell, USA)
Fmoc-N-amido-dPEG$_{36}$-acid	Quanta Biodesign (Powell, USA)
Fmoc-NH-(PEG)$_{27}$-COOH (PEG$_{28}$	Polypure (Oslo, Norway)
Fumaric acid (≥ 99.5 %)	Fluka (Buchs, Switzerland)
HPLC grade acetonitrile	VWR (Darmstadt, Germany)
Iron(III) chloride hexahydrate (99 %)	Grüssing GmbH (Filsum, Germany)
N,N,N′,N′-Tetramethyl-O-(1H-benzotriazol-1-yl)uronium hexafluorophosphate (HBTU)	Multisyntech GmbH (Witten, Germany)
N,N-Diisopropylethylamine (DIPEA),	Iris Biotech (Marktredwitz, Germany
Peptide grade dimethylformamide (DMF)	Iris Biotech (Marktredwitz, Germany)
Piperidine, and trifluoroacetic acid (TFA)	Iris Biotech (Marktredwitz, Germany)
TentaGel S RAM resin	Rapp Polymere GmbH (Tübingen, Germany)

All chemicals which are not listed in Table 1 have been purchased from Sigma-Aldrich (Germany).

2.2 Proteins

CytochromeC (equine heart) and transferrin (from human plasma) were bought from Sigma-Aldrich (Germany).

Transferrin was modified with a H_6-tag and labeled with Atto647N (NHS-ester) by Dr. Ulrich Lächelt (Pharmaceutical Biotechnology, LMU München). It is called H_6-Tf* in the following work.

H_6-GFP and H_6-luciferase have been expressed and purified as described in (2.11.1, 2.11.2). GFP binding nanobody (GBP, α-GFP-Nb), and lamin binding nanobody (α-lamin-Nb) have been expressed and purified as is described in (2.11.3).

2.3 Buffers

Table 2: Buffers used for experimental procedures

Buffer	Description
2-(4-(2-hydroxyethyl)-1-piperazinyl)-ethansulfonic acid (HEPES)	Biomol (Hamburg, Germany)
Phosphate buffered saline	If another pH value is stated it was adjusted with aqueous 1 M HCl or NaOH solution
Lysis buffer	20 mM Tris, 20% Succrose (w/v), 0.2 M NaCl, 10 mM $MgCl_2$, pH 7.5
LAR buffer	20 mM Glycylglycine, 1mM $MgCl_2$, 0.1 mM EDTA, 0.051 % (w/v) DTT, 0.0278 % (w/v) ATP, 0.5 % (v/v) Coenzyme A Stock solution, pH 8-8.5
Ellman's buffer	0.2 M Na_2HPO_4, 1 mM EDTA, pH 8.0

2.4 Solutions

DOPC solution: DOPC 3.6 mM in 60/40 H_2O/EtOH

DOPE solution: DOPE 3.6 mM in 54/46 H_2O/EtOH

2.5 Bacterial strains

E. coli strain DH5α was bought from Invitrogen (Karlsruhe, Germany) and was used for plasmid amplification.

For expression of H_6-GFP, *E.coli* protein expression strain BL21(DE3)plysS was purchased from Novagen (Merck4biosciences, Darmstadt , Germany).

For expression of H_6-luciferase RosettaBL21(DE3)pLysS from Merck Millipore, Germany were used.

Chemical competent bacteria strains were prepared in house.

2.6 Cell culture

Antibiotics, fetal bovine serum (FBS) and cell culture medium were bought from Life Technologies (Carlsbad, USA).

All cell lines were grown in medium supplemented with 10% FBS, 100 U ml^{-1} penicillin, 100 µg ml^{-1} streptomycin and 4 mM stable glutamine. All cells were cultured at 37 °C and 5% CO_2 in a humified incubator.

Table 3: Cell lines, description and media

Cell line	Description	Media
HeLa_*wt*	ATCC CCL-2; Subline of human epithelial cervical adenocarcinoma cell	DMEM
HeLa_Actin-GFP	Recombinant HeLa_*wt* cell line expressing Actin-GFP	RPMI-1640, folate-free
HeLa_PCNA-GFP	Recombinant HeLa_*wt* cell line expressing PCNA-GFP	RPMI-1640, folate-free
HeLa_Tubulin-GFP	Recombinant HeLa_*wt* cell line expressing Tubulin-GFP	RPMI-1640, folate-free
HUH7_*wt*	Human hepatocellular carcinoma cells	DMEM/Ham's F12 1:1
KB_*wt*	ATCC CCL-17; Subline of human epithelial cervical adenocarcinoma cell line HeLa_*wt*	RPMI-1640, folate-free

HeLa_Actin-GFP and HeLa_Tubulin-GFP cells were generated by Dr. K. von Gersdorff according to the procedure of the generation of HUH7_Actin-GFP and HUH7_Tubulin-GFP cell lines, which has been described elsewhere (PhD thesis LMU, 2006).

HeLa_PCNA-GFP [138] cells were kindly provided by Prof. Dr. Heinrich Leonhardt (Department of Biology II, LMU München).

2.7 Metal-organic frameworks (MOFs)

All metal-organic frameworks (MOFs) have been synthesized and analyzed by Patrick Hirschle (Department of Chemistry, LMU München).

Table 4: Metal-organic frameworks (MOF) used for the experiments

Name	Organic linker	Metal	Ref
MIL-88A	Fumaric acid	$FeCl_3$ x 6 H_2O	[139]
HKUST-1	Trimesic acid	$Cu(NO_3)_2$ x 2.5 H_2O	[140]
Zr-*fum*	Fumaric acid	$ZrCl_4$	[129]

2.8 Oligomer and peptide synthesis

Sequence-defined oligomers were synthesized by Dr. Dongsheng He, Dr. Edith Salcher, Dr. Claudia Scholz and Philipp Klein as has been described in [50, 51, 53, 141-143]. The oligomers including their exact sequence are listed in Table 5.

A_6/H_6-Acr (Acridine-PEG_{28}-A_6/H_6-NH_2), H_6-CF, H_6-A647N, H_6-Tf and 6-azido-hexanoic acid were synthesized by Dr. Ulrich Lächelt (Pharmaceutical Biotechnology, LMU München), $H_{0/3/6}$-Acr (Acridine-STOTDA-$H_{0/3/6/}$) were synthesized by Benjamin Steinborn (Pharmaceutical Biotechnology, LMU München).

H_6-Bad, H_6-KLK, H_6-Bak were synthesized on TentaGel S RAM (C-terminal amide) using an automated Syro Wave or semi-automated Initiator+ SP Wave Peptide Synthesizer (Biotage, Uppsala, Sweden). Syringe microreactors were obtained from Multisyntech GmbH (Witten, Germany).The peptides were sequentially assembled from C- to N-terminus under standard Fmoc solid phase peptide synthesis conditions. Automated synthesis using the Syro Wave was carried out with HBTU as activating reagent and double-coupling steps. Semi-automated synthesis with the Initiator+ SP Wave and manual coupling steps were carried out with Pybop as activating reagent. Coupling steps were carried out using 4 eq Fmoc L-amino acid (relative to free resin-bound amines), 4 eq HOBt, 4 eq activating reagent and 8 eq DIPEA in NMP – DMF 6 : 4 (7 mL per g resin) and 10 min incubation at room temperature. Fmoc deprotection was accomplished by 4 x 10 min incubation with 20 % piperidine in DMF (10 mL per g resin) at room temperature. After each coupling and deprotection step a washing procedure comprising 5 x 1 min DMF incubation (10 mL per g resin) was carried out. Finally, all peptides were cleaved off the resin by incubation with TFA–TIS–H_2O

95 : 2.5 : 2.5 (10 mL per g resin) for 90 min at room temperature. In case of intense yellow color of collected cleavage solution, TIS was added in small portions until decolorization occurred.

The cleavage solution was concentrated by evaporation under nitrogen stream and peptides were precipitated in 50 mL pre-cooled MTBE (2-methoxy-2-methylpropane) – n-hexane 1 : 1. All peptides were purified by size exclusion chromatography (SEC) using an Äkta purifier system (GE Healthcare Bio-Sciences AB, Sweden) based on a P-900 solvent pump module, a UV-900 spectrophotometrical detector, a pH/C-900 conductivity module, a Frac-950 automated fractionator, a Sephadex G-10 column and 10 mM hydrochloric acid solution – acetonitrile 7 : 3 as solvent. All peptides were lyophilized after SEC resulting in hydrochloride salts of the peptides. The compounds were analyzed by matrix-assisted laser desorption/ionization mass spectrometry (MALDI-MS, 2.10.2). The peptides were used without further purification.

2.9 Synthesis of AzMMMan linker

The AzMMMan linker was synthesized as has previously been described by Beckert *et al.* [107].

2.9.1 Synthesis of 3-(bromomethyl)-4-methyl-2,5-furandione (BrMMan)

Dimethylmaleic anhydride (DMMan) (5.04 g, 39.97 mmol), N-bromosuccinimide (4.56 g, 25.62 mmol), and benzoyl peroxide (64 mg, 0.36 mmol) were dissolved in 250 mL carbon tetrachloride (dried over molecular sieve UOP Type 3A). This mixture was gently refluxed under nitrogen for 5 h in a 500 mL round-bottom flask at 110-120 °C. Afterwards the reaction mixture was allowed to cool to room temperature and an additional amount of benzoyl peroxide (64 mg, 0.36 mmol) was added. The refluxing was continued for 5 h. After cooling to room temperature the residue was filtered and washed two times with 25 mL carbontetrachloride (dried over molecular sieve UOP Type 3A). Subsequently, the organic phase was washed two times with water (100 mL) and one time with brine (100 mL). The organic layer was dried over Na_2SO_4 and concentrated in vacuo to result in a yellow oil (DiBrMMan : BrMMan : DMMan; 1 : 10 : 4).

To remove the benzoyl peroxide, this oil was first purified by chromatography on a silica gel column (0.035-0.07 mm, 60A) and eluted with a mixture of petroleum ether/ethyl acetate (8:2) (DiBrMMan : BrMMan : DMMan; 0.3 : 10 : 4) .
Finally the residue was distilled with the help of a kugelrohr apparatus under vacuum. First DMMan was removed at 110-120 °C, 7 mbar. DMMan might be recovered and reused. The second fraction destilling at a temperature of 140 °C, 7 mbar contained BrMMan (1.8 g, yield 22%). Di-(bromomethyl)-1,5-furandione (DiBrMMan) was left in the still pot.
BrMMan: ^{1}H NMR (400 MHz, $CDCl_3$) 4.17 (s 2H), 2.17 (s 3H).
DiBrMMan: ^{1}H NMR (400 MHz, $CDCl_3$) 4.27 (s 4H)
DMMan: ^{1}H NMR (400 MHz, $CDCl_3$) 2.07 (s 6H)

2.9.2 Synthesis of 3-(azidomethyl)-4-methyl-2,5-furandione (AzMMMan)

3-(bromomethyl)-4-methyl-2,5-furandione (310.5 mg, 1.5 mmol) was dissolved in 10mL acetone (dried over molecular sieve UOP Type 3A). Sodium azide (97.5 mg, 1.5 mmol) was added in one portion. The suspension was stirred for 24 h at 37 °C. After filtering the solvent was evaporated. The remaining oil was dissolved in ethyl acetate (20 mL) and washed two times with water (20 mL). Afterwards the organic layer was washed with 20 mL brine and dried over Na_2SO_4. The liquid was concentrated in vacuo to result in a brown oil. (222 mg, yield 88 %).
^{1}H NMR (400 MHz ,$CDCl_3$) 4.29 (s, 2H), 2.22 (s, 3H).
IR vmax 2101, 1759, 1679 cm^{-1}.

2.10 Analytics

2.10.1 ^{1}H-NMR

^{1}H-NMR spectra were recorded at room temperature using a Jeol JNMR-GX 400 (400 MHz) or JNMR-GX 500 (500 MHz). Chloroform-d ($CDCl_3$) was used as solvent. 5 mg sample were used per measurement. Chemical shifts were calibrated to the residual proton signals of the solvent and are reported in ppm. Data is indicated with s = singlet. Spectra were analyzed using MestReNova (Mestrelab Research).

2.10.2 Mass spectroscopy

The compounds were analyzed by matrix-assisted laser desorption/ionization mass spectrometry (MALDI-MS) using 2,5-dihydroxybenzoic acid matrix and an Autoflex II mass spectrometer (Bruker Daltonics, Bremen, Germany).

2.11 Heterologous protein expression and purification

2.11.1 Cloning of H_6-luciferase expression plasmid

The plasmid containing the firefly luciferase gene (pEGFPLuc) was obtained from Clontech (USA). After transformation of the plasmid into DH-5α, amplification and re-purification, the coding region of the plasmid was amplified using the following primers, carrying a HindIII and EcoRI restriction side and a standard PCR Protocol (denaturation: 4 min 95 °C, 30 cycles: 95 °C, 30 sec; 56 °C 30 sec; 68 °C 2 min; final extension: 68 °C 4 min; hold: 4 °C)

eGFP1: 5'-CCGGAATTCATGGTGAGCAAGGGCGAGG-3'
Luc2: 5'-CCCAAGCTTTTACACGGCGATCTTTCCGC-3'

Using HindIII and EcoRI, this gene was cloned into a pET-28a vector (Novagen, Merck Millipore, Germany), following the pET System Manual 11th Edition. The resulting protein should carry a His-tag at the N- and C-terminus.
The resulting plasmid was verified by restriction digest using EcoRI and Hind III.

2.11.2 Green fluorescent protein (GFP) and luciferase

Recombinant green fluorescent protein containing a His-tag (H_6-GFP) was expressed and purified as has been described previously [54].
The H_6-luciferase expression plasmid was transformed into RosettaBL21(DE3)pLysS (MerckMillipore, Germany), following the standard transformation protocol (Novagen®, User Protocol TB009 Rev. H 0211JN).
BL21(DE3)plysS (H_6-GFP) or RosettaBL21(DE3)plysS (H_6-luciferase) were grown in LB Medium at 37 °C with shaking (H_6-luciferase: 15 µg/mL kanamycin, 34 µg/mL chloramphenicol; H_6-GFP: 100 µg/mL ampicillin, 50 µg/mL chloramphenicol) until an

optical density of 0.4-0.6 (600 nm). Afterwards the bacteria were cooled to room temperature (RT), protein expression was induced by adding 0.5 mM IPTG and they were incubated at 25 °C with shaking over night. Bacteria were harvested by centrifugation (30 min, 4000 x g, 4 °C). The supernatant was discarded and the pellet was resuspended in Lysis buffer (Table 2). RNase at a final concentration of 10 µg/mL, DNase at a final concentration of 30 µg/mL, lysozyme at a final concentration of 1 mg/mL and 1 mM PMSF were added. The solutions were frozen and thawed and sonicated (3 x 20 sec on ice, full power). The bacterial lysate was ultracentrifuged (1 h, 20000 rpm, 4 °C) and filtered using a 0.45 µm syringe filter.
The proteins were purified by nickel chromatography using a gradient from binding buffer (PBS pH 7.4, 20 mM imidazole) to elution buffer (PBS pH 7.4, 500 mM imidazole). Afterwards, the proteins were subjected to size exclusion chromatography (Sephadex G25 super fine size exclusion column) using PBS pH 7.4 as mobile phase for buffer exchange to remove the extend of salt. Finally the proteins were concentrated with Amicon Ultra centrifugal filter units (MWCO=10 kDa (H_6-GFP); MWCO=30 kDa (H_6-luciferase), Millipore, USA) and stored at -20 °C. The amount of purified protein was quantified using a Nanodrop (Thermo Scientific, Massachusetts, USA) and an ε(H_6-GFP)= 21890 $M^{-1}cm^{-1}$; 26.9 kDa or an ε(H_6-luciferase)= 37200 $M^{-1}cm^{-1}$; 63 kDa.

2.11.3 GFP- and lamin nanobody

GFP- or lamin nanobody (α-GFP-Nb or α-lamin-Nb) have been expressed and purified, similar to the purification of H_6-GFP and H_6-luciferase (2.11.2), as has been described elsewhere [63, 64]. Instead of lysis buffer, PBS pH 7.4 (500 mM NaCl, 20 mM imidazole, 2 mM PMSF) was used. After freezing, lysozyme at a final concentration of 100 µg/ mL and DNase I at a final concentration of 25 µg/mL were added. The bacteria lysate was incubated for 1 h at 4 °C under agitation, followed by sonication, ultracentrifugation and purification as has been described above. The amount of purified nanobody was quantified using a Nanodrop (Thermo Scientific, Massachusetts, USA) and ε= 27.000 $M^{-1}cm^{-1}$.

2.12 Modification of proteins with dyes, linkers or functional units

2.12.1 Modification of nanobodies with Atto647N

α-GFP-Nbs or α-lamin-Nbs were diluted in PBS (pH 8.0) to a concentration of 1 mg/ml (0.08 µmol/mL). Atto647N was solubilized in DMSO (10 mM) and 0.2 molar equivalents were added to the protein solution. The mixture was incubated under constant stirring for 3 h at 37 °C. Uncoupled dye was removed by size exclusion chromatography (Äkta purifier system GE Healthcare Bio-Sciences AB, Uppsala, Sweden) via a Sephadex G25 column using PBS (pH 8.0) as a mobile phase. The purified protein-dye conjugate was concentrated using Amicon Ultra centrifugal filter units (MWCO=10 kDa, Millipore, USA). Protein concentration was determined spectrophotometrically (NanoDrop 2000 Spectrophotometer, Thermo Scientific) using an extinction coefficient of 27.000 $M^{-1}cm^{-1}$. The purity of the protein- dye conjugate was confirmed on SDS-PAGE.

2.12.2 Modification of nanobodies with fluorescein isothiocyanate

α-GFP-Nbs or α-lamin-Nbs were diluted in PBS to a concentration of 2 mg/mL (0.16 µmol/mL). Fluorescein isothiocyanate (FITC) was solubilized in DMSO (13 mM) and 0.2 molar equivalents were added to the protein solution. The mixture was incubated under constant stirring for 4 h at 37 °C. Uncoupled dye was removed by size exclusion chromatography (Äkta purifier system GE Healthcare Bio-Sciences AB, Uppsala, Sweden) via a Sephadex G25 column using PBS (pH 7.4) as a mobile phase. The purified protein-dye conjugate was concentrated using Amicon Ultra centrifugal filter units (MWCO=10 kDa, Millipore, USA). Protein concentration was determined spectrophotometrically (NanoDrop 2000 Spectrophotometer, Thermo Scientific) using an extinction coefficient of 27.000 M^{-1} cm^{-1}.

2.12.3 Modification of cytochromeC with His-tag

CytochromeC (CytC) from equine heart was solubilized in PBS (20 mg/mL) and a DBCO-PEG4-NHS ester was solubilized in DMSO (50 mg/mL). One molar equivalent of linker was added to the protein solution and incubated for 3 h at 37 °C with

shaking. Non coupled linker was removed by size exclusion chromatography using an Äkta purifier system (GE Healthcare Bio-Sciences AB, Uppsala, Sweden), a Sephadex G25 super fine size exclusion column and PBS pH 7.4 as mobile phase. Afterwards four molar equivalents of H_6-azide were added to the DBCO modified CytC (3.56 mg/mL) and the mixture was incubated for 3 h at 37 °C. Non modified CytC was removed by nickel chromatography using an Äkta purifier system (GE Healthcare Bio-Sciences AB, Uppsala, Sweden), PBS (pH 7.4, 500 mM NaCl, 20 mM Imidazole) as binding buffer and PBS (pH 7.4, 500 mM NaCl, 500 mM imidazole) as elution buffer, followed by size exclusion chromatography (Sephadex G25 super fine size exclusion column) using PBS (pH7.4) as mobile phase to remove non coupled H_6-azide and for buffer exchange. The purified protein was concentrated using Amicon Ultra centrifugal filter units (MWCO=10kDa; Millipore, USA). The modified CytC is called H_6-CytC in the thesis.

2.12.4 Modification of H_6-GFP with AzMMMan

AzMMMan was dissolved in ACN (0.1 mg/mL). H_6-GFP was diluted in Hepps pH 8.0 at a final concentration of 10 mg/mL. The two solutions were mixed at a molar ratio of GFP to AzMMMan 1:200; 1:8 if calculated on the free terminal amino groups, as GFP has 25 lysines. The mixture was incubated for 2 h at 25 °C with shaking. To remove non-bound AzMMMan the protein solution was subjected to size exclusion chromatography (Sephadex G25 super fine size exclusion column) usingPBS (pH 8.0) as mobile phase. Afterwards, the purified H_6-GFP-AzMMMan was concentrated with Amicon Ultra centrifugal filter units (MWCO = 10 kDa, Millipore, USA) and stored at -20 °C.

2.12.5 Modification of H_6-GFP-AzMMMan with DBCO-K-H_6-K(H_6-DBCO)$_2$ (*1070*)

H_6-GFP-AzMMMan was diluted in PBS pH 8.0 (0.33 mg/mL). After dilution of DBCO-K-H_6-K(H_6-DBCO)$_2$ (***1070***) in ACN at final concentration of 2.5 mg/mL it was added to the H_6-GFP-AzMMMan solution and incubated for 3 h at 37 °C (molar ratio of H_6-GFP-AzMMMan : ***1070*** of 1:1. The H_6-GFP-AzMMMan-***1070*** conjugate was stored at -20 °C and used without any further purification.

2.12.6 Preparation of nanobody/oligomer formulations

Nanobodies were formulated with oligomers (Table 5) at a molar ratio of 1:5. Different oligomer amounts were diluted in HEPES buffer (pH 8.0) and the pH was adjusted with NaOH (1 M) to pH 8.0. Afterwards the dye modified nanobody was added to a final concentration of 0.5 mg/mL (0.04 µmol/mL). The mixture was incubated for 4 h with shaking at 37 °C and used for further experiments.

2.13 Preparation of MOF suspensions in HBG

MOF suspensions in HBG were always freshly prepared prior to performing the experiment. The necessary amount of MOF material in ethanol was centrifuged (10 min, 10.000 rpm), followed by carefully inverting the tubes and gently tapping them on a paper towel in order to get rid of the ethanol supernatant without damaging the MOF-pellet. The MOF pellet was then resuspended in HBG at a final concentration of 5 or 10 mg/mL by continuous pipetting, followed by 10 min sonication.

2.14 Modification of functionalized MOFs with different lipids

2.14.1 Micelle formation

100 µg MOFs were incubated with 2.5 nmol His-tag in a final volume of 1 mL HBG buffer for 15 min at room temperature, followed by centrifugation for 5 min at 13.000 rpm. Afterwards, micelle encapsulation was carried out as has been described in [86]. The supernatant was removed, and the functionalized MOFs were

resuspended in 10 µL DOPC solution (2.4), which was sonicated for 5 sec before usage. The MOF/DOPC mixture was sonicated for further 3-5 min until obtaining a homogenous solution. Afterwards 100 µL H_2O were added really fast, the solution was mixed thoroughly and used for further experiments.

2.14.2 Addition of lipids

MOFs were functionalized with His-tags at a final concentration of 7.3 mol His-tag/mg MOF per 333 µL HBG buffer for 15 min at room temperature. Afterwards definite amounts of a DOPC or DOPE solution were added. If a mixture of both solutions was added, the two solutions were mixed prior to usage. Afterwards the mixture was filled up to a final MOF concentration of 1 mg MOF/3333 µL HBG buffer and used for further experiments.

2.15 Ellman's assay

The oligomers to be measured were diluted in 30 µL HBG and 170 µL working solution (2.44 mL Ellman's buffer (Table 2) and 60 µL DTNB solution (c= 4 mg/mL in Ellman's buffer) were added. The mixture was incubated for 15 min at 37 °C with shaking and absorption (412 nm) was measured using a GENESYS UV-VIS spectrophotometer (Thermo Scientific, Massachusetts, USA). The concentration of free cysteines was calculated using a calibration curve, based on free cysteine. The percentage of free mercapto groups was calculated on the theoretical amount (100 %) of cysteines being present in the oligomer solution.

2.16 Inhibition of disulfide formation via NEM blocking

The oligomer solution was diluted in HEPES to a final concentration of 2 mg/mL, adjusted to a pH of 7.0 with NaOH (1 M) and reacted with a tenfold molar excess of N-ethylmaleimid (NEM), calculated on the amount of cysteines, for 2 h. Subsequently free NEM was reacted with a 20-fold molar excess of N-acetylcysteine for 2 h. The oligomer solutions were purified by size exclusion chromatography (Äkta purifier

system GE Healthcare Bio-Sciences AB, Uppsala, Sweden) via a Sephadex G10 column using acetonitrile/H_2O (7/3) (10 mM HCl) as a mobile phase.

2.17 Investigation of pH dependent binding of H_6-tags to Zr-*fum* over a longer period

This experiment has been carried out by Benjamin Steinborn (Pharmaceutical Biotechnology, LMU München). A 10 mg/mL Zr-*fum* stock solution in HBG (pH 7.4) was prepared as described above (2.13). In order to evaluate the stable binding and extent of acidic release of His-tags and Zr-*fum* MOF NPs over a longer period, Zr-*fum* NPs in HBG were loaded with H_6-A647N. 50 µL of the freshly prepared Zr-*fum* NPs were diluted in ~500 µL HBG pH 7.4 (depending on the amount of HCl added to the sample in the next step), followed by addition of 4 µL 1 mM H_6-A647N. The HBG volume therefore slightly varied in order to always allow for equal final sample volumes of 500 µL. Samples were briefly vortexed and incubated under agitation for 15 min (25 °C, 600 rpm, light protection).
Afterwards, samples were acidified to pH 3, pH 5 and pH 7.4 by addition of 9.2 µL, 4.5 µL or 0 µL 1 M HCl respectively. After 0.5 h, 3 h and 24 h, the respective samples were centrifuged (5 min, 14.000 rpm). The presence of free dye in the supernatant was determined photometrically at 646 nm (n=3). Independent samples were used for each time point.

2.18 Zeta potential measurements of MOF nanoparticle functionalization

3 nmol H_6-Acr or A_6-Acr were diluted in HBG buffer. In case of pro-apoptotic peptides and CytC 5 nmol were used. 100 µg MOF NPs were added (final volume 30 µL) and samples were incubated at room temperature for 15 min with shaking. Shortly before the measurement in a folded capillary cell (DTS1070), samples were diluted to a final MOF concentration of 0.1 mg/mL. Zeta potential was measured by electrophoretic laser-light scattering using a Zetasizer Nano ZS (Malvern Instruments, Worcestershire, U.K.). Zeta potentials were calculated by the Smoluchowski equation, each sample was measured 3 times with 10 to 30 subruns at 25 °C.

2.19 Fluorescence correlation spectroscopy (FCS) and fluorescence cross-correlation spectroscopy (FCCS)

2.19.1 Measurements of nanobody/oligomer mixtures

FCS measurements were carried out together with Dr. Tobias Preiß (Faculty of Physics, LMU München). To permit measurements at the same nanobody/oligomer concentrations which were used for cell experiments, non-modified nanobody was spiked with 1 % A647N-labeled nanobody. Afterwards nanobody/oligomer formulations were prepared as described above and diluted 1 : 1 to the same concentration as subsequently was put on cultured cells. Nanobody or nanobody/oligomer formulations (at a molar ratio of 1 : 5) were measured at a final nanobody concentration of 0.25 mg mL^{-1} (0.02 µmol mL^{-1}) in HEPES buffer (pH 7.4). The measurements were conducted on a ConfoCor2 setup (Zeiss Germany) using a 40× NA1.2 water immersion objective (Zeiss Germany) that focuses the exciting laser light (633 nm) into the sample. Fluorescence fluctuations of labeled molecules diffusing through the focal spot were recorded by an avalanche photodiode and correlated with the correlation function $G(\tau) = (\langle F(t)F(t + \tau)\rangle)/\langle F\rangle^2 - 1$. To derive the hydrodynamic radius of nanobody/oligomer formulations, correlation curves were fitted using two component fit were the first component was fixed to the diffusion time of freely diffusing nanobodies.

2.19.2 Measurements of functionalized MOFs

FCS and FCCS measurements were carried out by Dr. Tobias Preiß (Faculty of Physics, LMU München). The non-fluorescent MOF nanoparticles are not detectable by the FCS unless fluorescently labeled His-tags are attached to the nanoparticles. Thus a shift to higher diffusion times of correlation curve after addition of NPs to fluorescently labeled His-tags certifies the binding of His-tags to NPs surface. Normalization of autocorrelation curves helps to clearly visualize that the autocorrelation function of the MOF/His-tag is shifted towards higher correlation times with respect to the free His-tag molecules. Dual-color fluorescence cross-correlation spectroscopy (FCCS) allows for a comparison between spectrally separated channels to extract codiffusion events that reflect interactions between differently labeled molecules [144, 145].

For FCS and FCCS measurements, an Axiovert 200 microscope with a ConfoCor 2unit (Carl Zeiss, Jena, Germany) equipped with a 40x (NA 1.2) water immersion apochromat objective (Carl Zeiss) was used. A helium neon laser (633 nm) and for FCCS additionally an argon laser (488 nm) was used for illumination. Samples were measured in eight-well LabTekchamber slides (Nunc, Rochester, NY). If nothing else mentioned, measurements were performed in HBG (pH 7.4) at a temperature of 22.5 °C. Correlation was performed using ConfoCor 2 software.

2.19.2.1 Investigation of functionalization of MOFs with H_6-A647N by FCS

200 µL of H_6-A647N in HBG (pH 7.4) were measured in a 8-well chamber slide (Nunc™ Lab-Tek™ II) prior to and after addition of 2 µL of MOF stock solution.
The hydrodynamic radius of H_6-A647N was found to be $R_H^{H6A647N}$ = 2 nm ($D_{H6A647N}$ = 120 µm²/s). A two-component analysis (taking into account that part of His-tag molecules are not bound) resulted in an apparent diffusion time of 3.5 ms which corresponds to a hydrodynamic radius of Zr-*fum*/H_6-A647N of $R_H^{Zr\text{-}fum/H6A647N}$ = 56 nm and a diffusion constant $D_{Zr\text{-}fum/H6A647N}$ = 4.1 µm²/s (using finite size correction according to Wu *et al.* [146]).

2.19.2.2 Investigation of acidic release of H_6-A647N from Zr-*fum* by FCS

Investigation of the acidic release of H_6-A647N from Zr-*fum* nanoparticles by FCS
The Zr-*fum*/H_6-A647N solution was prepared as described above and acidified by the addition of 3 µL of HCl (1 M) / 200 µL sample. The two-component analysis provides a fraction of the fast diffusing species (His-tag molecules) of 50 %. As the curve is biased by agglomerates this value is just a rough estimation. But by comparison with the autocorrelation function in neutral environment the separation of His-tag in acidic environment is evident, providing an indication of pH-dependent detachment of His-tags from MOF nanoparticles.

2.19.2.3 Investigation of the influence of serum on Zr-*fum*/H_6-A647N stability by FCS

As described above, Zr-*fum* nanoparticles were functionalized with H_6-A647N in HBG at pH 7.4. Subsequently the coated NPs were diluted in Dulbecco's Modified Eagle's Medium (DMEM) containing 10 % FBS. To confirm the results, the same experiment was repeated but replacing the NP suspension by pure HBG as a control. H_6-A647N in HBG at pH 7.4 was diluted with DMEM (10 % FBS). The ensuing FCS measurements showed the same fast decay as before for H_6-A647N in HBG at pH 7.4, proving that H_6-A647N is not clustering/agglomerating in DMEM (10 % FBS).

2.19.2.4 Fluorescence cross-correlation spectroscopy

FCCS analysis was performed in order to confirm the co-localization of two proteins (H_6-GFP and H_6-Tf*) at the nanoparticles surface. 100 µL of a 60 nM H_6-GFP solution in HBG (pH 7.4) and 100 µL of a 50 nM H_6-Tf* solution in HBG (pH 7.4) were mixed in a 8-well chamber slide and measured prior to and after addition of 2 µL of MOF stock solution.

2.20 Cell experiments

2.20.1 Cell fixation and staining

Cells were seeded in 8-well Nunc chamber slights (Thermo Scientific, Germany) at a density of 12.000 cells/well. In case of KB_*wt* cells, wells were coated with collagen A prior to seeding. After 24 h incubation at 37 °C and 5 % CO_2 in a humified incubator, medium was removed and cells were washed with PBS (pH 7.4). 4 % (w/v) cold paraformaldehyde solution was added and cells were incubated for 10 min at room temperature with shaking. Cells were washed three times with PBS (pH 7.4) containing 0.1 % Tween 20 (PBST). Afterwards cells were permeabilized for 5 min by adding PBS (pH 7.4) containing 0.5 % Triton X-100. Cells were washed twice with PBST and incubated for 10 min in blocking solution (PBST containing 4% (w/v) bovine serum albumin). Atto647N labeled α-GFP-Nb or α-lamin-Nb were diluted in blocking solution (7 µg/mL) and incubated on the cells for 45 min at room

temperature. Cells were washed three times for five minutes with PBST and stored at 4 °C.

2.20.2 Screening of different oligomers for nanobody delivery

Nanobody was always formulated with oligomer at a molar ratio of 1:5. Different oligomer amounts were diluted in HEPES buffer (pH 8.0) and the pH was adjusted with NaOH (1 M) to pH 8.2. Afterwards the dye modified nanobody was added to a final concentration of 0.5 mg/mL (0.04 µmol/mL). The mixture was incubated for 4 h with shaking at 37 °C. For the screening experiment, cells were seeded in 96-well plates (Greiner bio-one) at a density of 4.000 cells/well. In case of KB_*wt* cells, wells were coated with collagen A prior to seeding. After 24 h medium was replaced with 80 µL fresh, serum-containing folate free RPMI medium. The various samples were added into each well at a final concentration of nanobody of 1.5 µM or 3.6 µM and incubated in case of targeted oligomers for 1 h at 37°C. Medium was removed and cells were incubated for 18 h in fresh serum containing folate free RPMI medium. Mixtures containing non-targeted oligomers were incubated for 15 h on the cells followed by 4 h incubation in fresh medium. Medium was replaced with PBS (pH 7.4) and cells were imaged using PerkinElmer Operetta® High Content Imaging System (Germany).

2.20.3 Luciferase assay

10.000 KB_*wt* cells/well were seeded in collagen A coated 96 well plate (PS Microplatte 96 well F Boden µClear TC weiß, Greiner, Frickenhausen, Germany) and grown in medium containing 10 % FBS for 24 h at 37 °C, 5 % CO_2 in a humified incubator. After 24 h the cell culture medium was replaced with 80 µL fresh medium and different samples were added. Cells were incubated for further 24 h at 37 °C, 5 % CO_2 in a humified incubator.

To measure intracellular delivered H_6- luciferase, cells were washed with PBS (pH 7.4) and PBS (pH 7.4) containing 0.5 mM D-luciferin was added.

To measure the extracellular luciferase signal, cells were washed with PBS (pH 7.4) and 100 µL LAR buffer (Table 2) were added to the cells.

To measure luciferase signal of intra- and extracellular H_6-luciferase, cells were treated with 100 µL cell culture lysis reagent (Promega, Mannheim, Germany) and incubated for 30 min at RT. The luciferase activity in the cell lysate was measured using the luciferase assay kit (Promega, Mannheim, Germany).
For all three different cases, the luciferase signal was always determined using a Centro LB 960 plate reader luminometer (Berthold Technologies, Bad Wildbad, Germany).

2.20.4 Cell viability assay (MTT assay)

Setup A) Nanobody experiments. Cells were seeded in 96-well plates at a density of 6.000 cells/well. In case of KB_*wt* cells, wells were coated with collagen A prior to seeding. Samples were prepared as described above. After 24 h medium was replaced with 80 µL of fresh medium containing 10 % FBS. Samples were diluted 1:1 with HEPES buffer (pH 8.0) (0.02 µmol/mL), 20µL of each sample were added to each well (final protein concentration 3.6 µM) and incubated on cells for 1 h at 37 °C and 5 % CO_2. Afterwards medium was replaced with fresh serum containing folate free RPMI medium and cells were incubated for 18 h.
Setup B) MOF experiments. Cells were seeded in 96-well plates at a density of 4.000 cells/well. After 24 h medium was replaced with 80 µL of fresh medium. The appropriate amount of compound to be tested was diluted in HBG (pH 7.4) and 20 µL of each sample/well were added. Cells were incubated for 48 h at 37 °C and 5 % CO_2 in a humified incubator.
A) and B) Afterwards the MTT assay was performed for both experimental setups in the same way. 10 µL of MTT (3-(4,5-dimethylthiazol-2-yl)-2,5-diphenyltetrazolium bromide) (5 mg/mL) were added to each well reaching a final concentration of 0.5 mg/mL. After an incubation time of 2 h, unreacted dye and medium were removed and the 96-well plates were frozen at −80 °C for at least 30 min. To dissolve the purple formazan product 100 µL DMSO were added per well and the plate was incubated for 30 min at 37 °C with shaking. The wells were quantified by measuring absorbance at 590 nm with background correction at 630 nm using a microplate reader (TecanSpectrafluor Plus, Tecan, Switzerland). All studies were performed in quintuplicates. The relative cell viability (%) related to control wells treated only with

20 µL buffer (specified in the results sections) was calculated as ([A] test/[A] control) × 100 %.

2.20.5 Fluorescence microscopy

Cells were seeded in 96-well plates (Greiner bio-one) at a density of 4.000 cells/well. In case of KB_*wt* cells, wells were coated with collagen A prior to seeding. After 24 h medium was replaced with 80 µL fresh, serum-containing folate free RPMI medium. Then the various Atto647N labeled samples were prepared as described above, added into each well and incubated in case of targeted oligomers for 1 h at 37°C. Medium was removed and cells were incubated for 18 h in fresh serum containing folate free RPMI medium. Mixtures containing non-targeted oligomers were incubated for 15 h on the cells followed by 4 h incubation in fresh medium. Medium was replaced with PBS and cells were imaged using PerkinElmer Operetta® High Content Imaging System (Germany). For time series experiments, medium was replaced with DMEM without phenol red supplemented with 10 % FBS, 100 U mL^{-1} penicillin, 100 µg mL^{-1} streptomycin. Imaging was started either 1.5 h or 19 h after transduction. Cells were imaged for 2 h every 5 min followed by imaging every 15 min for 22 h.

2.20.6 Confocal microscopy

2.20.6.1 Nanobody/oligomer formulations

Cells were seeded in 8-well Nunc chamber slights (Thermo Scientific, Germany) at a density of 12.000 cells/well. In case of KB_*wt* cells, wells were coated with collagen A prior to seeding. After 24 h medium was replaced with 240 µL fresh, serum-containing folic acid free RPMI medium. Then the various samples were prepared as described above, added into each well and incubated for 1 h at 37 °C. Medium was removed and cells were incubated for 18 h in fresh serum containing folate free RPMI medium. Medium was replaced by PBS (pH 7.4) and cells were imaged using a Leica TCS SP8 confocal microscope with an 63x DIC oil immersion objective (Plan-Apochromat, Zeiss, USA).

2.20.6.2 Functionalized MOF nanoparticles

Cells were seeded in 8-Well Nunc chamber slights (Thermo Scientific, Germany) at a density of 12.000 cells/well. Wells were coated with collagen A prior to seeding. After 24 h medium was replaced with 240 µL fresh medium. The various samples were prepared as described above but in a final volume of 60 µL HBG (pH 7.4). 30 µg MOF NPs were functionalized with 0.3 nmol H_6-CF or H_6-GFP. In case of the co-delivery experiment, 0.15 nmol H_6-GFP were mixed with 0.15 nmol H_6-Tf* before the addition of 30 µg Zr-*fum* MOF NPs. The mixtures were added to the cells and incubated for 24 h. In case of HKUST-1 MOF NPs, the medium was changed after 2 h. Prior to imaging nuclei were stained with Hoechst dye. Medium was replaced by DMEM without phenol red supplemented with 10 % FBS, 100 U mL^{-1} penicillin, 100 µg mL^{-1} streptomycin and cells were imaged using a Leica TCS SP8 confocal microscope with an 63x DIC oil immersion objective (Plan-Apochromat, Zeiss, USA).

2.20.7 Determination of efficiencies of co-localization of nanobody and target protein

To evaluate efficiencies of nanobody delivery leading to specific co-localization of nanobody and target protein, experiments were carried out as has been described above for the screening experiments. To determine efficiencies, at least 500 cells were imaged using PerkinElmer Operetta® High Content Imaging System (Germany). Cells in which specific co-localization of nanobody and target protein was visible were counted. The percentage of cells in which co-localization of nanobody and target protein occurred was calculated as follows: (Number of cells with co-localization of nanobody and target protein / total number of cells) x 100%.

2.20.8 Flow cytometry

2.20.8.1 Cellular uptake experiments of nanobody/oligomer formulations

Cells were seeded in 24-well plates at a density of 30.000 cells/well. In case of KB_*wt* cells, wells were coated with collagen A prior to seeding. After 24 h medium was replaced with 400 µL fresh, serum-containing medium. For folic-acid competition

experiments, medium was changed to medium containing 100 µM folic acid, 30 min prior to the addition of the samples. The various samples were prepared as described above, diluted in HEPES buffer (pH 8.0) and 100 µL of the sample was added into each well at a final nanobody concentration of 3.6 µM and incubated for 1 h at 37 °C. Cells were put on ice, washed with PBS (pH 7.4), detached with trypsin/EDTA and diluted in cold PBS (pH 7.4) containing 10 % FBS. Cells were centrifuged and resuspended in PBS (10 % FBS, pH 4) to extinguish the outside fluorescence. The cellular fluorescence was assayed by excitation of fluorescein at 488 nm and detection of emission at 510 nm.

For long-time uptake experiments, medium was changed after 1 h incubation at 37 °C and cells were incubated for 18 h in fresh serum containing folate free RPMI medium. Cells were washed with PBS (pH 7.4), detached with trypsin/EDTA and diluted with fresh medium. After centrifugation the cells were taken up in PBS (10 % FBS, pH 7.4). The cellular fluorescence was assayed by excitation of Atto647N at 635 nm and detection of emission at 665 nm.

Cells were appropriately gated by forward/sideward scatter and pulse width for exclusion of doublets. DAPI (4′,6-diamidino-2-phenylindole) was used to discriminate between viable and dead cells. Data were recorded by Cyan™ ADP flow cytometer (Dako, Hamburg, Germany) using Summit™ acquisition software (Summit, Jamesville, NY) Gated cells (10.000 per sample) were collected. Analysis was done by FlowJo 7.6.5 flow cytometric analysis software. All experiments were performed in triplicates.

2.20.8.2 Cellular uptake experiments of functionalized MOF NPs

Cells were seeded in 24-well plates at a density of 20.000 cells/well. After 24 h, medium was replaced with 400 µL fresh medium. 0.5 nmol H_6-CF or H_6-GFP were diluted in HBG (pH 7.4), 50 µg MOF NPs (5 mg/mL in HBG) were added (final volume 50 µL) and the solution was strongly mixed. For the co-delivery of H_6-GFP and H_6-Tf* 0.25 nmol H_6-GFP and 0.25 nmol H_6-Tf* were pre-mixed in HBG (pH 7.4) before Zr-*fum* MOF NPs (5 mg/mL in HBG) were added (final volume 50 µL).

The mixture was incubated for 15 min at room temperature, diluted 1:1 with HBG (pH 7.4) and added to the cells. Cells were incubated for 24 h at 37 °C and 5 % CO_2

in a humidified incubator. In case of HKUST-1 MOF NPs, medium was changed after 2 h.

Cells were washed with PBS (pH 7.4), detached with trypsin/EDTA and diluted with fresh medium. Cells were centrifuged and resuspended in PBS containing 10 % FBS at pH 4 to quench extracellular fluorescence. The cellular fluorescence was assayed by excitation of fluorescein at 488 nm and detection of emission at 510 nm. For the co-delivery of H_6-GFP and H_6-Tf* the cellular fluorescence was also assayed by excitation of A647N at 635 nm and detection of emission at 665 nm.

Cells were appropriately gated by forward/sideward scatter and pulse width for exclusion of doublets. DAPI (4′,6-diamidino-2-phenylindole) was used to discriminate between viable and dead cells. Data were recorded by Cyan™ ADP flow cytometer (Dako, Hamburg, Germany) using Summit™ acquisition software (Summit, Jamesville, NY). Gated cells (10.000 per sample) were collected. Analysis was done by FlowJo 7.6.5 flow cytometric analysis software. All experiments were performed in triplicates. Mean fluorescence intensity (MFI) was calculated by FlowJo 7.6.5 flow cytometric analysis software and is depicted as normalization to HBG.

2.20.8.3 Determination of receptor status

Estimation of folate receptor status

Different cell lines were washed with PBS (pH 7.4), detached with trypsin/EDTA and diluted with fresh medium. Cells were centrifuged and resuspended in 100 µL PBS (10 % FBS, pH 7.4). Allophycocyanin (APC)-conjugated anti folic acid receptor 1 IgG1 antibody (10 µL; R&D Systems, USA) or IgG1 (Dako, Germany) (1:100 dilution) as isotype control were added. Cells were incubated for 1 h on ice, washed twice with PBS (10 % FBS, pH 7.4) and resuspended in 500 µL PBS (10 % FBS, pH 7.4). The amount of folate receptor positive cells was analyzed through excitation of APC at 635 nm and detection of emission at 665 nm. Cells were appropriately gated by forward/sideward scatter and pulse width for exclusion of doublets. DAPI (4′,6-diamidino-2-phenylindole) was used to discriminate between viable and dead cells. Data were recorded by Cyan™ ADP flow cytometer (Dako, Hamburg, Germany) using Summit™ acquisition software (Summit, Jamesville, NY). Analysis was done by FlowJo 7.6.5 flow cytometric analysis software.

Estimation of transferrin receptor status

HeLa_*wt* cells were washed with PBS (pH 7.4), detached with trypsin/EDTA and diluted with fresh medium. Cells were centrifuged and resuspended in 100 µL PBS (10 % FBS, pH 7.4). 1 µL mouse anti-hCD71 (Dako, Germany) (1:100 dilution) for detection of the transferrin receptor or IgG1 (Dako, Germany) (1:100 dilution) as isotype control were added, cells were incubated for 1 h on ice and washed twice with PBS (10 % FBS, pH 7.4). Cells were then stained with 0.5 µL Alexa Fluor 488Goat Anti -Mouse IgG(H+L) (Life technologies) as secondary antibody (1:200 dilution) for 1 h on ice, washed twice with PBS (10 % FBS, pH 7.4) and resuspended in 700 µL PBS (10 % FBS, pH 7.4). The cellular fluorescence was assayed by excitation at 488 nm and detection of emission at 510 nm. Cells were appropriately gated by forward/sideward scatter and pulse width for exclusion of doublets. DAPI (4′,6-diamidino-2-phenylindole) was used to discriminate between viable and dead cells. Data were recorded by Cyan™ ADP flow cytometer (Dako, Hamburg, Germany) using Summit™ acquisition software (Summit, Jamesville, NY). Analysis was done by FlowJo 7.6.5 flow cytometric analysis software.

2.20.9 Endocytosis inhibition assay

HeLa_*wt* cells were seeded in 24-Well plates at a density of 50.000 cells/well. After 24 h, medium was replaced with 400 µL fresh medium containing the different endocytosis inhibitors, chlorpromazine (5 µM, 10 µM, 20 µM), amiloride (1 mM, 2 mM, 5 mM) and genistein (100 µM, 150 µM, 200 µM). Cells were pre-incubated with the different inhibitors or at 4 °C for 30 min before addition of the H_6-GFP/Zr-*fum* MOF NPs. 0.5 nmol H_6-GFP were diluted in HBG (pH 7.4), 50 µg Zr-*fum* MOF NPs (5 mg/mL in HBG) were added (final volume 50 µL) and the solution was strongly mixed.

The mixture was incubated for 15 min at room temperature, diluted 1:1 with HBG (pH 7.4) and added to the cells. Cells were incubated for 2 h at 37 °C, 5 % CO_2 or at 4 °C.

Cells were washed with PBS (pH 7.4), detached with trypsin/EDTA and diluted with fresh medium. Cells were centrifuged and resuspended in PBS containing 10 % FBS

at pH 4 to quench extracellular fluorescence. The cellular fluorescence was assayed by excitation of fluorescein at 488 nm and detection of emission at 510 nm.
Cells were appropriately gated by forward/sideward scatter and pulse width for exclusion of doublets. DAPI (4′,6-diamidino-2-phenylindole) was used to discriminate between viable and dead cells. Data were recorded by Cyan™ ADP flow cytometer (Dako, Hamburg, Germany) using Summit™ acquisition software (Summit, Jamesville, NY). Five thousand gated cells per sample were collected. Analysis was done by FlowJo 7.6.5 flow cytometric analysis software. All experiments were performed in triplicates. Data is presented as % cellular uptake, of cellular uptake of Zr-*fum*/H_6-GFP NPs at 37 °C.

2.20.10 Delivery of pro-apoptotic peptides and cytochromeC

Cells were seeded in 96-Well plates at a density of 4.000 cells/well. After 24 h, medium was replaced with 80 µL fresh medium. 1 nmol of H_6-Bak, H_6-Bad, H_6-KLK or H_6-CytC was diluted in HBG (pH 7.4), 20 µg Zr-*fum* MOF NPs were added followed by strongly mixing of the samples. Controls were performed without the addition of Zr-*fum* MOF NPs. The mixtures were incubate for 15 min at room temperature, diluted 1:1 with HBG (pH 7.4, final volume 20 µL), added to the cells and incubated for 48 h at 37 °C and 5 % CO_2 in a humified incubator. Cell viability assay (MTT) was carried out as has been described above (2.20.4).

2.21 Statistical analysis

The statistical significances of experiments were analyzed using the t- test, **** $p<0.0001$, *** $p<0.0003$, ** $p<0.001$, * $p<0.01$.

3 Results

3.1 Intracellular delivery of nanobodies for imaging of target proteins in live cells

This chapter has been adapted from:

Intracellular Delivery of Nanobodies for Imaging of Target Proteins in Live Cells. Ruth Röder, Jonas Helma, Tobias Preiß, Joachim O. Rädler, Heinrich Leonhardt, Ernst Wagner. Pharmaceutical Research (2017), 34(1):161-174.

The following chapter describes the investigation of finding a potent carrier for the intracellular delivery of nanobodies for imaging of target proteins in live cells.

Potential intracellular molecular targets can be accessed in fixed and permeabilized cells only. Intracellular protein delivery may expand possible applications of nanobodies for the treatment of live cells for bioimaging and functional biological or therapeutic purposes. Besides, labeling of proteins, prior to their delivery is possible, broadening the scope of dyes which can be used from intracellular expressed fluorescent proteins to any desired marker.

For nanobody delivery, our investigations aimed at non-covalent interactions with oligomers for the following reasons. Due to the small nanobody size, covalent modification with dye and additional linkers appears to be problematic.

Nanobodies have a conserved core sequence, providing the beta-sheet based barrel-like domain structure. Variation occurs mostly in their complementarity determining regions (CDRs), which are responsible for specific antigen recognition [147]. This results in very similar structures with only slightly modified properties from adapting to target other proteins or molecules of interest.

When designing nanobody carriers directed towards target cells, various extra- and intracellular barriers have to be overcome. To ensure efficient nanobody delivery, the approach in the current work was to form stable nanoparticles by mixing nanobody with cationizable carrier oligomers.

Taking advantage of the above described quite conserved structural characteristics, I have analyzed sixteen different sequence-defined cationic oligoaminoamides (Table 5) [51, 141, 142, 148] from a library of more than 1000 oligomers for their potential to deliver nanobodies effectively into cells. I have investigated PEGylated as well as non-PEGylated carriers exhibiting different topologies. Carrier subunits comprise the diaminoethane building blocks Stp (succinoyl tetraethylene pentamine) or Sph

(succinoyl pentaethylene hexamine), and α,ε-amidated lysines as branching points. Optionally histidines as protonable buffering units or oleic acids to enhance endosomal escape, as well as cysteines which are supposed to serve for bioreversible crosslinkage of nanobody-bound oligomers, thus expected to stabilize the nanobody-oligomer network [50]. Ligand-PEG was included as functional shielding and cell targeting domain and glutamic acid as non-functional subunits.
The schematic formulation strategy is shown in Figure 5.

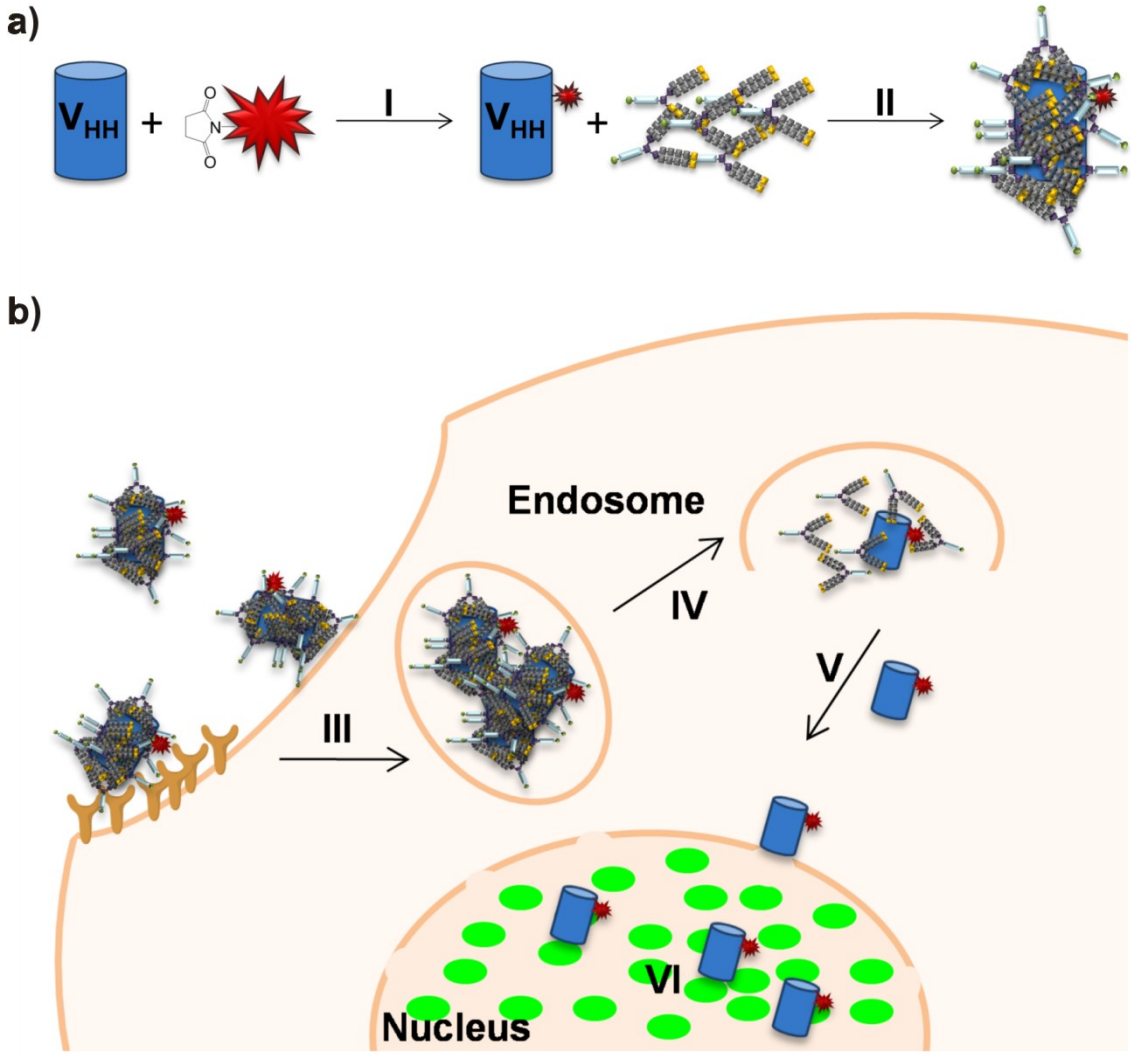

Figure 5: Schematic formulation strategy of nanobodies. a) After fluorescent labeling of the nanobody (I), the nanobody is mixed with a carrier oligomer leading to non-covalent interactions (II). b) The nanobody/oligomer nanoparticles are incubated with the cells leading to either receptor specific or non-specific cellular uptake (III). After endosomal escape and freeing from the oligomer (IV) the native nanobody can diffuse within the cell (V). In this scheme, diffusion into the nucleus and binding to focal PCNA-GFP as target structures in the nucleus is depicted (VI). Adapted from [59].

In order to visualize its cellular uptake and localization as well as its interaction with a target protein the nanobody was first labeled with a dye (I) followed by mixing and incubating with an oligomer (II) to form stable nanoparticles (Figure 5a). Thereafter the nanobody/oligomer complexes were incubated with the cells (Figure 5b), resulting in both receptor dependent and - independent cellular uptake (III). After successful endosomal escape (IV) the nanobody diffuses to its target protein (V) which can be visualized upon binding of the labeled nanobody (VI).
In the end, two related precise sequence-defined oligoaminoamide carriers (Figure 6) were found which are suitable to efficiently deliver different labeled nanobodies into cells.

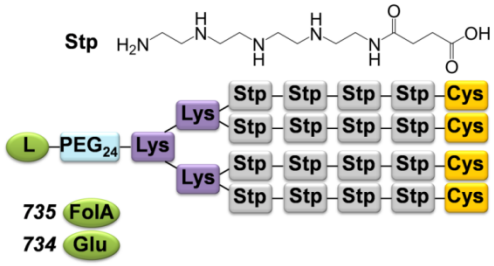

Figure 6: Structure of the 4-arm oligomers which showed the best delivery efficiency. ***735*** containing folic acid (FolA) as targeting ligand and ***734*** comprising glutamic acid instead of a targeting ligand; Stp, succinoyl tetraethylene pentamine; Lys, Cys, amino acids L-lysine, L-cysteine. Adapted from [59].

3.1.1 Heterologous expression and purification of GFP binding nanobody and lamin-nanobody

Both nanobodies (GFP binding nanobody (α-GFP-Nb) and lamin-nanobody (α-lamin Nb)) were expressed in *Escherichia coli* WK6 cells as has been described in [63, 64]. Given the fact that for the following delivery experiments quite a lot of nanobody was needed, expression and purification in larger scale was attempted. The purity of both nanobodies was investigated on SDS-gel after staining with Coomassie (α-GFP-Nb: Figure 7a; α-lamin-Nb: Figure 7b). Both nanobodies have a size of 13.7 kDa.
From 10 L *E. coli* WK6 culture 25 mg pure α-GFP-Nb were obtained. In case of α-lamin-Nb 30 mg were obtained from 4 L *E.coli* WK6 culture. Functionality of nanobodies was evaluated after modification with a dye (Atto647N NHS ester) by staining of their target proteins in different fixated cell lines (3.1.2).

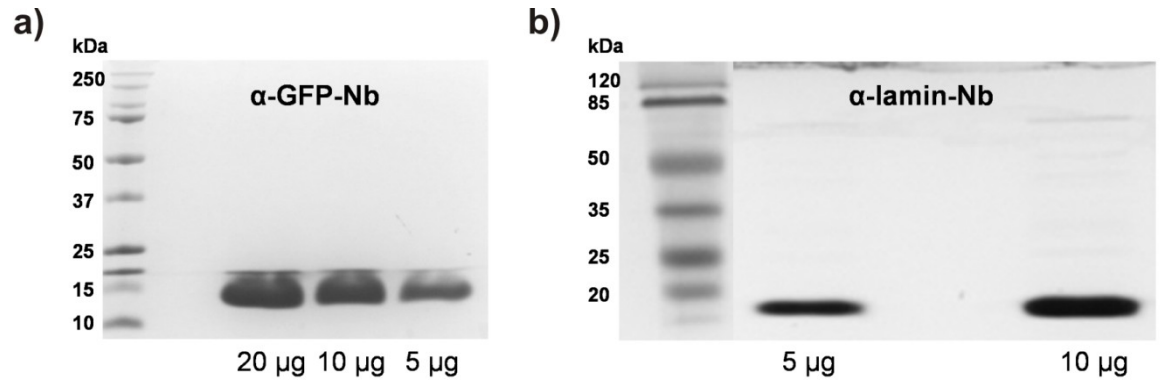

Figure 7: Analysis of purified nanobodies. After purification of nanobodies from *E.coli* WK6 cells, different amounts of nanobody were separated on a SDS-PAGE and stained with Coomassie. a) Purified α-GFP-Nb from left to right, Protein Ladder (Precision Plus Protein Standard, Bio-Rad, USA), 20 µg, 10 µg, 5 µg. b) Purified α-lamin-Nb from left to right, Protein Ladder (PEQ Lab Protein Marker III, Germany), 5 µg, 10 µg.

3.1.2 Evaluation of nanobodies and their molecular targets

For first general screening experiments, GFP was selected as a target protein. Delivery and binding of a α-GFP-Nb fused to a fluorescent protein - so called chromobodies [64] - to its target protein has recently been shown by Chiu *et al*. [149]. Furthermore, there are plenty of existing cell lines, where GFP has been fused to a variety of proteins with well-characterized subcellular localization, providing “visible” antigens to directly test the delivery of α-GFP-Nb in different subcellular compartments [63, 70, 72]. Secondly, lamin was selected as an endogenous target protein. It is localized at the nuclear membrane. Therefore, binding of the labeled lamin binding nanobody (α-lamin-Nb) results in the visualization of the typical round nuclear rim structure. Interaction of intracellular expressed lamin-chromobody with lamin had already been shown in *Drosophila melanogaster* S2 and HeLa cells [64].

Both nanobodies were fluorescently labeled with NHS-Atto647N by coupling to primary amines, i.e. lysine residues and N-terminal amino acids, and purified (Figure 8).

As can be seen in Figure 8 both nanobodies show clear bands when stained with Coomassie. Upon imaging at a wavelength of 646 nm a thick band at the specific size of the nanobodies of 13.7 kDa is visible. The faint band around 25 kDa could be a result of dimerization of nanobodies. But as the detection at 646 nm is far more sensitive than the Coomassie staining and the additional band is just visible at 646 nm it is negligible.

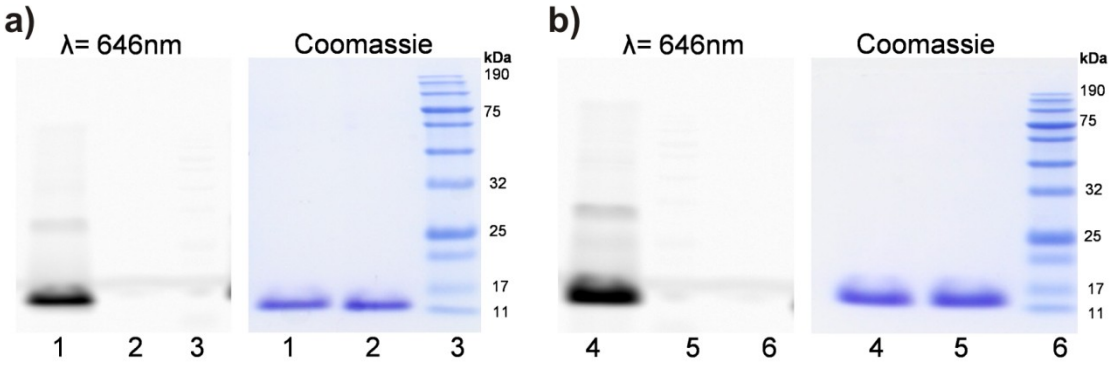

Figure 8: SDS-PAGE analysis of the modification of α-GFP-Nb (a) and α-lamin-Nb (b) with NHS-Atto647N dye. Grey pictures, imaging of gels at a wavelenght of 646 nm using Typhoon (GE Healthcare). Blue pictures, imaging of Coomassie staining. a) 1: Atto647N-labeled α-GFP-Nb 2: α-GFP-Nb without modification, 3: Protein Standard Broad Range (NEB); b) 4: Atto647N-labeled α-lamin-Nb 5: α-lamin-Nb without modification, 6: Protein Standard Broad Range (NEB). Adapted from [59].

To investigate if the binding affinity of nanobodies was not affected by dye coupling, staining of fixated cells was performed with both labeled nanobodies and four different folate receptor expressing cell lines, HeLa_PCNA-GFP, HeLa_Actin-GFP, HeLa_Tubulin-GFP, and KB_*wt* cells (Figure 10), which were later on used for the protein delivery experiments.

All cell lines were paraformaldehyde fixated and stained wih 0.5 µM Atto647N-labeled α-GFP-Nb (Figure 9a-c) or 0.5 µM Atto647N-labeled α-lamin-Nb (Figure 9d) to demonstrate that the modification of primary amines i.e. lysine residues and N-terminal amino acids of nanobodies with NHS-Atto647N does not affect specific binding to their target proteins.

Applying labeled α-GFP-Nb, specific staining could be shown for all three different GFP-tagged proteins (Figure 9a-c) Staining of KB_*wt* cells with labeled α-lamin-Nb lead to specific staining of endogenous lamin (Figure 9d), confirming that nanobody activity was not affected by dye coupling.

For the following screening experiments, amongst others, also oligomers targeted to the folate receptor should be used. Therefore the surface expression level of folic acid receptor in all used cell lines was investigated by flow cytometry using an Allophycocyanin (APC)-conjugated anti folic acid receptor 1 IgG1 antibody.

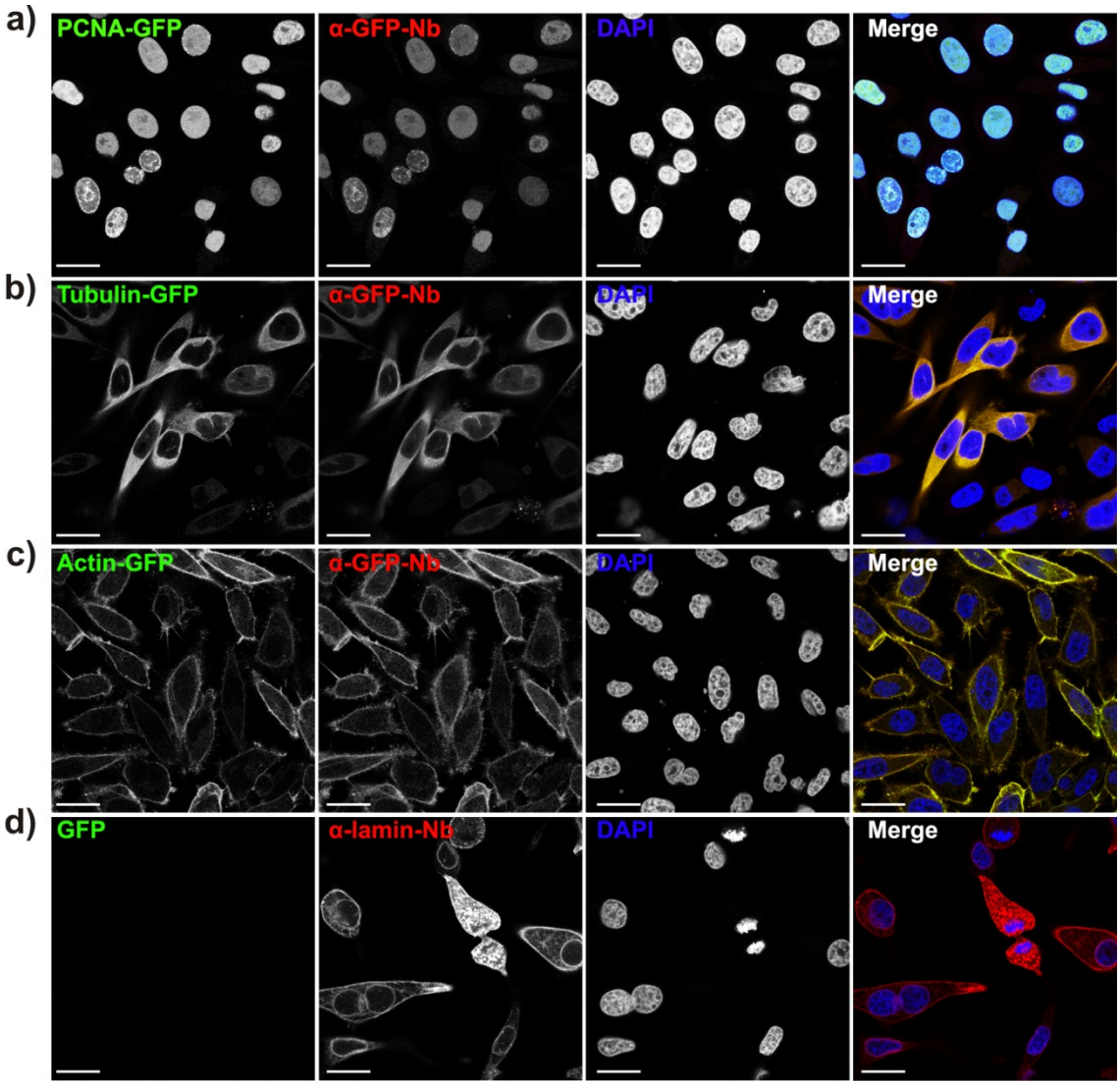

Figure 9: Staining of different paraformaldehyde fixated cell lines with Atto647N-labeled α-GFP-Nb or α-lamin-Nb. Paraformaldehyde fixated cell lines were stained wih 0.5 µM Atto647N-labeled α-GFP-Nb (a-c) or 0.5 µM Atto647N-labeled α-lamin-Nb (d) to demonstrate that the modification of primary amines i.e. lysine residues and N-terminal amino acids of nanobodies with NHS-Atto647N does not affect specific binding to their target proteins. First column, GFP fluorescence of GFP tagged proteins; second column, Atto647N fluorescence of labeled α-GFP-Nb or labeled α-lamin-Nb; third column, nuclear staining with DAPI; fourth column, merge of all three channels. Scale bars: 25 µm. a) Staining of HeLa_PCNA-GFP cells with α-GFP-Nb. b) Staining of HeLa_Tubulin-GFP cells with α-GFP-Nb. c) Staining of HeLa_Actin-GFP cells with α-GFP-Nb. d) Staining of KB_*wt* cells with α-lamin-Nb. Adapted from [59].

Figure 10 shows enhanced expression of folic acid receptor in all different cell lines. KB_*wt* cells show the highest expression level (blue) followed by HeLa_PCNA-GFP cells (red). HeLa_Tubulin-GFP and HeLa_Actin-GFP cells show slightly lower expression levels.

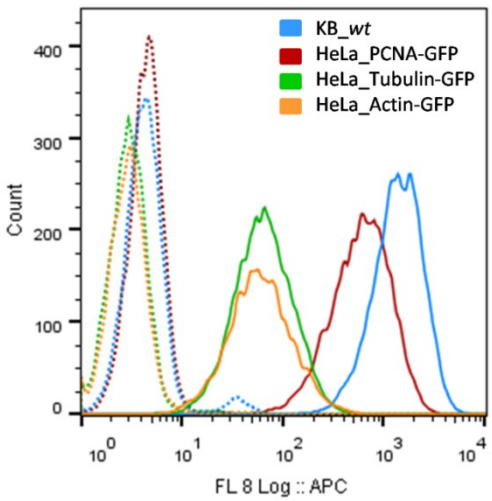

Figure 10: Determination of the surface expression level of the folic acid receptor in different cell lines by flow cytometry. Control cells (dotted lines) were treated with isotype control, mouse IgG1. Allophycocyanin (APC)-conjugated anti folic acid receptor 1 IgG1 antibody was used for the detection of the folic acid receptor (solid lines). Blue, KB_*wt*; red, HeLa_PCNA-GFP; green, HeLa_Tubulin-GFP; orange, HeLa_Actin-GFP. Adapted from [59].

3.1.3 Screening of different oligomers for nanobody delivery

Dye modified nanobody on its own does not diffuse into live cells, as it is shown in Figure 11.

For effective delivery of α-GFP-Nb into living cells, cationizable oligomers from an existing library of cationic oligoaminoamides were screened (Table 5).

All oligomers had been synthesized by solid-phase supported synthesis to gain well defined chemical structures and topologies. For the library screen, labeled α-GFP-Nb was mixed with different oligomers and incubated at 37 °C for 4 h to form non-covalent nanobody/oligomer formulations as explained above. HeLa_PCNA-GFP cells [64, 138] exhibiting a nucleoplasmic epitope were used to investigate protein delivery efficiency. Cells were incubated with two different amounts of labeled α-GFP-Nb/oligomer mixtures (final concentration of 1.5 µM and 3.6 µM nanobody). The formulations were prepared in HEPES buffer (pH 8.0) and incubated on cells in folate-free, but serum containing medium. Folate-free medium was used to ensure that folate receptors can be accessed by the folate targeted oligomers without folate competition. All nanobody/oligomer formulations were tested at molar ratios of 1:1, 1:5 and 1:10. As the molar ratios of 1:1 and 1:10 did not lead to an as efficient cellular uptake, just the results of the 1:5 ratio are presented in this work.

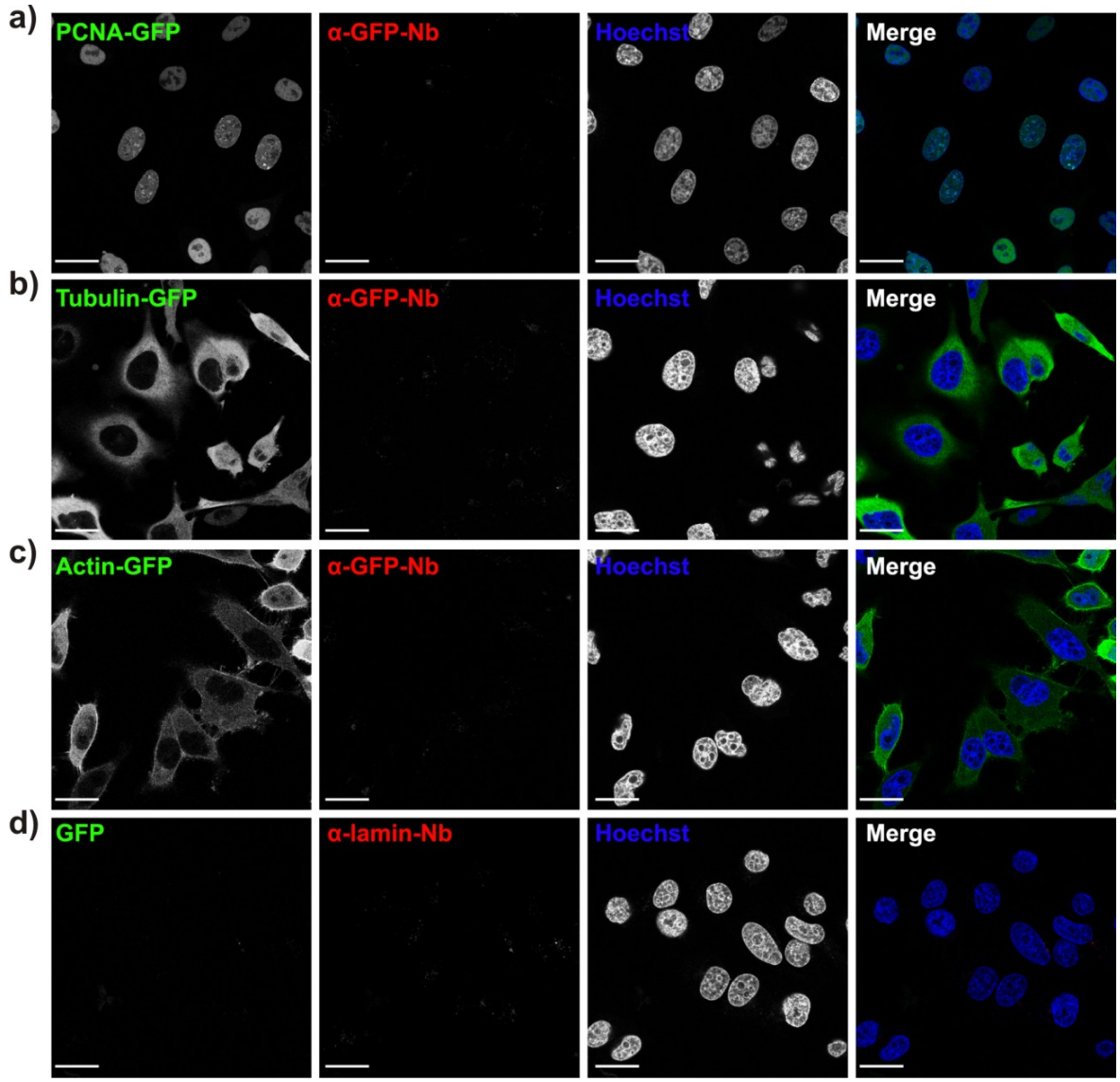

Figure 11: Confocal laser scanning microscopy of live cells incubated with pure Atto647N-labeled α-GFP-Nb or α-lamin-Nb. Different cell lines were incubated with 3.6 µM Atto647N-labeled α-GFP-Nb (a-c) or α-lamin-Nb (d) for 18 h, followed by 4 h incubation in fresh media. First column, GFP fluorescence of GFP tagged proteins; second column, Atto647N fluorescence of α-GFP-Nb or α-lamin-Nb; third column, nuclear staining with Hoechst dye; fourth column, merge of all three channels. Scale bars: 25 µm. a) HeLa_PCNA-GFP cells; b) HeLa_Tubulin-GFP cells; c) HeLa_Actin-GFP cells; d) KB_*wt* cells. Adapted from [59].

An overview of cellular uptake and effective delivery leading to specific binding of intracellular PCNA-GFP is given in Table 5.

Cellular uptake was considered to be positive if α-GFP-Nb was visualized inside cellular vesicles. It is marked with "+" in Table 5 "Cellular uptake". Co-localization of α-GFP-Nb and PCNA-GFP in the nucleus was regarded as specific binding to target protein and is marked with "+" in Table 5 "Specific binding to target protein". "+-" describes the fact that delivery experiments using α-GFP-Nb formulated with ***730*** or ***731*** at a molar ratio of five, lead to co-localization with PCNA-GFP, but the signal was

far less intense than if oligomer ***734*** or ***735*** were used. The delivery of α-GFP-Nb at a final concentration of 1.5 µM did not result in any significant cellular uptake and therefore just the results for a final concentration of 3.6 µM are depicted in Table 5. A more detailed description of the structures can be found in [142].

Table 5: Summary of oligoaminoamide oligomers used for nanobody delivery.

ID	Topology	Sequence (C-to N- terminal)	Cellular uptake	Specific binding to target protein	Ref
392		A-K-(K-(Stp_3-C)$_2$)$_2$	-	-	[51]
402		A-K-(K-(Stp_4-C)$_2$)$_2$	-	-	[51]
606		A-K-[H-K-(H-Sph-Sph-H-Sph-H-C)$_2$]$_2$	+	-	[141]
730		K-(PEG_{24}-E)-K-(K-$OleA_2$)-K(Stp_4-C)$_2$	+	+-	[144]
731	4-arm	K-(PEG_{24}-FolA)-K-(K-$OleA_2$)-K(Stp_4-C)$_2$	+	+-	[144]
732		K-(PEG_{24}-E)-K-[K-(Stp_3-C)$_2$]$_2$	+-	-	[142]
733		K-(PEG_{24}-FolA)-K-[K-(Stp_3-C)$_2$]$_2$	+-	-	[142]
734		K-(PEG_{24}-E)-K-[K-(Stp_4-C)$_2$]$_2$	+	+	[142]
735		K-(PEG_{24}-FolA)-K-[K-(Stp_4-C)$_2$]$_2$	+	+	[142]
728		K-(PEG_{24}-E)-K-(Stp_4-C-K-$OleA_2$)$_2$	+	-	[53]
729		K-(PEG_{24}-FolA)-K-(Stp_4-C-K-$OleA_2$)$_2$	+	-	[53]
737	2-arm	K-(PEG_{24}-FolA)-K-(Stp_4-C)$_2$	-	-	[53]
788		K-(PEG_{24}-E)-K-[(H-Stp)$_3$-H-C]$_2$	-	-	[142]
789		K-(PEG_{24}-FolA)-K-[(H-Stp)$_3$-H-C]$_2$	-	-	[142]
488	U-shape	K-(Stp_4-K-(K-$OleA_2$)-C)$_2$	-	-	[50]
622	comb structure	C-[K(Stp)]$_8$-C	+	-	[148]

ID: identification number of oligomers. PEG_{24}: polyethylene glycol containing 24 ethylene oxide monomer units, FolA: folic acid, OleA: oleic acid, SuccA: succinic acid, Stp: succinoyl tetraethylene pentamine, Sph: succinoyl pentaethylene hexamine, A, C, E, H, K: amino acids; +: positive effect, -: negative effect, + -: indicating a slight effect

As a result of the analysis, larger oligomers (4-arm structures) lead to better cellular uptake than smaller oligomers (2-arm, U-shape or comb structures). Oligomers comprising histidines or Sph did not improve cellular uptake or release of cellular vesicles. Transductions using 3.6 µM labeled α-GFP-Nb formulated with ***735*** at a molar ratio of 1:5 resulted in the highest efficiency in specific binding of PCNA-GFP in the nucleus (binding of nuclear PCNA-GFP in 40 % of the cells, 3.1.7, Table 6). 3.6 µM of the α-GFP-Nb formulation with ***734***, the non-targeted counterpart of ***735***,

also lead to intracellular binding of PCNA-GFP, but with a slightly lower efficiency of 30% (3.1.7, Table 6).

3.1.4 Investigation of nanobody/oligomer nanoparticles using FCS

The interaction of nanobody and the two most effective oligomers was investigated using fluorescence correlation spectroscopy (FCS). FCS is a highly sensitive single-molecule technique for measuring hydrodynamic radii of fluorescent molecules or particles in highly diluted solutions in the nanomolar concentration range [150]. The normalized results are shown in Figure 12.

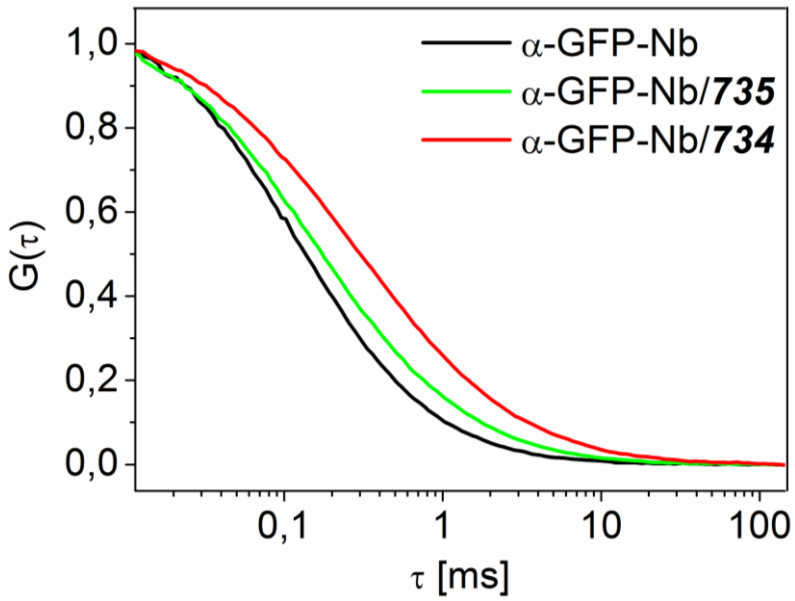

Figure 12: Fluorescent correlation spectroscopy of α-GFP-Nb and oligomers. Non-labeled nanobodies spiked with 1 % Atto647N-labeled nanobodies were mixed with ***735*** or ***734*** at a molar ratio of 1:5 and incubated for 4 h at 37 °C. Normalized average correlation curves show R_H of 2 nm for non-formulated nanobody (black), R_H of 15 nm – 20 nm for nanobody/***735*** nanoparticles (green) or nanobody/***734*** nanoparticles (red). Measurements were carried out by Dr. Tobias Preiß (Faculty of Physics, LMU München). Adapted from [59].

The GFP-binding nanobody possesses a hydrodynamic radius (R_H) of 2 nm which fits well with its published size of 2 nm x 4 nm [63]. The formulation of α-GFP-Nb/***735*** at a molar ratio of 1:5 resulted in a homogenous solution containing two particle fractions; one with a R_H of 15 nm consisting of complexes of multiple Nbs with ***735***, and one fraction with a R_H of 2 nm presenting just slightly or not modified monomeric nanobody. In case of the α-GFP-Nb/***734*** mixtures a slightly different R_H of 20 nm for the nanoparticles was found.

3.1.5 Terminal cysteines are important for nanoparticle formation

Additionally, the importance of incorporated terminal cysteines within the oligomeric structure was evaluated by comparing samples of α-GFP-Nb/***735*** or /***734*** mixtures with free cysteines to samples where the terminal cysteines were blocked by N-ethylmaleimide (NEM) (Figure 13) using FCS. After modification of the terminal cysteines, only particles of the size of monomeric nanobodies were found. Thus no stable binding of nanobody with oligomer could be observed. To confirm these findings, microscopy was performed using NEM modified oligomers ***735*** and ***734*** (data not shown)***.*** Consistent with FCS measurements, no cellular uptake or binding to intracellular PCNA-GFP was found, leading to the assumption that cysteines are absolutely essential for nanoparticle stabilization.

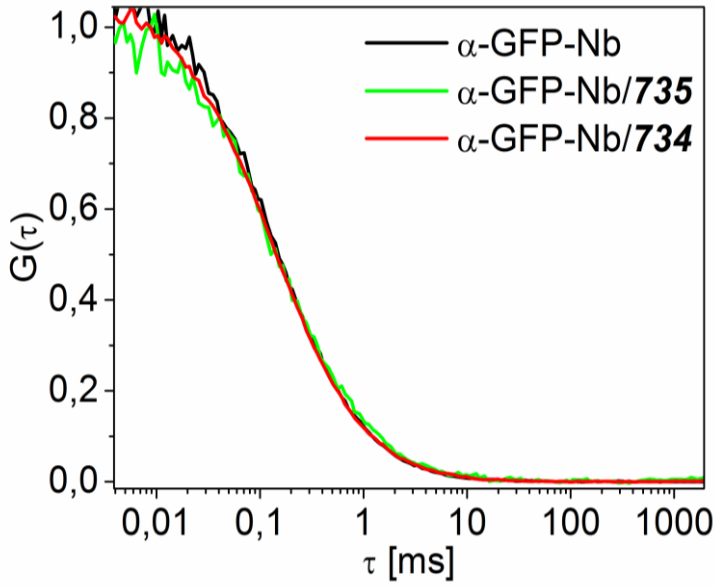

Figure 13: Fluorescence correlation spectroscopy of α-GFP-Nb and oligomers with NEM blockade. α-GFP-Nb spiked with 1% Atto647N-labeled α-GFP-Nb was mixed with oligomer ***735*** or ***734*** with NEM blockade at a molar ratio of 1:5 and incubated for 4 h at 37°C. Fluorescent correlation spectroscopy measurements were carried out at a final concentration of α-GFP-Nb of 0.5 mg/mL in HEPES buffer. Normalized average correlation curves show R_H of 2 nm for α-GFP-Nb (black) and no change in correlation curves upon incubation with ***735*** (green) or ***734*** (red) indicating that free terminal cysteines are absolutely essential for the formation of α-GFP-Nb/oligomer nanoparticles. Measurements were carried out by Dr. Tobias Preiß (Faculty of Physics, LMU München). Adapted from [59].

To further investigate the mechanism of nanoparticle formation, the oxidation of free cysteines of oligomer ***735*** and ***734*** was followed during the 4 h incubation time (Figure 14). A continuous oxidation could be observed resulting in a final oxidation of 90 % of the thiols.

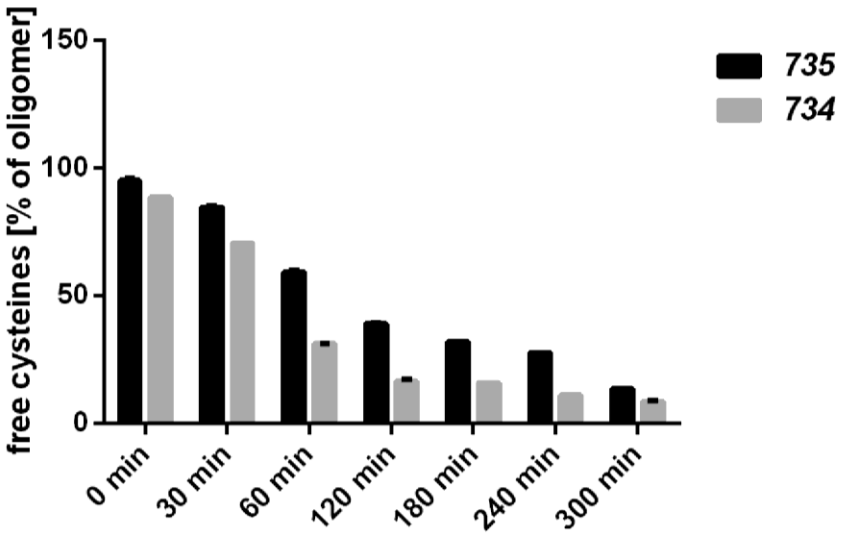

Figure 14: Investigation of thiol oxidation during nanobody/oligomer nanoparticle formation. The oxidation of free thiols during the formation of nanobody/oligomer nanoparticles was investigated over a period of 4 h. α-GFP-Nb was mixed with oligomer ***735*** or ***734*** at a molar ratio of 1:5 and incubated for 4 h at 37°C. At the indicated time points, samples were drawn and the amount of free thiols was determined by Ellman's assay. The percentage of free cysteines left in the reaction was calculated ± SD (*n*=3). Black bars, nanobody/***735***; grey bars, nanobody/***734***. Adapted from [59].

3.1.6 Targeting efficiency of oligomer *735*

To evaluate the folate receptor specific uptake of the nanobody/***735*** formulations, cellular internalization experiments on KB_*wt* cells were carried out. The α-GFP-Nb was labeled with carboxyfluorescein (α-GFP-Nb-CF). Fluorescein loses its fluorescence at acidic pH [151]. Thus the selection of this dye allows quenching of the fluorescence of extracellular bound nanobody by performing the measurement in acidic buffer. Cells were incubated with 3.6 µM α-GFP-Nb-CF formulated with oligomers ***735*** or ***734*** at a molar ratio of 1:5 for 45 min and uptake efficiency was determined by flow cytometry (Figure 15). The targeting ligand containing nanobody/***735*** nanoparticles showed enhanced cellular uptake compared to the folate-free nanobody/***734*** formulations (Figure 15a). To verify if nanoparticles are specifically taken up via the folate receptor, folate competition experiments were carried out. Cells were pre-incubated with saturating 100 µM folic-acid before the uptake experiments. As it is depicted in Figure 15b, short-time uptake of α-GFP-Nb-CF/***735*** could be inhibited by the addition of folic acid.

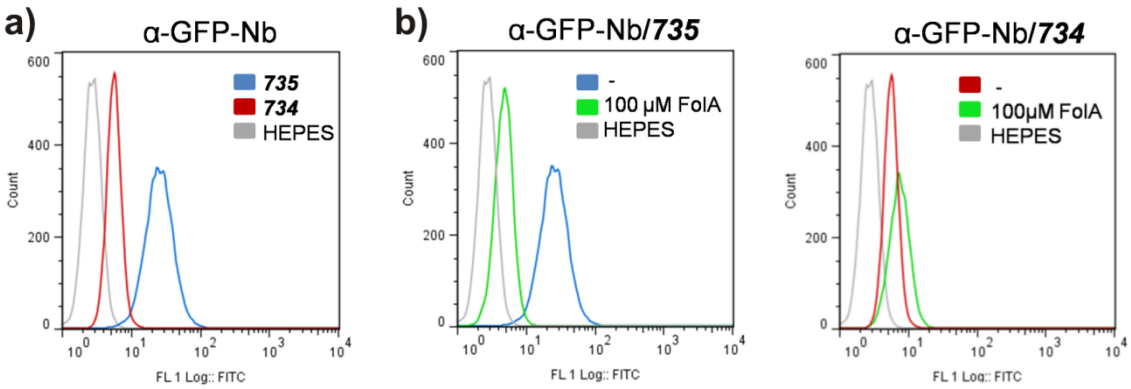

Figure 15: Cellular internalization of carboxyfluorescein (CF) modified α-GFP-Nb. CF-nanobodies were mixed with oligomer ***735*** or ***734*** at a molar ratio of 1:5 and incubated for 4 h at 37 °C. a) KB_*wt* cells were transduced with 3.6 µM nanobody/***735*** (blue) or /***734*** (red). After 1 h incubation at 37 °C cellular internalization was determined by flow cytometry. b) Free folic acid competition experiments: KB_*wt* cells were pre-incubated for 30 min with 100 µM free folic acid. Afterwards cells were transduced with 3.6 µM α-GFP-Nb/***735*** (left) or 3.6 µM α-GFP-Nb/***734*** (right). After 45 min incubation at 37 °C, cellular internalization was determined by flow cytometry. Green, with 100 µM folic acid inhibition; blue or red, without folic acid inhibition; grey, control incubation of cells with HEPES buffer. Adapted from [59].

Although comparison of cellular internalization experiments using oligomers ***735*** and ***734*** after 45 min showed higher uptake efficiency using the folic acid modified oligomer ***735***, flow cytometry analysis (Figure 16) and microscopic examination (3.1.7, Figure 19) of the cells after 19 h, also resulted in a quite high uptake of non-targeted nanobody/***734*** nanoparticles.

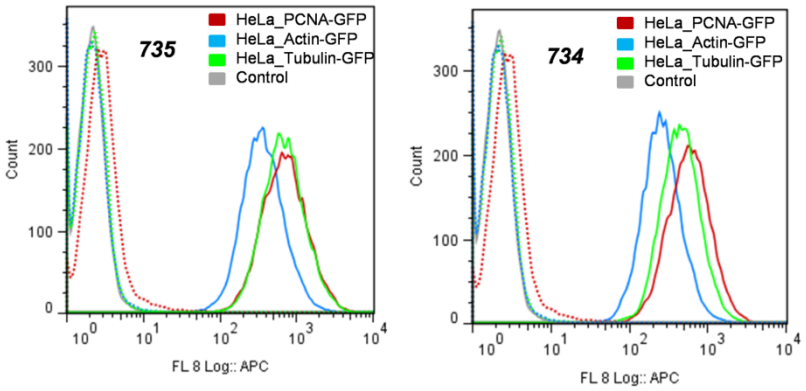

Figure 16: Flow cytometric analysis of cellular uptake of α-GFP-Nb/*735* or *734* after 19 h. Atto647N-labeled α-GFP-Nb was mixed with oligomer ***735*** or ***734*** at a molar ratio of 1:5 and incubated for 4 h at 37 °C. Afterwards cells were incubated for 1 h with 3.6 µM labeled nanobody formulated with oligomer ***735*** (left) or oligomer ***734*** (right) (solid lines) or pure nanobody (dotted lines), followed by 18 h incubation in fresh media. Cellular uptake of α-GFP-Nb into different recombinant HeLa cell lines was investigated. Red, HeLa_PCNA-GFP cells; blue, HeLa_Actin-GFP cells; green, HeLa_Tubulin-GFP cells; grey, exemplary HEPES control in HeLa_PCNA-GFP cells. Adapted from [59].

Additionally, the zeta potential of all nanobody/oligomer formulations was evaluated, showing a positive zeta potential of ~+15 mV.

3.1.7 Evaluation of specific binding of GFP binding nanobody to target proteins

Figure 17 depicts the transduction of Atto647N-labeled α-GFP-Nb using oligomer ***735*** into HeLa_PCNA-GFP cells. Cells were incubated with α-GFP-Nb/***735*** at a molar ratio of 1:5 for 1 h followed by incubation in fresh media for 18 h.

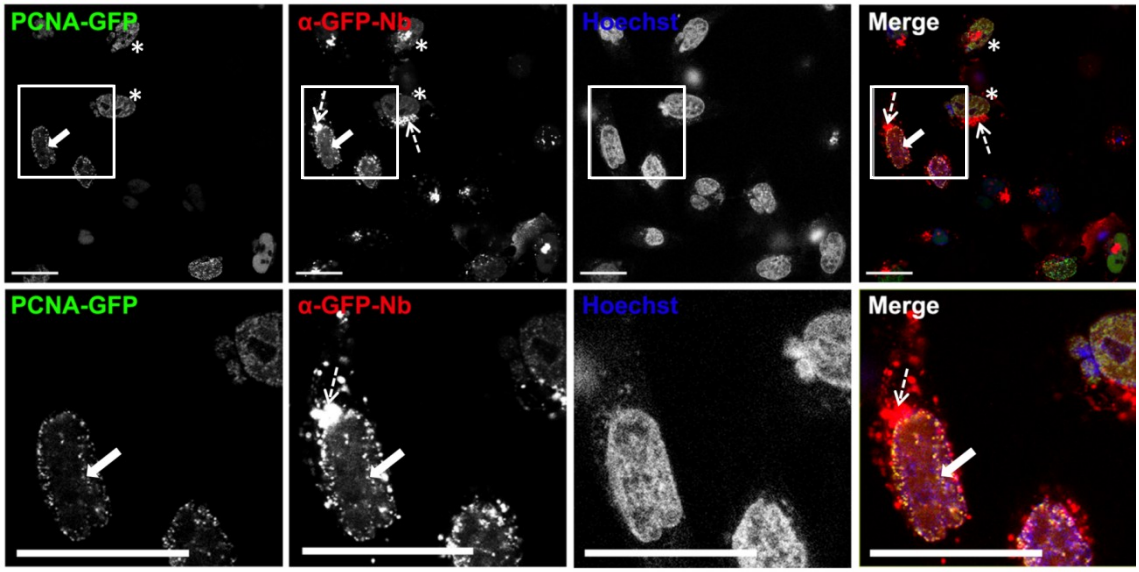

Figure 17: Confocal laser scanning microscopy of live cells after transduction with α-GFP-Nb/*735*. HeLa_PCNA-GFP cells were incubated for 1 h with 3.6 µM Atto647N-labeled α-GFP-Nb formulated with oligomer ***735*** at a molar ratio of 1:5, followed by 18 h incubation in fresh media. First column, GFP fluorescence of GFP tagged proteins; second column, Atto647N fluorescence of α-GFP-Nb; third column, nuclear staining with Hoechst dye; fourth column, merge of all three channels. Scale bars: 25 µm.
Thick arrows indicate cells in S Phase where the typical punctuated patterns of PCNA-GFP at the replication foci is visible. Stars indicating cells in G1 and G2 phase; dashed arrows (second and fourth column) exemplary indicating nanoparticles being trapped in cellular vesicles. Adapted from [59].

In the pictures of the first column the specific punctuated pattern of concentrated PCNA-GFP at replication foci (thick arrows) as it is visible in S-phase and the diffuse pattern (white stars) indicating the G1- and G2-phase is visible. The second pictures depict the co-localization of the specific pattern of PCNA-GFP and α-GFP-Nb at the replication foci (thick arrows), but also co-localization of α-GFP-Nb and PCNA-GFP in G1 and G2 (white stars), indicating binding of the nanobody to its GFP-tagged target protein through the whole cell cycle.

The delivery efficiency of the selected α-GFP-Nb/oligomer nanoparticles was furthermore investigated on HeLa_Actin-GFP and HeLa_Tubulin-GFP cells, exhibiting two different targets at the cytoskeleton. Transduction experiments were carried out with 3.6 µM Atto647N-labeled Nb formulated with ***735*** at a molar ratio of

1:5, as has been described above for HeLa_PCNA-GFP cells. Figure 18a displays the delivery into HeLa_Actin-GFP and Figure 18b into HeLa_Tubulin-GFP cells.

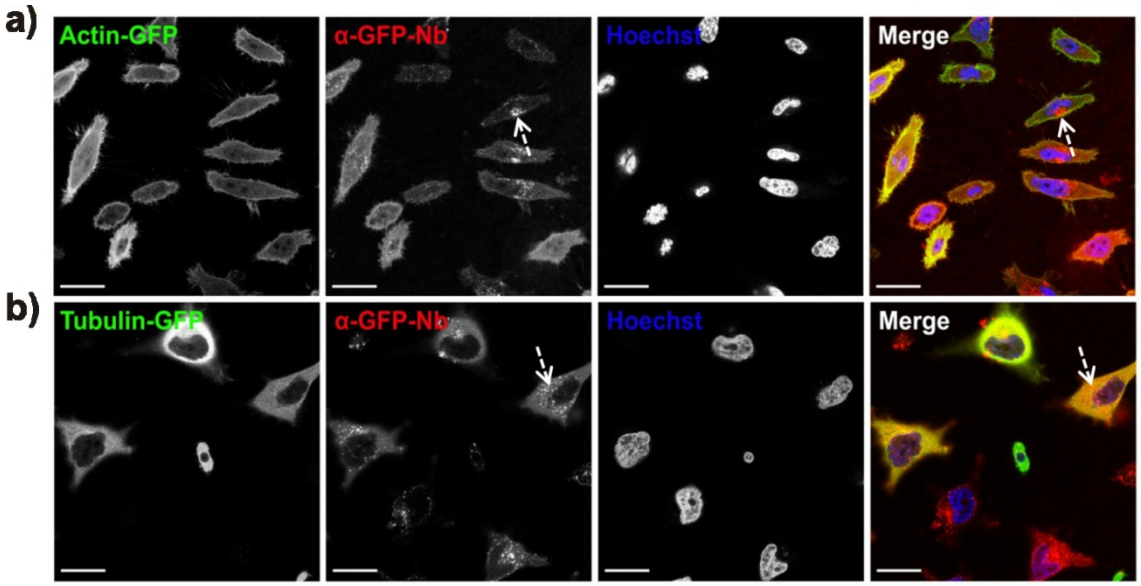

Figure 18: Confocal laser scanning microscopy of live cells after transduction with α-GFP-Nb/*735*. Different recombinant HeLa cell lines were incubated for 1 h with 3.6 µM Atto647N labeled α-GFP-Nb formulated with oligomer ***735*** at a molar ratio of 1:5, followed by 18 h incubation in fresh media. First column, GFP fluorescence of GFP tagged proteins; second column, Atto647N fluorescence of α-GFP-Nb; third column, nuclear staining with Hoechst dye; fourth column, merge of all three channels. Dashed arrows indicate exemplary nanoparticles being trapped in cellular vesicles. Scale bars: 25 µm. a) HeLa_Actin-GFP cells; b) HeLa_Tubulin-GFP cells. Adapted from [59].

In both cell lines specific co-localization of α-GFP-Nb (second row) with GFP tagged proteins (first row) can be seen. This demonstrates the versatility of the delivery approach. Images applying the non-targeted oligomer ***734*** as delivery agent are depicted in Figure 19. The experiment was carried out as has been described above for nanobody/**735** mixtures. Incubation of nanobody/**734** mixtures for 1h on the cells followed by 18 h incubation in fresh media, also resulted in quite high uptake efficiencies, similar to the above described flow cytometry experiments (Figure 16). Apart from specific binding of the α-GFP-Nb to target proteins, Figure 17-19 (second column) display small intense dots (dashed arrows). These dots are oligomer/protein nanoparticles still being entrapped in cellular vesicles, indicating the escape from these endolysosomal vesicles as the main bottleneck. Additionally, the efficiency of specific binding to target protein was determined by microscopic evaluation of at least 500 cells per value (Table 6). Cells in which specific co-localization of nanobody and target protein was visible were counted. The percentage of cells in which co-localization of nanobody and target protein occurred was calculated as follows:

(number of cells with co-localization of nanobody and target protein/total number of cells) x 100%. This resulted in specific co-localization of nanobody and GFP-tagged proteins in 40 % of HeLa_PCNA-GFP, 60 % of HeLa_Tubulin-GFP and 50 % of HeLa-Actin-GFP cells.

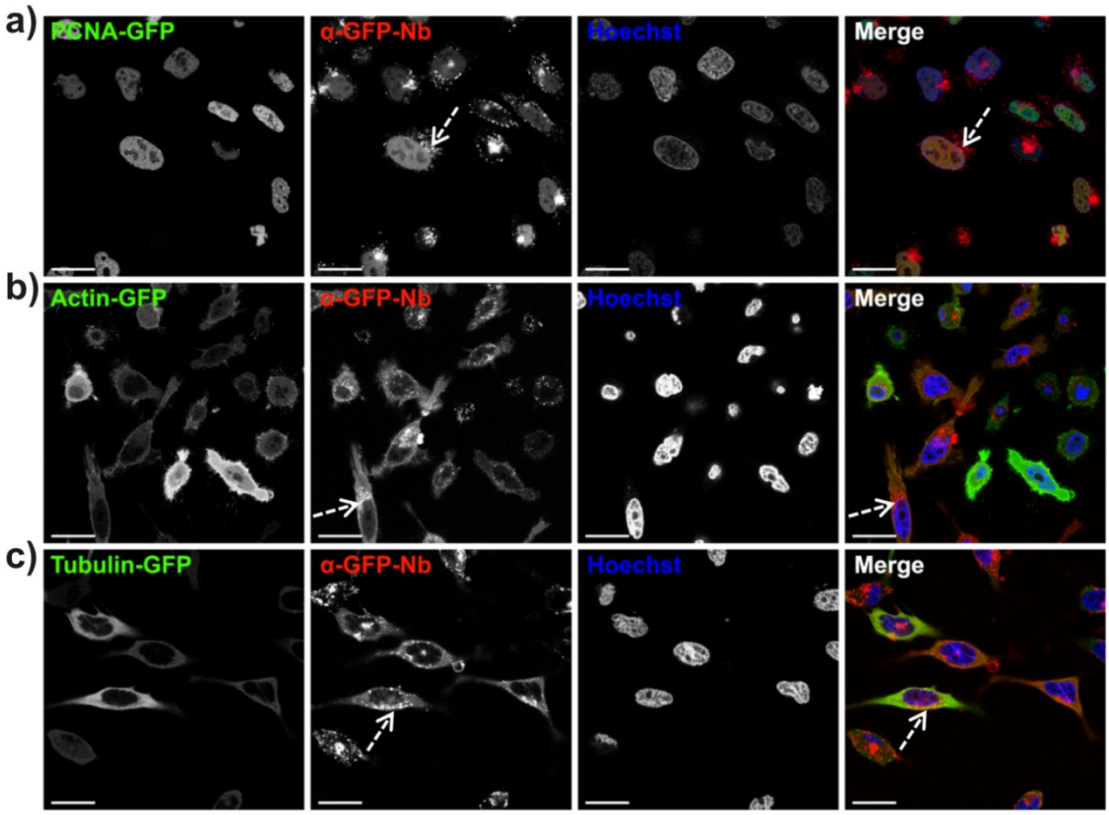

Figure 19: Confocal laser scanning microscopy of live cells after transduction with α-GFP-Nb/*734*. Different recombinant HeLa cell lines were incubated for 1 h with the 3.6 µM Atto647N labeled α-GFP-Nb formulated with ***734*** at a molar ratio of 1:5, followed by 18 h incubation in fresh media. First column, GFP fluorescence of GFP tagged proteins; second column, Atto647N fluorescence of α-GFP-Nb; third column, nuclear staining with Hoechst dye; fourth column, merge of all three channels. Dashed arrows indicate exemplary nanoparticles being trapped in cellular vesicles. Scale bars: 25 µm. a) HeLa_PCNA-GFP cells; b) HeLa_Actin-GFP cells; c) HeLa_Tubulin-GFP cells. Adapted from [59].

Table 6: Efficiencies of co-localization of nanobody and target protein

HeLa_PCNA-GFP **α-GFP-Nb**		HeLa-Actin-GFP **α-GFP-Nb**		HeLa_Tubulin-GFP **α-GFP-Nb**		KB_*wt* **α-lamin-Nb**	
735	***734***	***735***	***734***	***735***	***734***	***735***	***734***
50%	30%	60%	30%	50%	35%	70%	40%
40%	20%	40%	35%	60%	50%	60%	40%
35%	20%	60%	40%	70%	50%	50%	30%
Average							
40%	**30%**	**50%**	**35%**	**60%**	**45%**	**60%**	**40%**

Evaluation of at least 500 cells per value. Cells in which specific co-localization of nanobody and target protein was visible were counted. The percentage of cells in which co-localization of nanobody and target protein occurred was calculated as follows: (number of cells with co-localization of nanobody and target protein/total number of cells) x 100%.

3.1.8 Evaluation of cytotoxicity of nanobodies and oligomers *735* and *734*

Metabolic activity was determined for HeLa_PCNA-GFP, _Actin-GFP, _Tubulin-GFP and KB_*wt* cells by a dimethylthiazolyldiphenyltetrazolium bromide (MTT) assay. Therefore nanobodies were formulated with oligomer ***735*** or ***734*** at a molar ratio of 1:5, and formulations were incubated for 1 h on the cells followed by 18 h incubation in fresh medium. α-GFP-Nbs were used for all recombinant HeLa cell lines and α-lamin-Nb for KB_*wt* cells, showing absence of significant toxicity for the used nanobodies and the oligomer/nanobody formulations under the applied conditions (Figure 20).

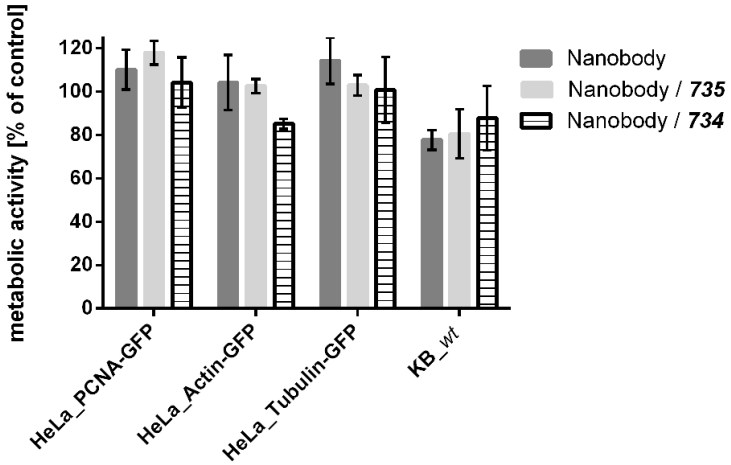

Figure 20: Evaluation of cytotoxicity of nanobody formulated with oligomer *735* or *734.* Nanobody was formulated with oligomer ***735*** or ***734*** at a molar ratio of 1:5. Cells were incubated for 1 h with the protein/oligomer mixture at a final nanobody concentration of 3.6 µM, followed by 18 h incubation in fresh media. Dark grey, free nanobody; light grey, transduction of cells with nanobody/***735***, patterned, transduction of cells with nanobody/***734***. Atto647N-labeled α-GFP-Nb was used for all recombinant HeLa cell lines and Atto647N-labeled α-lamin-Nb for KB_*wt* cells. Data are presented as % metabolic activity of control cells ± SD (*n*=5). Adapted from [59].

3.1.9 Application of the delivery strategy to a lamin binding nanobody

Taking advantage of the fact that nanobodies exhibit low variations in terms of size, structure and surface properties, the delivery strategy outlined above should be easily transferable to various other nanobodies. To investigate this, the delivery of a lamin binding nanobody (α-lamin-Nb) into KB_*wt* cells was evaluated. First, the association of Atto647N-labeled α-lamin-Nb with either oligomer ***735*** or ***734*** in HEPES buffer (pH 8.0) after incubation for 4 h at 37 °C was investigated by FCS (Figure 21), giving similar results as for α-GFP-Nb (3.1.4, Figure 12).

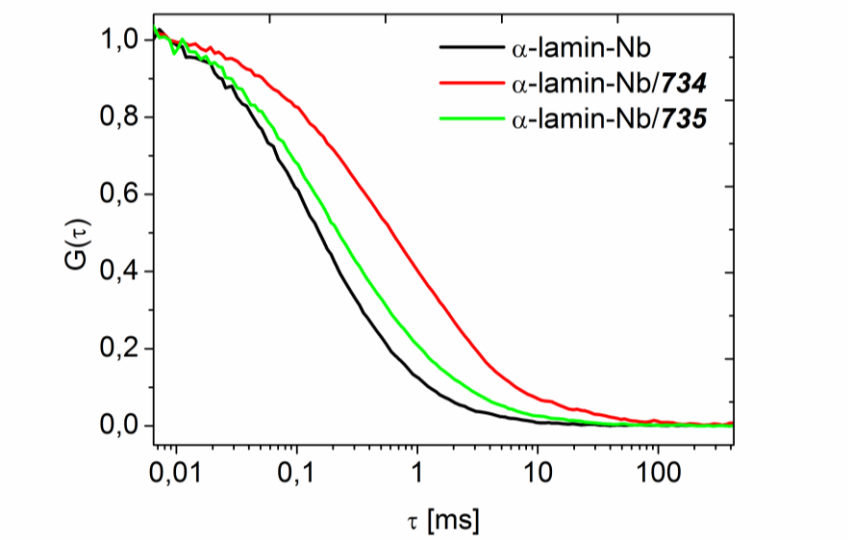

Figure 21: Fluorescent correlation spectroscopy of α-lamin-Nb and oligomers. Non-labeled nanobodies spiked with 1% Atto647N-labeled nanobodies were mixed with oligomer ***735*** or ***734*** at a molar ratio of 1:5 and incubated for 4 h at 37 °C. Normalized average correlation curves show R_H of 2 nm for non-formulated nanobody (black), R_H of 15 nm – 20 nm for nanobody/***735*** nanoparticles (green) or nanobody/***734*** nanoparticles (red). Adapted from [59].

The labeled α-lamin-Nb was found to have a R_H of 2 nm, α-lamin-Nb/oligomer mixtures resulted in two fractions with R_H of 2 nm for non-bound or modified monomeric α-lamin-Nb, and R_H of 20 nm for formulated α-lamin-Nb/oligomer.

For transduction experiments, Atto647N-labeled α-lamin-Nb/oligomer formulations were incubated for 1 h on the cells at a final concentration of 3.6 µM nanobody in serum containing folate-free RPMI medium, followed by 18 h incubation in fresh medium.

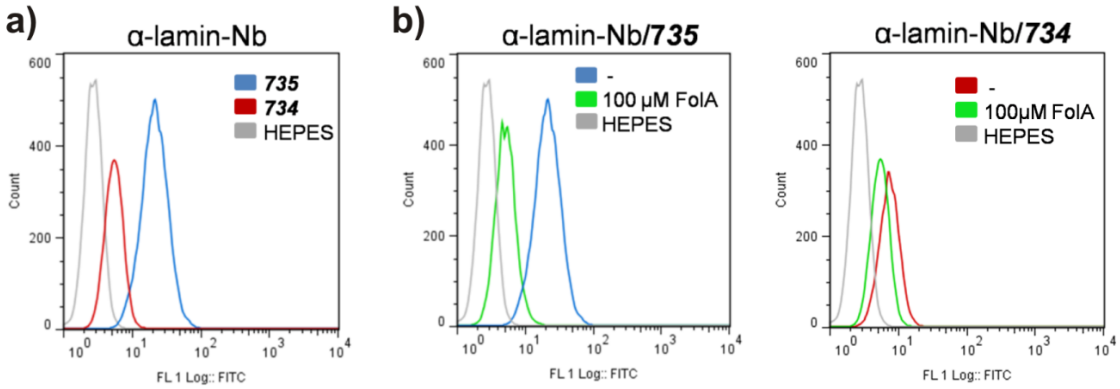

Figure 22: Cellular internalization of carboxyfluorescein (CF) modified α-lamin-Nb. CF-nanobodies were mixed with oligomer ***735*** or ***734*** at a molar ratio of 1:5 and incubated for 4 h at 37 °C. a) KB_*wt* cells were transduced with 3.6 µM nanobody/***735*** (blue) or /***734*** (red). After 1 h incubation at 37 °C cellular internalization was determined by flow cytometry. b) Free folic acid competition experiments: KB_*wt* cells were pre-incubated for 30 min with 100 µM free folic acid. Afterwards cells were transduced with 3.6 µM α-lamin-Nb/***735*** (left) or 3.6 µM α-lamin-Nb/***734*** (right). After 45 min incubation at 37 °C, cellular internalization was determined by flow cytometry. Green, with 100 µM folic acid inhibition; blue or red, without folic acid inhibition; grey, control incubation of cells with HEPES. Adapted from [59].

Microscopic evaluation showed specific binding of Atto647N-labeled nanobody to lamin in 60 % of KB_*wt* cells for the folat receptor-targeted ***735*** formulation, and 40 % for the non-targeted ***734*** formulation (Table 6).

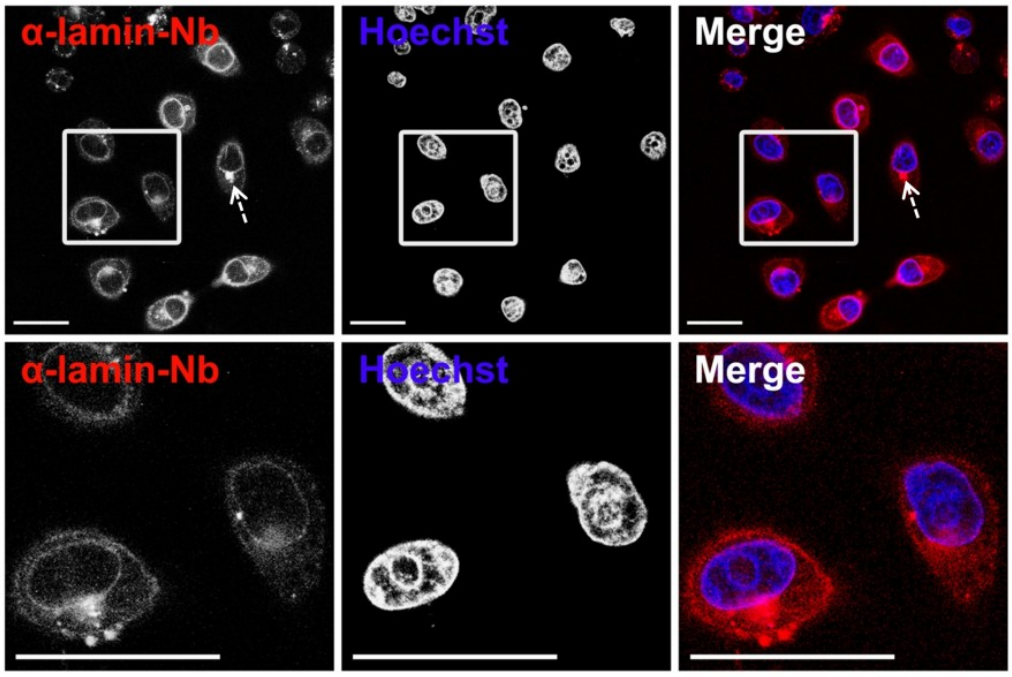

Figure 23: Confocal laser scanning microscopy of live KB_*wt* cells after transduction with α-lamin-Nb/*735*. Cells were incubated with 3.6 µM Atto647N-labeled α-lamin-Nb formulated with ***735*** at a molar ratio of 1:5. KB_*wt* cells were incubated for 1 h with the nanobody/oligomer mixture, followed by 18 h incubation in fresh media. First column, Atto647N fluorescence of labeled α-lamin-Nb which binds to endogenous lamina lining the nucleus visualizing the typical nuclear rim structure; second column, nuclear staining with Hoechst dye; third column, merge of both channels. Dashed arrows exemplary indicating nanoparticles being trapped in cellular vesicles. Scale bars: 25 µm. Adapted from [59].

Cellular internalization experiments resulted in folate receptor specific uptake of CF-labeled α-lamin-Nb/***735*** after 45 min incubation (Figure 22).

Figure 23 depicts the delivery of Atto647N-labeled α-lamin-Nb/***735*** nanoparticles into KB_*wt* cells leading to co-localization of delivered nanobody with endogenous lamina lining the nucleus. The delivery of α-lamin-Nb/***734*** is shown in Figure 24. As for the α-GFP-Nb, some nanobody was still being entrapped in intracellular vesicles showing no co-localization with nuclear lamin (dashed arrow shows exemplary vesicles).

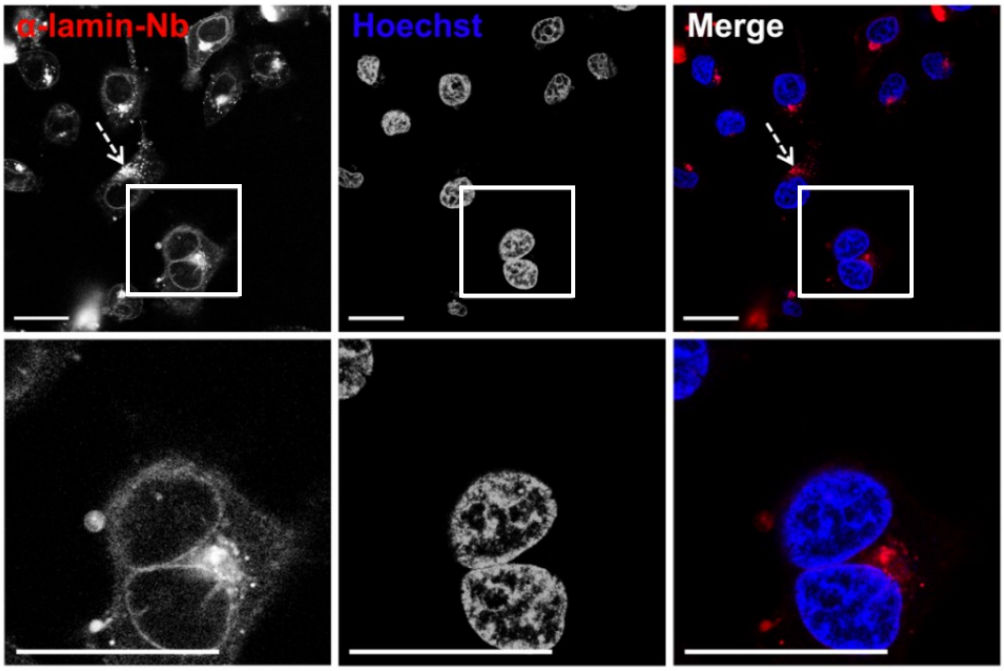

Figure 24: Confocal laser scanning microscopy of live KB_*wt* cells after transduction with α-lamin-Nb/*734*. Cells were incubated with 3.6 µM Atto647N-labeled α-lamin-Nb formulated with oligomer ***734*** at a molar ratio of 1:5. KB_*wt* cells were incubated for 1 h with the nanobody/oligomer mixture, followed by 18 h incubation in fresh media. First column, Atto647N fluorescence of labeled α-lamin-Nb which binds to endogenous lamina lining the nucleus visualizing the typical nuclear rim structure; second column, nuclear staining with Hoechst dye; third column, merge of both channels. Dashed arrows exemplary indicating nanoparticles being trapped in cellular vesicles. Scale bars: 25 µm. Adapted from [59].

3.1.10 Live cell imaging of intracellular delivered lamin nanobody

To further evaluate the uptake and delivery process, real-time imaging of the delivery of Atto647N-labeled α-lamin-Nb/***735*** nanoparticles into KB_*wt* cells was performed. For this purpose, the transduction was carried out as described above. Time series were either taken 1.5 h or 19 h after transduction. Selected frames of these time series are shown in Figure 25. Figure 25 depicts images following the escape of cellular vesicles right after cellular uptake of α-lamin-Nb/***735*** nanoparticles. For this time series pictures were taken every 5 min for 2 h. For cell 1 and 2, the first picture (0 min) shows nanoparticles suggested to be entrapped in cellular vesicles. In the second picture (70 min) the even distribution of α-lamin-Nb through the cell can be seen. Additionally concentrated dots are visible resulting from nanobody suggested to be entrapped in cellular vesicles (dashed arrows show exemplary vesicles). After 120 min highlighting of the nuclear rim structure that is characteristic of the nuclear lamina is visible (red circle), caused by specific binding of the labeled α-lamin-Nb to

nuclear lamin. Concentrated dots (dashed arrows show exemplary vesicles) are a result of nanoparticles suggested to be entrapped in cellular vesicles. In cell 3 no release from cellular vesicles is visible.

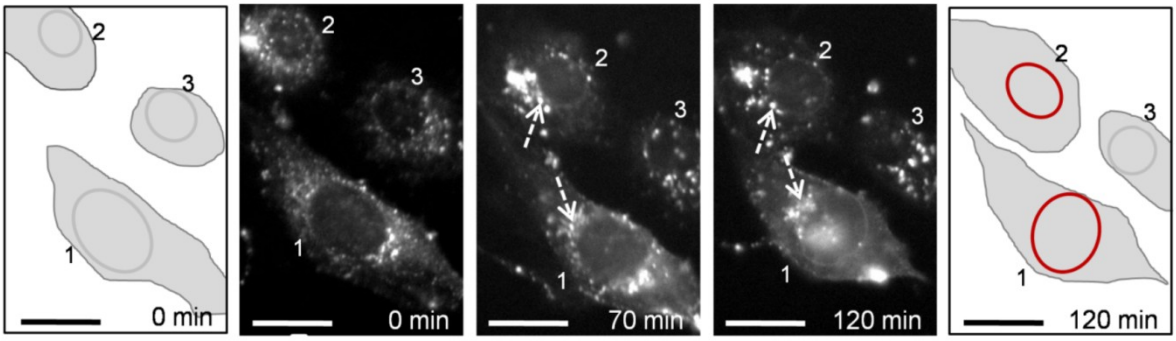

Figure 25: Real-time imaging of the delivery of α-lamin-Nb/*735* into KB_*wt* cells. Cells were incubated with 3.6 µM Atto647N-labeled α-lamin-Nb, formulated with ***735*** at a molar ratio of 1:5 for 1 h, followed by incubation in fresh media. Time series were taken by widefield fluorescence microscopy. Selected frames from these time series are shown. Scale bars: 25 µm. Time series was started 1.5 h after transduction of the cells. Cell 1 and 2, 0 min, nanobody is trapped in cellular vesicles; 70 min, even distribution of nanobody throughout the cell, some nanobody is still being trapped in cellular vesicles (dashed arrows); 120 min, specific co-localization of labeled nanobody with the lamina lining the nucleus can be seen. Concentrated dots (dashed arrows) are resulting from nanoparticles still being trapped in cellular vesicles. Cell 3, nanoparticles are trapped in cellular vesicles for the length of the time series. Schemes depicting cells without specific binding of α-lamin-Nb (0 min) and after specific binding of nanobody to nuclear lamin (120 min) indicated by red coloring of the nuclear membrane in cell 1 and 2. Adapted from [59].

Selected frames from the time series following a cell through cell division, after successful transduction of α–lamin-Nb are shown in Figure 26. Pictures were taken every 5 min for 2 h and afterwards every 15 min for additional 22 h. From the beginning of the imaging (0 min), specific co-localization of α-lamin-Nb and endogenous lamina lining the nucleus could be observed (thick arrow). At that time this cell was probably in G2 phase. Concentrated dots (dashed arrows show exemplary vesicles) are again resulting from nanoparticles being entrapped in cellular vesicles. From 275 min to 350 min the cell could be followed through cell division. Specific binding of α-lamin-Nb to the nuclear lamina could still be found at 515 min and 815 min in the two freshly divided cells.

In sum, functional nanobodies were delivered into live cells leading after escape from cellular vesicles to specific binding of an endogenous target, and the target was visualized throughout the cell cycle.

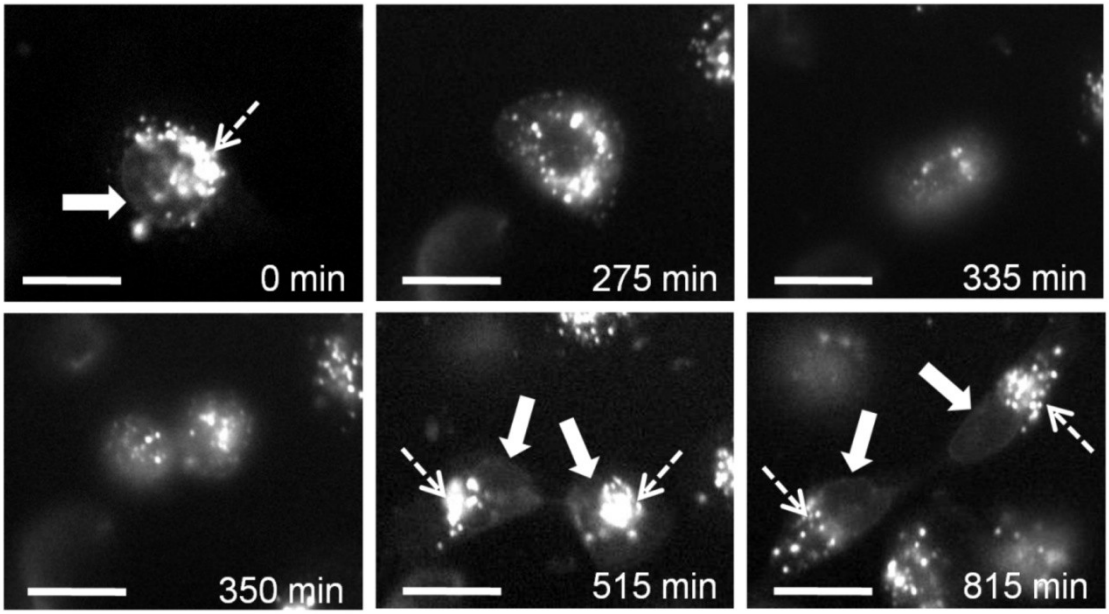

Figure 26: Real-time imaging of binding of α-lamin-Nb to nuclear lamin throughout cell division. Cells were incubated with 3.6 µM Atto647N-labeled α-lamin-Nb, formulated with ***735*** at a molar ratio of 1:5 for 1 h, followed by incubation in fresh media. Time series were taken by widefield fluorescence microscopy. Selected frames from these time series are shown. Scale bars: 25 µm. Imaging was started 19 h after transduction of the cells. At that time this cell was probably in G2 phase (0 min). Specific binding of α-lamin-Nb to the lamina lining the nucleus (thick arrows) can be seen. Concentrated dots (dashed arrows) are resulting from nanoparticles being trapped in cellular vesicles. The cell could be followed through mitosis (275 min - 350 min). Scale bars: 25 µm. Adapted from [59].

3.2 MOF nanoparticles as defined carrier system for His-tagged functional units

Parts of this chapter (3.2.3-3.2.9, 3.2.12) have been adapted from:

Multifunctional nanoparticles by coordinative self-assembly of His-tagged units with metal-organic frameworks. Ruth Röder, Tobias Preiß, Patrick Hirschle, Benjamin Steinborn, Andreas Zimpel, Miriam Höhn, Joachim O. Rädler, Thomas Bein, Ernst Wagner, Stefan Wuttke and Ulrich Lächelt. Journal of the American Chemical Society (2017), 139(6): 2359-2368.

In the following chapter, the investigation of the coordinative interaction of oligohistidine-tags (His-tags) with metal-organic frameworks (MOFs) as a novel external functionalization concept for MOF NPs is presented. This His-tag dependent interaction was developed by Dr. Ulrich Lächelt and Dr. Stefan Wuttke (LMU München). It is based on a self assembly process and the inherent properties of the compounds. An overview of MOFs has been given in the introduction (1.5). MOFs are a class of materials composed of inorganic building units, metal ions or metal oxide clusters, which are coordinatively connected by organic linkers to create porous three-dimensional frameworks Figure 27a.

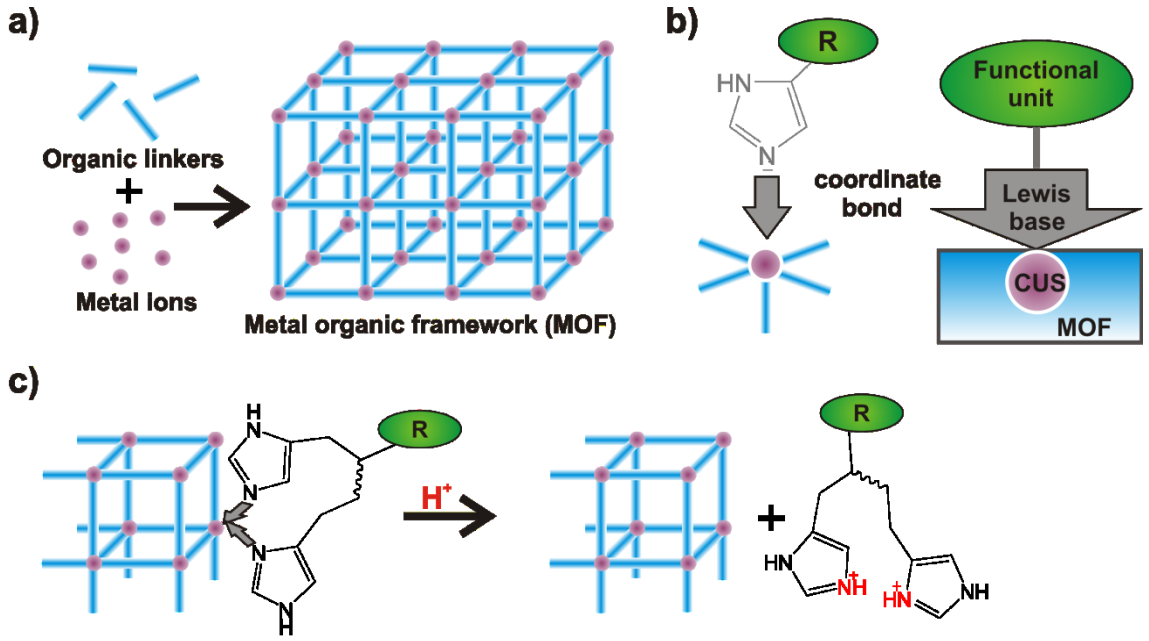

Figure 27: Coordinative self-assembly of His-tagged molecules with MOF NPs. a) Molecular composition of MOFs; b) Coordinative bond between the imidazole group of histidines acting as Lewis base and coordinatively unsaturated metal sites (CUS) acting as Lewis acid. Multifunctional MOF NPs can be generated by coordinative attachment of different functional units via self-assembly; c) Schematic illustration of acidic detachment due to histidine protonation. Adapted from [158].

Their crystallinity, chemically functionalizable pores and potential systematic structural variations are some factors amongst others that allow to precisely design these materials for particular purposes [152, 153]. The described concept uses the interactions between Lewis bases, such as the imidazole function of histidine and coordinatively unsaturated metal sites present on the external surface of MOF NPs to self-assemble different functional units onto MOF NPs (Figure 27b).

Since His-tags can readily be integrated into peptides or proteins by synthetic, recombinant or bioconjugation techniques, they appear to be ideal connectors to create a versatile inorganic/bioorganic interface at the MOF NPs' surface. The same interaction (Figure 27b) is routinely used for the purification of recombinant proteins by immobilized metal ion chromatography [154, 155]. Applicability of the coordinative His-tag interactions for intracellular delivery of proteins has been demonstrated by using conjugates of nitrilotriacetic acid derivatives and cell-penetrating peptides [44, 156], polymers [157] or silica NPs [149]. Since the metalsites are already an integral part of the coordinative MOF structure, the external secondary modification via coordinate bonds in the presented approach of 'self-assembling multifunctional coordination particles' (SAMCOPs) is considered a powerful tool for the combinatorial and stoichiometric generation of functional MOFs.

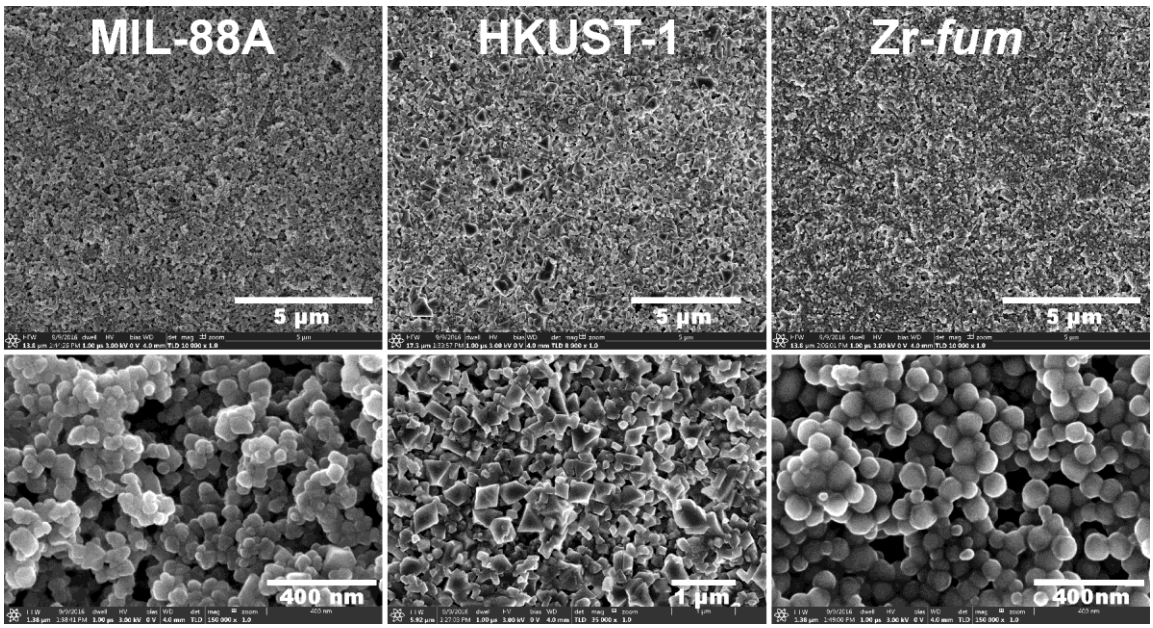

Figure 28: Scanning electron microscopy (SEM) images of MIL-88A (left), HKUST-1 (middle) and Zr-*fum* (right). Lower row depicts enlarged images of the pictures in the upper row. White scale bars upper row: 5 µm; lower row as indicated in the images. SEM images were taken by Dr. Steffen Schmidt and Patrick Hirschle (Department of Chemistry, LMU München). Adapted from [158].

A set of three exemplary MOF structures, MIL-88A (Fe^{3+}/fumaric acid) [121], HKUST-1 (Cu^{2+}/trimesic acid) [140] and Zr-*fum* (Zr^{4+}/fumaric acid) [129]) each based on a different metal component, was selected for testing the assembly strategy (Figure 28).

First, the external binding of various His-tagged synthetic peptides and recombinant or chemically H_6-modified proteins was investigated. The set of functional units used in this study is summarized in Table 7.

Table 7: His-tagged functional units used for the assembly with MOF NPs.

Code	Sequence[a] / Description	Function
A_6, H_6-Acr	Acridine-PEG_{28}-H_6-NH_2	Photometric detection
$H_{0/3/6}$-Acr	Acridine-STOTDA-$H_{0/3/6}$	
H_6-A647N	ATTO647N-PEG_{12}-H_6-NH_2	Fluorescence
H_6-CF	Carboxyfluorescein-PEG_{12}-H_6-NH_2	
H_6-GFP	Recombinant nlsEGFP (H_6-Tag)	Model protein
H_6-Tf*	Transferrin, conjugated with H_6-PEG_{36} and ATTO647N	
H_6-luciferase	Recombinant luciferase (H_6-Tag)	
H_6-Bak	H_6-GGQVGRQLAIIGDDINR-NH_2	Apoptotic peptides
H_6-Bad	H_6-GNLWAAQRYGRELRRMSDEFVD-NH_2	
H_6-KLK	H_6-GGKLAKLAKKLAKLAK-NH_2	
H_6-CytC	CytochromeC conjugated with H_6	Apoptotic protein

[a] Peptide sequences are indicated from N- to C-terminus using the one-letter code for α-amino acids (H_n, n = number of histidines); * ATTO647N label

Dr. Ulrich Lächelt could show the external modification of MIL-88A, HKUST-1 and Zr-*fum* MOF nanoparticles with the His-tag model peptide H_6-Acridine (H_6-Acr), in HEPES buffered glucose (HBG) at pH 7.4 by the detection of residual free peptide in the supernatant after incubation and centrifugation of the MOF suspensions (Figure 29). Figure 29a depicts the chemical structure and control chromatogram of model compounds H_6-Acr and A_6-Acr. For detection of the residual free peptide in the supernatant, H_6-Acr or A_6-Acr control were incubated with different MOF NPs in HBG at pH 7.4 for 15 min. After centrifugation, the supernatant was analyzed by RP-HPLC (λ=360 nm, Figure 29b). The exclusive reduction of H_6-Acr (in contrast to A_6-Acr) in

the supernatant represents qualitative evidence for the histidine dependent interaction with all three investigated MOF species.

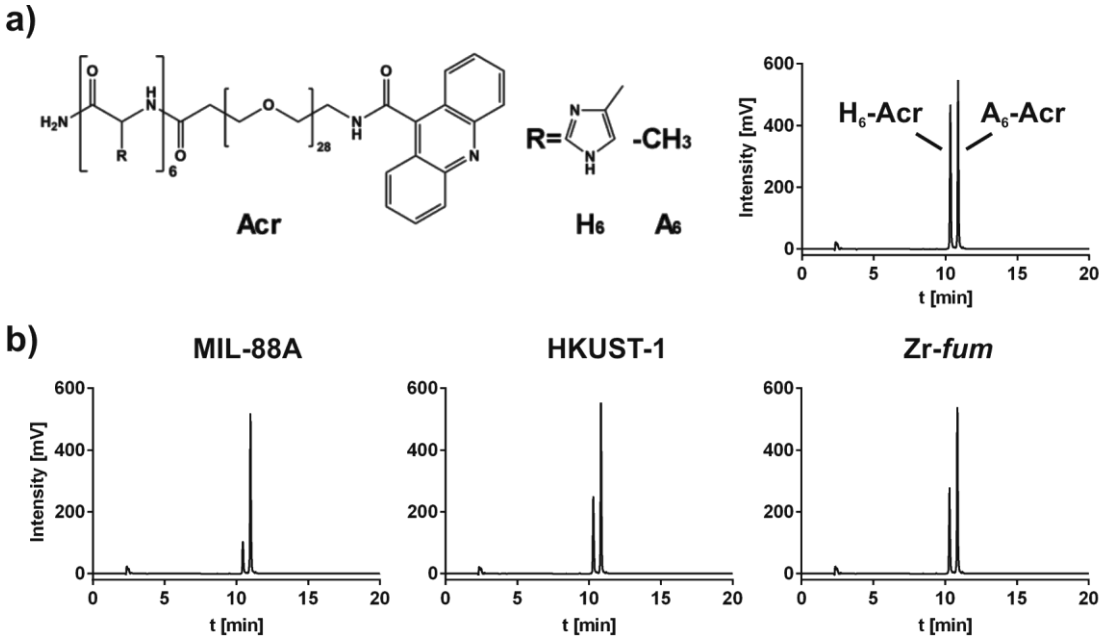

Figure 29: Acridine (Acr) peptide binding to MIL-88A (left), HKUST-1 (middle) and Zr-*fum* (right) particles. a) Chemical structure and control chromatogram of model compounds H_6-Acr and A_6-Acr; b) Different MOF NPs were incubated with H_6-Acr or A_6-Acr in HBG pH 7.4, followed by centrifugation. The residual free peptides in the supernatant were qualitatively determined by RP-HPLC, (H_6 vs. A_6, λ=360 nm). HPLC measurements were carried out by Dr. Ulrich Lächelt (Pharmaceutical Biotechnology, LMU München). Adapted from [158].

Additionally, using fluorescence correlation spectroscopy (FCS) the binding of fluorescently labeled H_6-tags (H_6-A647N) to MOF NPs was measured at low concentrations with single-molecule sensitivity (Figure 30). First H_6-A647N on its own was measured (Figure 30 grey curves), followed by a second measurement after the addition of MOF NPs (Figure 30, colored curves). The FCS measurements were carried out by Dr. Tobias Preiß (Faculty of Physics, LMU München).

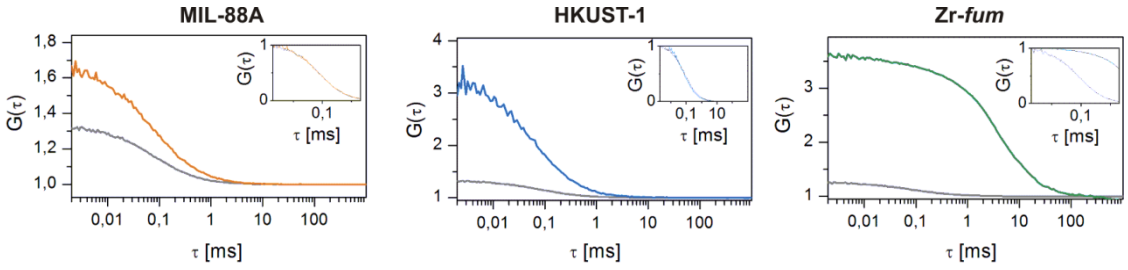

Figure 30: Investigation of interaction of H_6-A647N with different MOF NPs. FCS measurements of H_6-A647N were performed before (grey) and after MOF addition (colored). Inserts show normalization of the same data. FCS measurements were carried out by Dr. Tobias Preiß (Faculty of Physics, LMU München). Adapted from [158].

Figure 30 shows a significant increase in the autocorrelation amplitude after addition of all three MOF species, indicating a reduction of the H_6-tag number concentration most likely due to multiple binding to MOF NPs. In case of MIL-88A and HKUST-1, however, no change in the characteristic correlation decay time could be detected. This can probably be attributed to MOF induced fluorescence quenching [159, 160], as well as rather large effective particle sizes resulting from aggregation, which both can cause a decline of detectable tags after binding.

The following chapter will now show the further characterization of the His-tag MOF interaction with a focus on the potential biological application of this system. Cytotoxicity as well as its potential as carrier for small molecules, proteins and peptides will be evaluated.

MIL-88A, HKUST-1 and Zr-*fum* have been synthesized by Patrick Hirschle (PhD study, Department of Chemistry, LMU München).

H_6-CF, H_6-A647N and H_6-Tf have been synthesized by Dr. Ulrich Lächelt (Group leader, Pharmaceutical Biotechnology, LMU München), $H_{0/3/6}$-Acr were synthesized by Benjamin Steinborn (PhD study, Pharmaceutical Biotechnology, LMU München). The synthesis of all other functional units is described in Material and Methods (Chapter 2).

3.2.1 Heterologous expression and purification of H_6-GFP

H_6-GFP was expressed in *E.coli* BL21(DE3)plysS as has been described in Maier *et al.* [54]. The purified protein was analyzed on SDS-PAGE after staining with Coomassie (Figure 31). H_6-GFP has a size of 26.9 kDa.

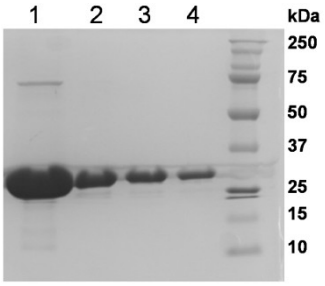

Figure 31: Analysis of purified H_6-GFP. Different amounts of the purified H_6-GFP, were separated on a 10 % SDS-PAGE and stained with Coomassie. 1: 40 µg, 2: 15 µg, 3: 10 µg, 4: 5 µg. Precision Plus Protein standard (BioRad, USA).

From 10 L bacteria culture 30 mg H_6-GFP were obtained.

3.2.2 Cloning, heterologous expression and purification of H_6-luciferase

A well-established system in our lab to quantitatively analyze pDNA- or siRNA transfection is the delivery of either a luciferase containing plasmid, or siRNA to inhibit luciferase expression. Adapting to this system we intended to purify a H_6-tagged luciferase in order to establish a similar read out system for the delivery of proteins. This system would be beneficial in different ways. First it would make screening experiments similar to pDNA or siRNA transfections possible. Furthermore it would not only proof the successful intracellular delivery of a protein but would beyond that verify the functionality of an enzyme after the whole delivery process. The His-tag was first needed for easy protein purification via Ni-affinity chromatography, but could then be used for the coupling to different MOF NPs.
After cloning of luciferase into pET-28a vector (Novagen, Merck Millipore, Germany), to obtain a His-tag containing protein, the accurateness of this cloning experiment was verified by a restriction digest with Hind III and EcoRI (Figure 32a).

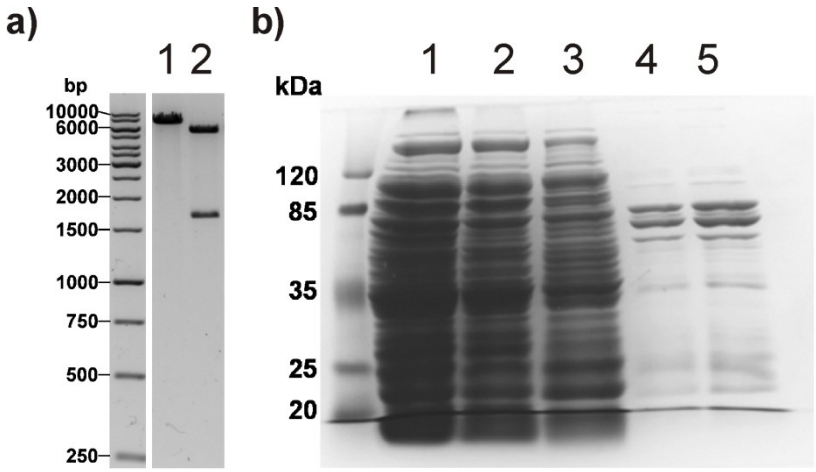

Figure 32: Analysis of cloning of luciferase into pET-28a and purity of resulting expressed and purified H_6-luciferase. a) DNA ladder, 1, linearized plasmid, 2, plasmid digested with HindIII and EcoRI resulting in two fragments at 5369bps and 1758 bps. b) PEQ Lab Protein Marker III (Germany), 1, Bacteria lysate, 2, Flow through of affinity purification, 3, washing step, 4, 10 µg H_6-luciferase, 5, 20 µg H_6-luciferase.

The whole plasmid has a size of 7127 bps. After the restriction digest, two fragments with the size of 1758 bps (H_6-luciferase) and 5369 bps (pET-28a) were obtained, verifying the correct cloning.
This expression plasmid was then transformed into RosettaBL21(DE3)pLysS. Expression was induced by the addition of 500 mM IPTG. The whole purification process was monitored on SDS-PAGE (Figure 32b). From 4 L bacteria culture ~

10 mg H_6-luciferase were obtained. To test the functionality of the purified H_6-luciferase, a luciferase assay was carried out (2.20.3), resulting in ~1 x 10^{12} RLU/mg luciferase.

3.2.3 Cytotoxicity studies of different MOFs

To evaluate the suitability of MOF NPs as intracellular carrier system, the toxicity of MIL-88A (Fe^{3+}/fumaric acid) [121], HKUST-1 (Cu^{2+}/trimesic acid) [140] as well as Zr-*fum* (Zr^{4+}/fumaric acid) [129] was investigated on HeLa_*wt* cells. Cells were incubated with different MOF NP concentrations for 48 h followed by evaluation of cell viability by MTT assay (Figure 33a).

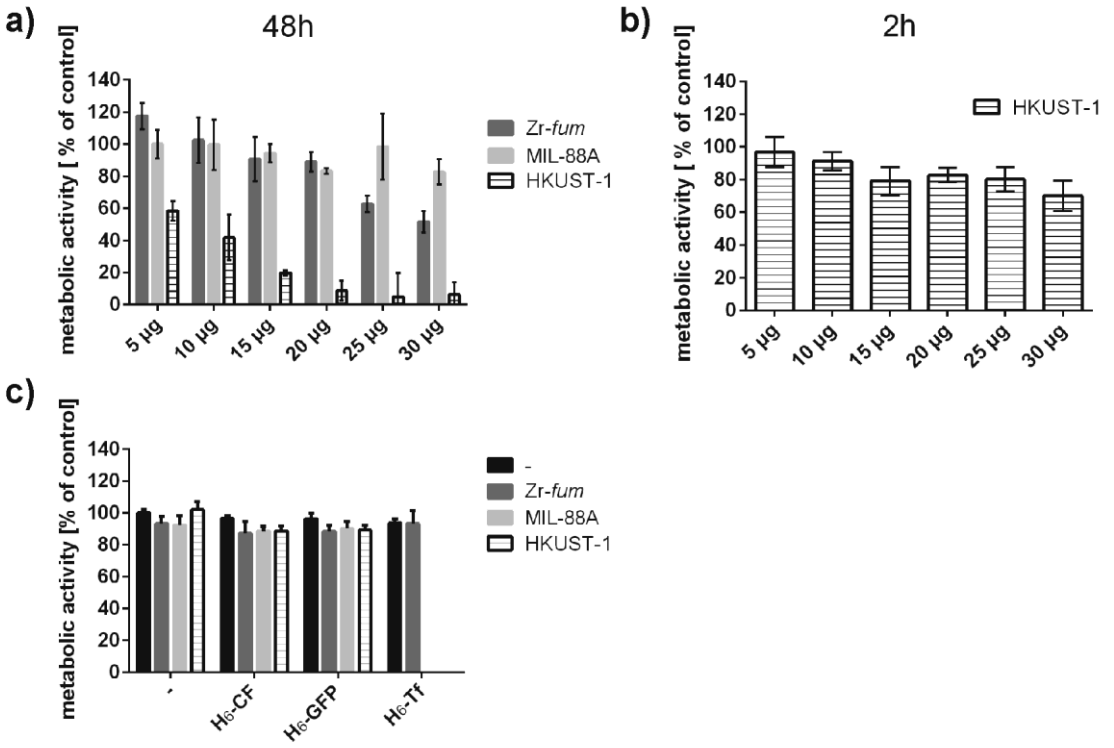

Figure 33: Evaluation of cytotoxicity of different MOF nanoparticles. HeLa_*wt* cells were incubated with different amounts of Zr-*fum* (dark grey), MIL-88A (light grey) and HKUST-1 (pattern) for 48 h (a) or 2 h (b). c) Incubation of HeLa_*wt* cells with 10 µg MOFs modified with different His-tags or without His-tags (-). CF: carboxyfluorescein, Tf: transferrin. Data are presented as % metabolic activity of control cells ± SD (*n*=5) (MTT assay). Adapted from [158].

MIL-88A and Zr-*fum* were very well tolerated, HKUST-1 exhibited considerable cytotoxicity. Therefore incubation times were reduced to 2 h, deleting observable effects on metabolic activity after 48 h (Figure 33b). Additionally also the effect on

metabolic activity of the different His-tags was evaluated, showing no effect (Figure 33c).

3.2.4 Investigation of His-tag binding to different MOF NPs

Apart from, the in the introduction to this chapter described investigation of binding using RP-HPLC, the His-tag specific binding of H_6-Acr compared to A_6-Acr was verified by zeta potential measurements (Figure 34). Therefore MOF NPs were incubated with H_6-Acr or A_6-Acr as a control. The change in Zeta potential with and without the addition of MOF NPs was investigated. A significant shift towards neutrality caused by the His-tag containing derivatives only could be detected for all three different MOF NPs.

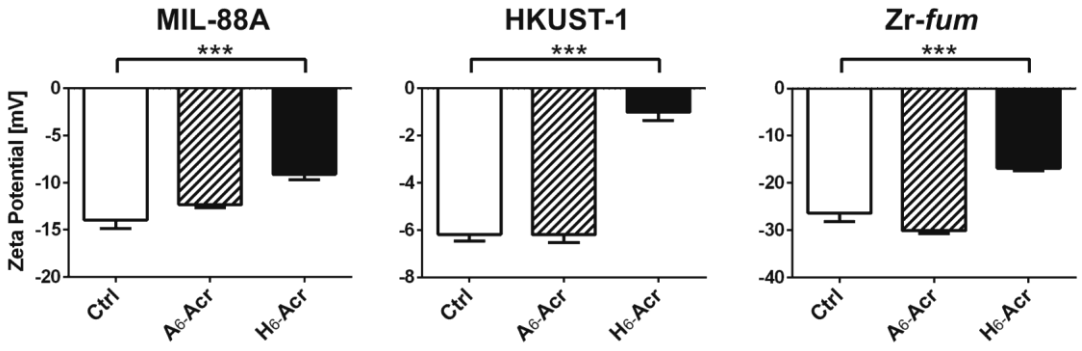

Figure 34: Effect of peptide binding to MOF NP on their zeta potential. After incubation of MOF NPs with A_6-Acr (patterned bar), H_6-Acr (black bar) or without His-tag (white bar) the change in zeta potential was measured by dynamic light scattering. Zeta potentials were calculated by the Smoluchowski equation, each sample was measured 3 times with 10 to 30 subruns at 25 °C. Adapted from [158].

3.2.5 Investigation of stability of His-tag Zr-*fum* interaction

For first evaluations of the suitability of the functionalized MOF NPs for their use in cell culture, the stability of the Zr-*fum* H_6-A647N interaction under different conditions was investigated by FCS (Figure 35). Free H_6-tags (blue) showed fast single molecule diffusion prior to NP addition (Figure 35, left). After the addition of Zr-*fum* NPs at pH 7.4 (orange) the collective diffusion was shifted towards higher diffusion times revealing H_6-tag binding to Zr-*fum* NPs. Following acidification (green) the diffusion rate increased relative to the pH 7.4 measurement indicating partial

detachment of tags from the MOF NP surface, due to the protonation of histidines. Also the interaction in DMEM medium containing 10 % FBS was investigated (Figure 35, right). Importantly, H_6-tag association with Zr-*fum* NPs remained stable, confirming the suitability for use under cell culture conditions. These FCS measurements were carried out by Dr. Tobias Preiß (Faculty of Physics, LMU München).

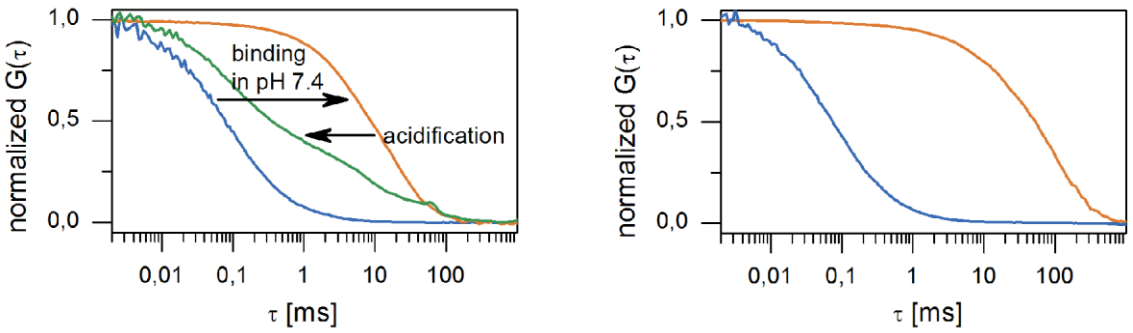

Figure 35: Investigation of Zr-*fum*/H_6-A647N interaction under different conditions. Left: The addition of Zr-*fum* NPs to free H_6-A647N (blue), lead to a shift of the collective diffusion time towards higher diffusion times (orange). Upon acidification, the diffusion rate increased (green). Right: Measurements in DMEM (10 % FBS) of free H_6-A647N (blue) and Zr-*fum*/H_6-A647N (orange). FCS measurements were carried out by Dr. Tobias Preiß (Faculty of Physics, LMU München). Adapted from [158].

Additionally, a time course experiment was carried out to investigate the pH dependent stability of Zr-*fum*/H_6-A647N over a longer period of time (Figure 36). After functionalization of Zr-*fum* NPs with H_6-A647N for 15 min, MOF NP suspensions were set to a defined pH and incubated for 0.5 h, 3 h or 24 h. After centrifugation, data was obtained by photometric determination (λ=646 nm) of free H_6-A647N in the supernatant. The experiment was carried out by Benjamin Steinborn (PhD study, Pharmaceutical Biotechnology, LMU München). Figure 36 shows stable association of Zr-*fum*/H_6-A647N for 24 h at pH 7.4 and rapid partial (pH 5) or complete (pH 3) release upon acidification. This is consistent with the hypothesis of unprotonated histidines acting as Lewis base and being responsible for binding (Figure 27). It is suggested that the incomplete detachment at pH 5 is caused by a lowered pK_a of the imidazole group due to metal ion binding [161] and an equilibrium between protons and metal ions competing for histidine interactions.

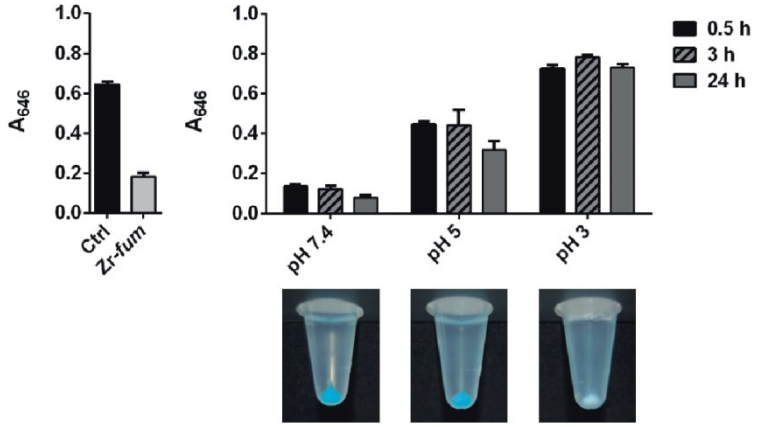

Figure 36: pH dependent stability of H_6-tag binding to Zr-*fum* NPs. Experimental data obtained by photometric determination (λ=646 nm) of free H_6-A647N in the supernatant after centrifugation; Zr-*fum* NPs were loaded with H_6-A647N at pH 7.4 for 15 min (left). MOF NP suspensions were then acidified to a defined pH and incubated for indicated times (right). Reaction tubes below show the samples after 24 h at pH 7.4 (left), pH 5 (middle), pH 3 (right) and centrifugation; decoloration of MOF pellets due to acidic H_6-A647N detachment at pH 3 can be observed. The experiment was carried out by Benjamin Steinborn (PhD study, Pharmaceutical Biotechnology, LMU München). Adapted from [158].

3.2.6 Evaluation of simultaneous binding of two entities to a single particle

As a distinct advantage of the self-assembly concept demonstrated here is the possible one-step multifunctionalization of MOF NPs by simultaneously mixing different H_6-tagged functional units with bare MOF NPs. This fact was first evaluated by fluorescence cross-correlation spectroscopy (FCCS) measurements. Two His-tagged proteins with distinct fluorescence spectra - recombinant GFP with genetically encoded His-tag: H_6-GFP, and human transferrin chemically conjugated with a H_6-tag and Atto647N label: H_6-Tf* - were used to investigate simultaneous binding of both entities to single MOF NPs (Figure 37). To a solution containing equimolar amounts of both proteins, Zr-*fum* NPs were added and the shift in the autocorrelation curve was investigated. Figure 37 shows the autocorrelation and cross-correlation curves of mixed H_6-GFP and H_6-Tf* solutions before and after the addition of Zr-*fum* NPs. We found no coincidence of H_6-GFP and H_6-Tf* without NPs since the cross-correlation curve of protein mixture is close to baseline (Figure 37 light grey dotted, not exactly baseline due to crosstalk of GFP into red channel). After addition of Zr-*fum* NPs the analysis of the cross-correlation (Figure 37 dark grey) shows a high ratio of co-localization of both proteins which is interpreted as simultaneous attachment of H_6-GFP and H_6-Tf* to the same NPs surface.

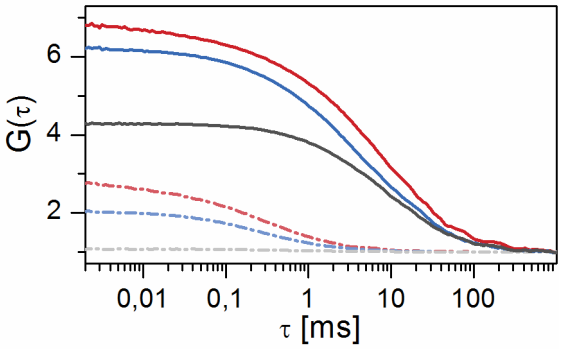

Figure 37: Fluorescence cross-correlation spectroscopy (FCCS) measurements of H_6-GFP and H_6-Tf*. FCCS measurements of H_6-GFP (blue) and H_6-Tf* (red) in HBG (pH 7.4) were carried out before (dotted), and after (solid) the addition of Zr-*fum* MOF NP. Cross-correlation before (dotted grey) and after (solid grey) Zr-*fum* addition. FCCS measurements were performed by Dr. Tobias Preiß (Faculty of Physics, LMU München). Adapted from [158].

3.2.7 Evaluation of cellular uptake using flow cytometry and confocal laser scanning microscopy

After demonstrating that MOF NPs can effectively be functionalized with His-tags, and that MOF NPs do not exhibit significant cytotoxicity under the used conditions, cellular uptake of MOF NPs was investigated. All three different MOF species were functionalized with H_6-tagged fluorescent dye (H_6-carboxyfluorescein, H_6-CF) or H_6-GFP and incubated on HeLa_*wt* cells for 24 h. In case of HKUST-1 NPs, due to their cytotoxicity (Figure 33) incubation was reduced to 2 h. Cellular uptake was investigated by flow cytometry and confocal laser scanning microscopy (CLSM, Figure 38 and 39). MIL-88A and HKUST-1 MOF NPs contained huge particles with a tendency to aggregate and showed quenching effects, as has been described above, resulting in poor detectability of cellular uptake (Figure 38a, b). Incubation of cells with pure His-tags without the addition of MOF NPs did not show any cellular uptake (Figure 38c). Zr-*fum*/H_6-CF or Zr-*fum*/H_6-GFP showed cellular uptake in flow cytometry analysis (Figure 39a) and CLSM images (Figure 39b). The mean fluorescence intensity (MFI, inset) of cells treated with Zr-*fum*/H_6-CF increased 20-fold compared to free H_6-CF. The MFI of cells treated with Zr-*fum*/H_6-GFP even showed 30-fold higher values compared to free H_6-GFP.

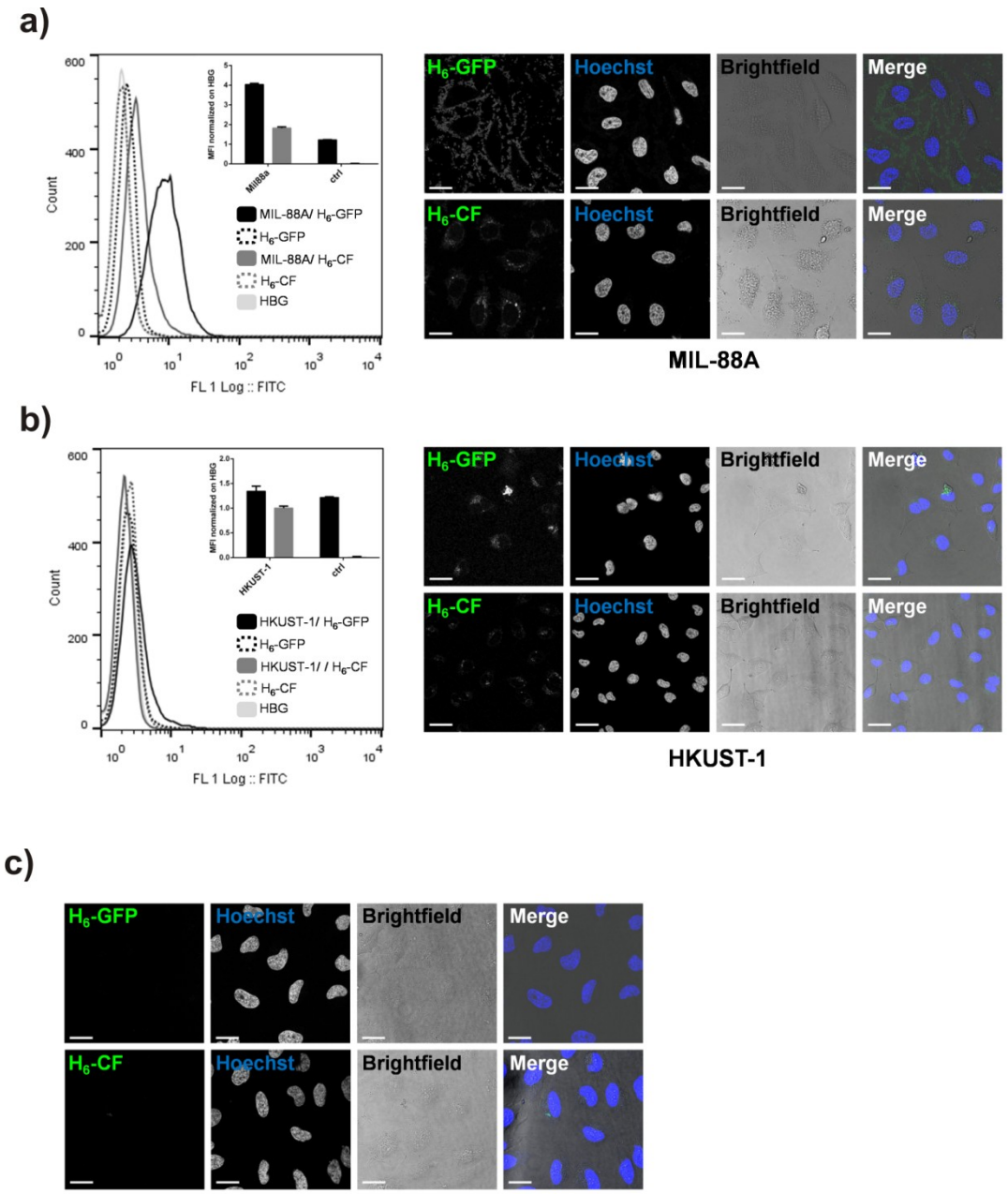

Figure 38: Cellular uptake of H_6-GFP or H_6-CF functionalized MIL-88A or HKUST-1 MOF NPs. H_6-GFP or H_6-CF were incubated with MOF NPs for 15 min at room temperature. Mixtures were put on HeLa_*wt* cells at a concentration of 0.1 mg MOF NP/nmol His-tag per mL medium. MIL-88A MOF NPs were incubated on the cells for 24 h. HKUST-1 MOF NPs for 2 h. Flow cytometric analysis: MOF NP/H_6-GFP (black), H_6-GFP (dotted black), MOF NP/H_6-CF (dark grey), H_6-CF (dotted dark grey), HBG (light grey). Inset shows mean fluorescence intensity (MFI) normalized on HBG. Ctrl indicating incubations without the addition of MOF NPs. Confocal laser scanning microscopy (CLSM) images from left to right: green fluorescence of H_6-GFP or H_6-CF, nuclear staining with Hoechst dye, brightfield picture, merge of all three channels. Scale bars: 25 µm.
a) Evaluation of cellular uptake using MIL-88A MOF NPs. Scale bars: 25 µm. b) Evaluation using HKUST-1 MOF NPs. Scale bars: 50 µm. c) Control incubations without the addition of MOF NPs H_6-GFP (upper row), H_6-CF (lower row). Scale bars: 25 µm.
Please note, that both MIL-88A and HKUST-1 MOF NPs have high quenching abilities, and especially the flow cytometric analysis might not be sensitive enough to detect the actual amount of internalized H_6-GFP, H_6-CF. The same might also be the case for CLSM. Adapted from [158].

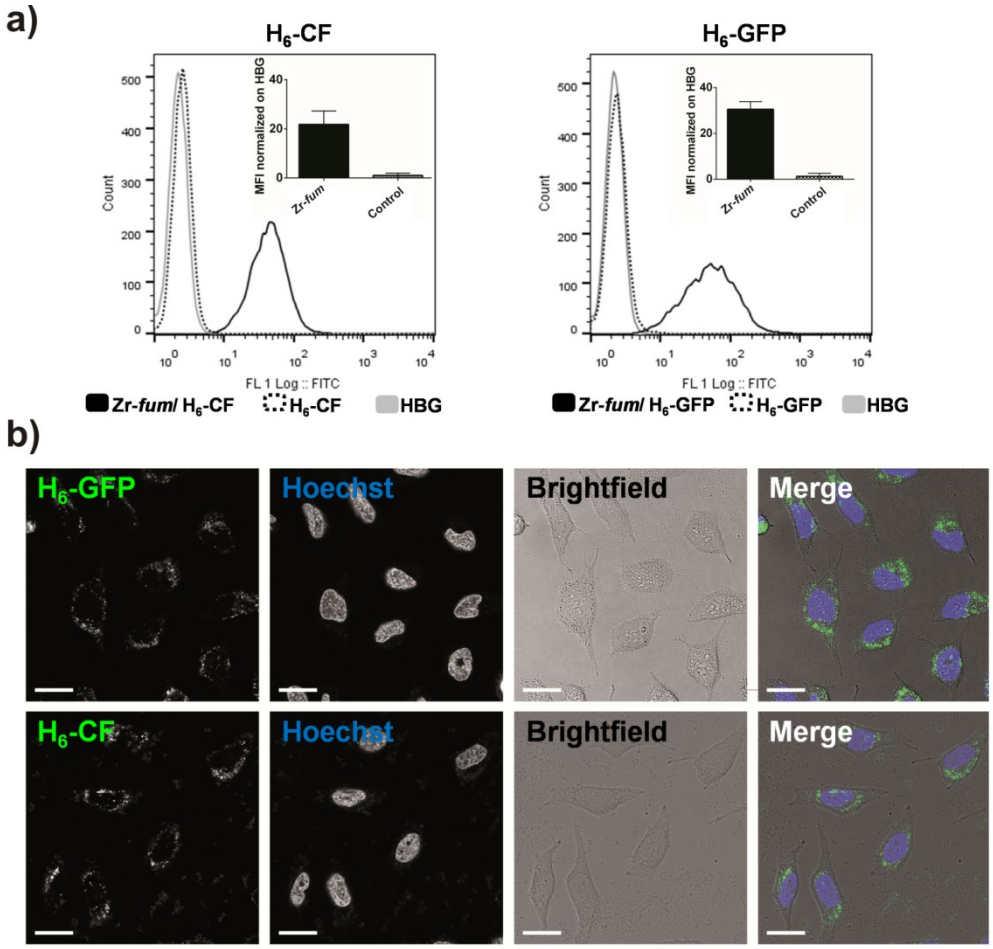

Figure 39: Cellular uptake of H_6-GFP or H_6-CF functionalized Zr-*fum* NPs. H_6-GFP or H_6-CF were incubated with MOF NPs for 15 min at room temperature. Mixtures were put on HeLa_*wt* cells at a concentration of 0.1 mg MOF NP/nmol His-tag per mL medium and incubated for 24 h. a) Flow cytometric analysis: Zr-*fum*/H_6-CF or H_6-GFP (black), pure H_6-CF or H_6-GFP (dotted black), HBG (light grey). Inset shows mean fluorescence intensity (MFI) normalized on HBG. Ctrl indicating incubations without the addition of MOF NPs. b) Confocal laser scanning microscopy (CLSM) images from left to right: green fluorescence of H_6-GFP or H_6-CF, nuclear staining with Hoechst dye, brightfield picture, merge of all three channels. Scale bars: 25 µm. Adapted from [158].

3.2.8 Cellular uptake of double-functionalized Zr-*fum* nanoparticles

The possible one-step multifunctionalization of MOF NPs by simultaneously mixing different His-tagged units with bare MOF NPs facilitates the creation of multifunctional MOF NPs with various stoichiometric ratios as required for optimization of spatio-temporal co-delivery into cells. As the simultaneous assembly of H_6-GFP and H_6-Tf* with Zr-*fum* MOF NPs had been confirmed by FCCS measurements (Figure 37), HeLa_*wt* cells were subjected to these double-functionalized particles (Zr-*fum*/H_6-GFP+H_6-Tf*) for 24 h, and the internalization was investigated (Figure 40). Considerable co-localization of H_6-GFP and H_6-Tf* could be

observed (Figure 40a and b, upper row), as indicated by the yellow coloring in the merge images. In contrast to free H_6-GFP, free H_6-Tf* was also taken up by the cells without the addition of Zr-*fum* MOF NPs to a certain extent (Figure 40 a and b, lower row). This can be explained by the fact that HeLa cells express the transferrin receptor (Figure 41), thus enabling receptor mediated uptake of free H_6-Tf*.

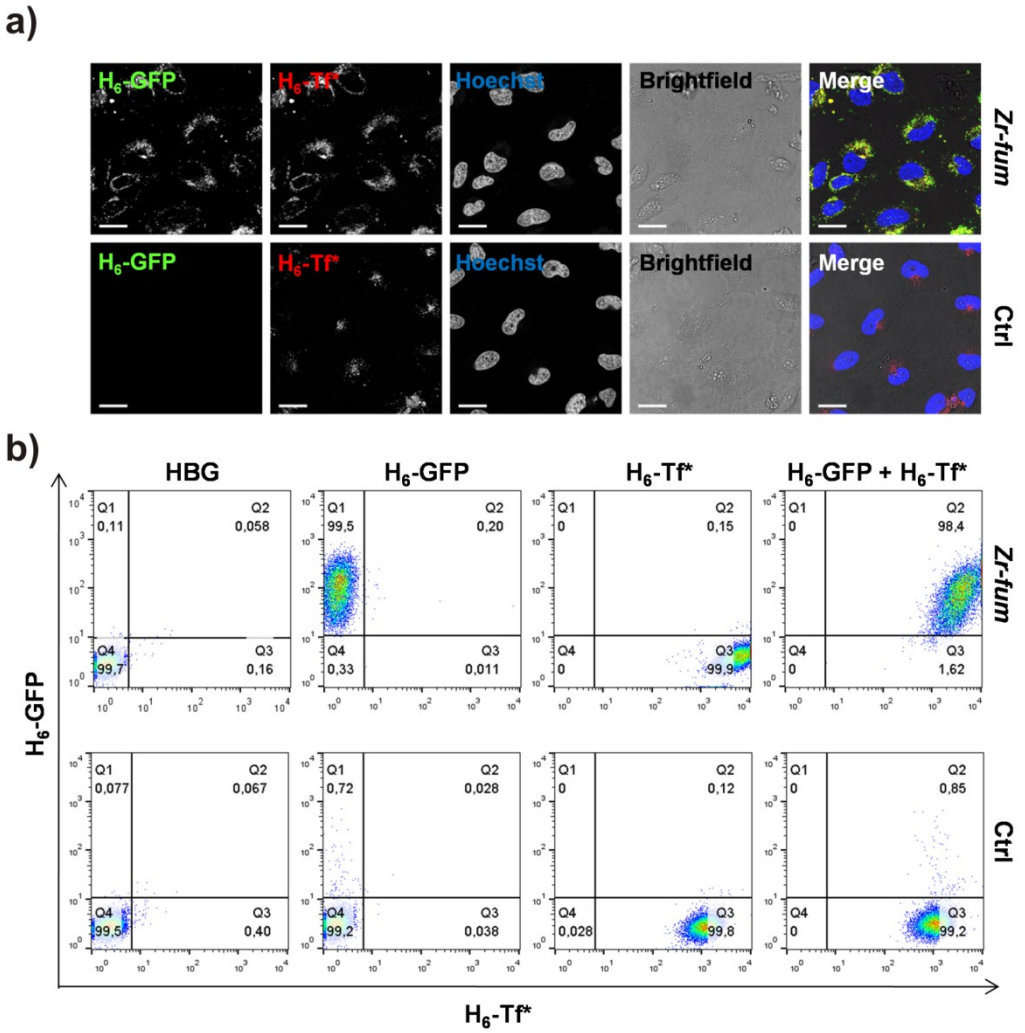

Figure 40: Co-delivery of H_6-GFP and H_6-Tf* into HeLa_*wt* cells. His-tags were incubated with Zr-*fum* MOF NPs for 15 min at room temperature. Different mixtures were incubated for 24 h on HeLa_*wt* cells at a concentration of 0.1 mg Zr-*fum* MOF NP and 1 nmol His-tags per mL medium, followed by CLSM imaging or flow cytometric analysis. Cellular uptake of Zr-*fum*/H_6-GFP+H_6-Tf* (upper row) or control without MOF NPs (lower row). a) CLSM images. left to right: fluorescence of H_6-GFP, fluorescence of H_6-Tf*, nuclear staining with Hoechst dye, brightfield picture, merge of all four channels, yellow color indicates co-localization of H_6-GFP and H_6-Tf*. Scale bars: 25 µm. b) Flow cytometry analysis: Evaluation of delivery of Zr-*fum*/H_6-GFP +H_6-Tf* (upper row) or control without the addition of Zr-*fum* MOF NPs (lower row). Left to right: HBG control, H_6-GFP, H_6-Tf*, H_6-GFP + H_6-Tf*. Adapted from [158].

However, despite the MOF independent uptake route of H_6-Tf*, association with Zr-*fum* resulted in 5-fold higher internalization, confirming an additional boost due to NP mediated uptake.

In summary, the evidence for simultaneous assembly of different functional units with Zr-*fum* MOF NPs as well as concurrent transport into living cells indicates the successful creation of multifunctional programmable MOF NP interfaces capable of manipulating cellular processes.

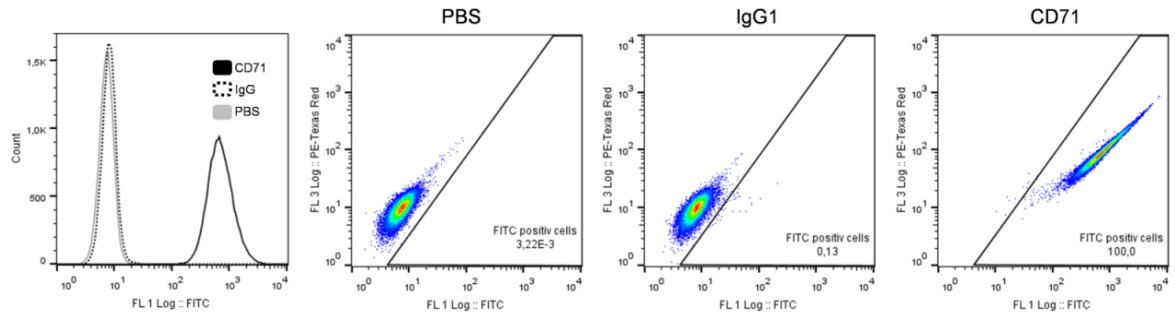

Figure 41: Determination of surface expression level of transferrin receptor (TfR) in HeLa_*wt* cells by flow cytometry. Control cells (dotted black) were treated with mouse IgG1. Mouse anti-hCD71 antibody was used for the detection of the TfR (solid black). Alexa Fluor 488 Goat Anti -Mouse IgG(H+L) secondary antibody was used for the detection of receptor expression. Grey, PBS. Adapted from [158].

3.2.9 Investigation of the endocytosis mechanism of MOF NPs

The cellular uptake pathway of MOF NPs was investigated using Zr-*fum*/H_6-GFP nanoparticles as a model system. First investigations where cells were pre-incubated for 30 min at 4 °C to reduce cellular metabolism and block energy dependent processes, before incubation with Zr-*fum*/H_6-GFP for 2 h on ice, revealed a mainly energy dependent uptake pathway. To further analyze the endocytotic pathway, cellular uptake experiments were carried out in the presence of different endocytosis inhibitors. Chlorpromazine inhibiting clathrine mediated endocytosis, amiloride inhibiting macropinocytosis and genistein inhibiting caveloae mediated endocytosis were used to discriminate the particular endocytotic routes.

Cells were always pre-incubated with the different inhibitors for 30 min followed by incubation with Zr-*fum*/H_6-GFP NPs for 2 h. Afterwards the cellular fluorescence was assayed by flow cytometry. Amiloride showed the greatest inhibition suggesting macropinocytosis is having major contribution to the uptake of Zr-*fum*/H_6-GFP nanoparticles. Since some effect of genestein was observed, caveloae mediated uptake might also be involved.

Looking at the intracellular distribution of internalized H_6-GFP, or H_6-CF via Zr-*fum* MOF NPs in detail (Figure 39), the spotty arrangement indicates high vesicular

entrapment and suggests endosomal escape to be a hurdle for cytosolic delivery.

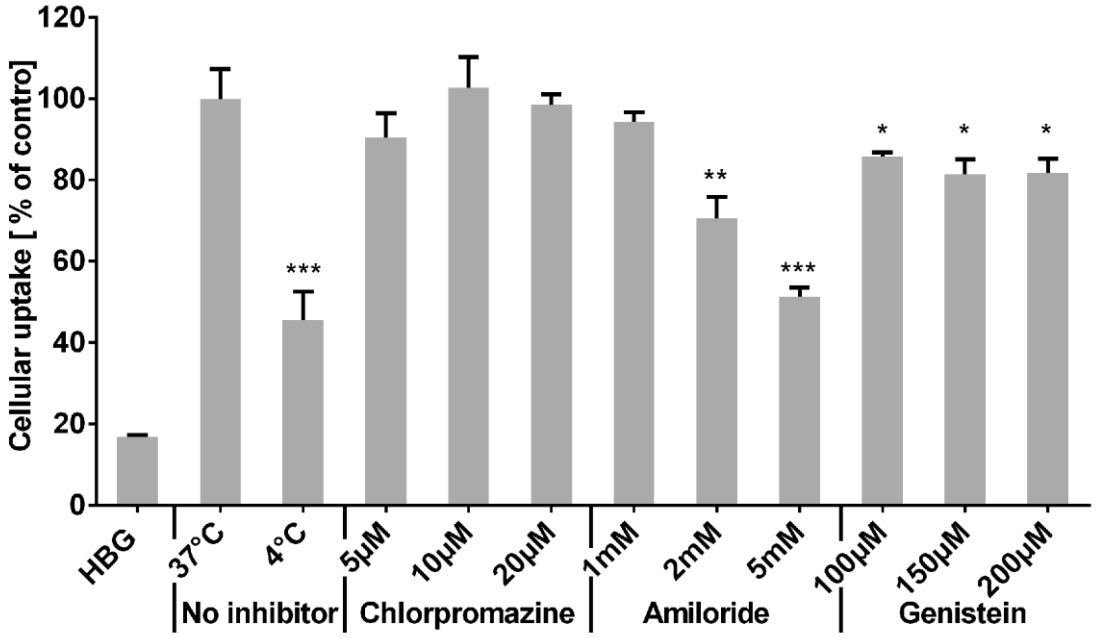

Figure 42: Evaluation of endocytosis inhibition of Zr-*fum*/H_6-GFP nanoparticles. H_6-GFP was incubated with Zr-*fum* NPs for 15 min at room temperature. HeLa_*wt* cells were pre-incubated with the different inhibitors or at 4 °C for 30 min. Afterwards Zr-*fum*/H_6-GFP NPs were added followed by incubation for 2 h at 37 °C or 4 °C. Flow cytometric analysis was carried out in PBS (pH 4.0) to quench the extracellular fluorescence. Cellular uptake was evaluated by calculation of the mean fluorescence intensity (MFI). Data is presented as % cellular uptake, of cellular uptake of Zr-*fum*/H_6-GFP NPs at 37 °C. ± SD (*n*=3). Adapted from [158].

3.2.10 Screening of different functionalizing units to enhance cellular uptake or endosomal escape

3.2.10.1 Evaluation of different lipids to enhance cellular uptake and endosomal escape

Liposomes were one of the first nanosized drug delivery systems ever to be produced [162]. Compared to other nanoparticles, liposomes usually have a reduced cytotoxicity and liposomal encapsulation can help to reduce clearance by the immune system, thus increasing circulation time of various drugs in the system.

In the upcoming chapter we have applied the two phospholipids 1,2-dioleoyl-*sn*-glycero-3-phosphocholine (DOPC) and 1,2-dioleoyl-*sn*-glycero-3-phospho-ethanolamine (DOPE) to enhance cellular uptake and endosomal escape of the MOF NPs.

Phospholipids are phosphorus containing, amphiphilic lipids, with a hydrophilic head and two hydrophobic fatty acid “tails”. Building the bilayer of bio membranes, they are a major component of all cell membranes. Phospholipids in general have a very wide range of application in drug delivery systems, examples are: Doxorubicin (Lipo-Dox®, Doxil®) [163], Cytosine (DepoCyt®) or Morphine sulfate (DepoDur™) [164, 165].

Both in plants and animals, phosphatidylcholine (PC) and phosphatidylethanolamine (PE) are the most common phospholipids [166]. Contrary to that, membranes of liposomes consist usually to a better part of PC. Due to the low hydration of its polar head group, PE has the ability to form non-bilayer structures under physiological conditions, destabilizes membranes, and induces membrane fusion [167].

DOPE is usually used to prepare pH sensitive liposomes, but it has difficulties to form liposomes on its own. Therefore usually materials containing titratable acidic groups must be added. At neutral pH the fatty acid carboxyl group can provide effective electrostatitc repulsion, while at acidic pH, the carboxyl groups are protonated, inverting from a bilayer- to a non-bilayer phase (also called hexagonal II phase) [165, 168].

Wuttke *et al.* [86] have shown the successful coating of MIL-100(Fe) and MIL-101(Cr) with DOPC, by a controlled solvent-exchange deposition of the lipid onto the MOF surface. These MOF@lipids systems were able to effectively store dye molecules leading to cellular uptake into cells.

The results of the encapsulation of functionalized MOFs into micelles but also the effect of just adding lipids to the functionalized MOF solutions without any prolonged micelle formulation reactions are presented in the following section.

Functionalized Zr-*fum* NPs (Zr-*fum*/H_6-CF or Zr-*fum*/H_6-GFP) were either coated with DOPC (micelle formation) or DOPC was just added to the solution. Afterwards, cellular uptake of MOF NPs into HeLa_*wt* cells was analyzed by flow cytometry (Figure 43). In general, the addition of DOPC lead to enhanced cellular uptake of His-tag functionalized Zr-*fum* NPs. Without the addition of MOF NPs no cellular uptake of free His-tags could be detected (Figure 43; MFI: grey or patterned bars, histograms: patterned curves). Cellular uptake of Zr-*fum*/H_6-CF encapsulated in DOPC micelles (Figure 43 left) did not seem to be as high as cellular uptake just after the addition of DOPC (Figure 43 right). Comparison of cellular uptake of bare Zr-*fum*/H_6-CF shows a decreased uptake of the samples used for micelle formation. Due to the micelle formation protocol, the functionalization of Zr-*fum* NPs was carried out in a ten times

higher volume than the functionalization of samples where the DOPC solution was just added. Hence in case of H_6-CF, the concentration of His-tag and MOF seems to have a significant impact on effective functionalization of MOF NPs. Disregarding this volume dependent effect, cellular uptake of Zr-*fum*/H_6-CF NPs could significantly be enhanced by just adding increasing volumes of DOPC until a final concentration in the well of 21.6 µM.

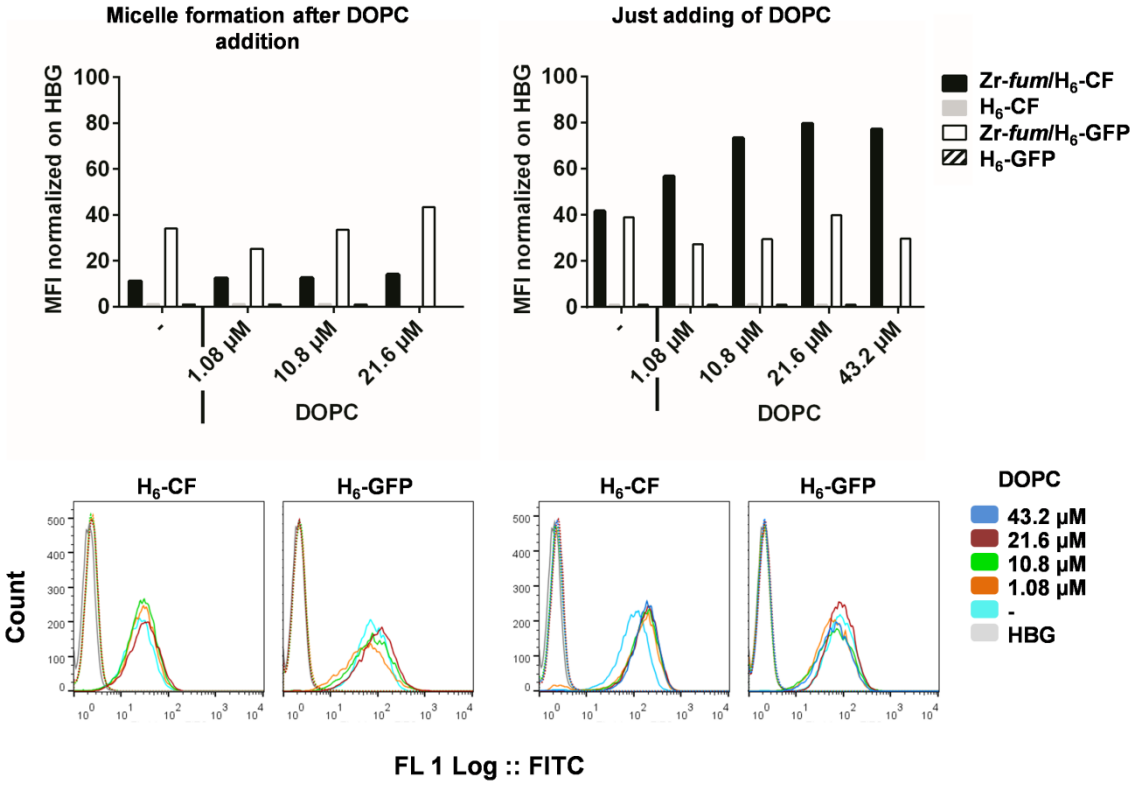

Figure 43: Flow cytometry analysis of the influence of the addition of DOPC to functionalized Zr-*fum* NPs. After functionalization of Zr-*fum* NPs with H_6-CF or H_6-GFP (30 µg Zr-*fum*/0.22 nmol H_6-CF or H_6-GFP per well), DOPC was added to the solution. NPs were either encapsulated in DOPC micelles, according to protocol [86] (left), or DOPC was just added to the solution (right). Samples were incubated on KB_*wt* cells for 24 h. Calculated mean fluorescence intensities (MFI) values were normalized on HBG. Experiments were always carried out with or without the addition of Zr-*fum* NPs. MFI histograms: Zr-*fum*/H_6-CF (black), H_6-CF (grey), Zr-*fum*/H_6-GFP (white), H_6-GFP (patterned). Flow cytometry: Zr-*fum*/His tag (solid curves), His-tag (patterned curves). Final DOPC concentration in the well; 43.2 µM (blue), 21.6 µM (red), 10.8 µM (green), 1.08 µM (orange), - : without the addition of DOPC (turquoise), HBG control (grey). Samples were prepared in duplicates.

Higher concentrations did not further enhance cellular uptake. Coating of Zr-*fum*/H_6-CF with DOPC did show a negligible effect. Compared to H_6-CF, the volume in which MOF NPs were functionalized with H_6-GFP had much lower impact on cellular uptake. Including DOPC in the reaction just had a slight, but-dose dependent effect on Zr-*fum*/H_6-GFP NPs, which did not differ significantly between the samples in

which Zr-*fum*/H_6-GFP NPs were encapsulated in DOPC micelles or the ones where DOPC was just added. Here concentrations higher than 21.6 µM even seemed to worsen cellular uptake.

To further investigate the influence of DOPC on intracellular distribution of internalized functionalized Zr-*fum* NPs, CLSM was performed. Figure 44 shows images of H_6-CF (upper two rows) or H_6-GFP (lower two rows) functionalized Zr-*fum* NPs, to which 10.8 nmol DOPC (first and third row) were optionally added, before incubating them on KB_*wt* cells for 24 h.

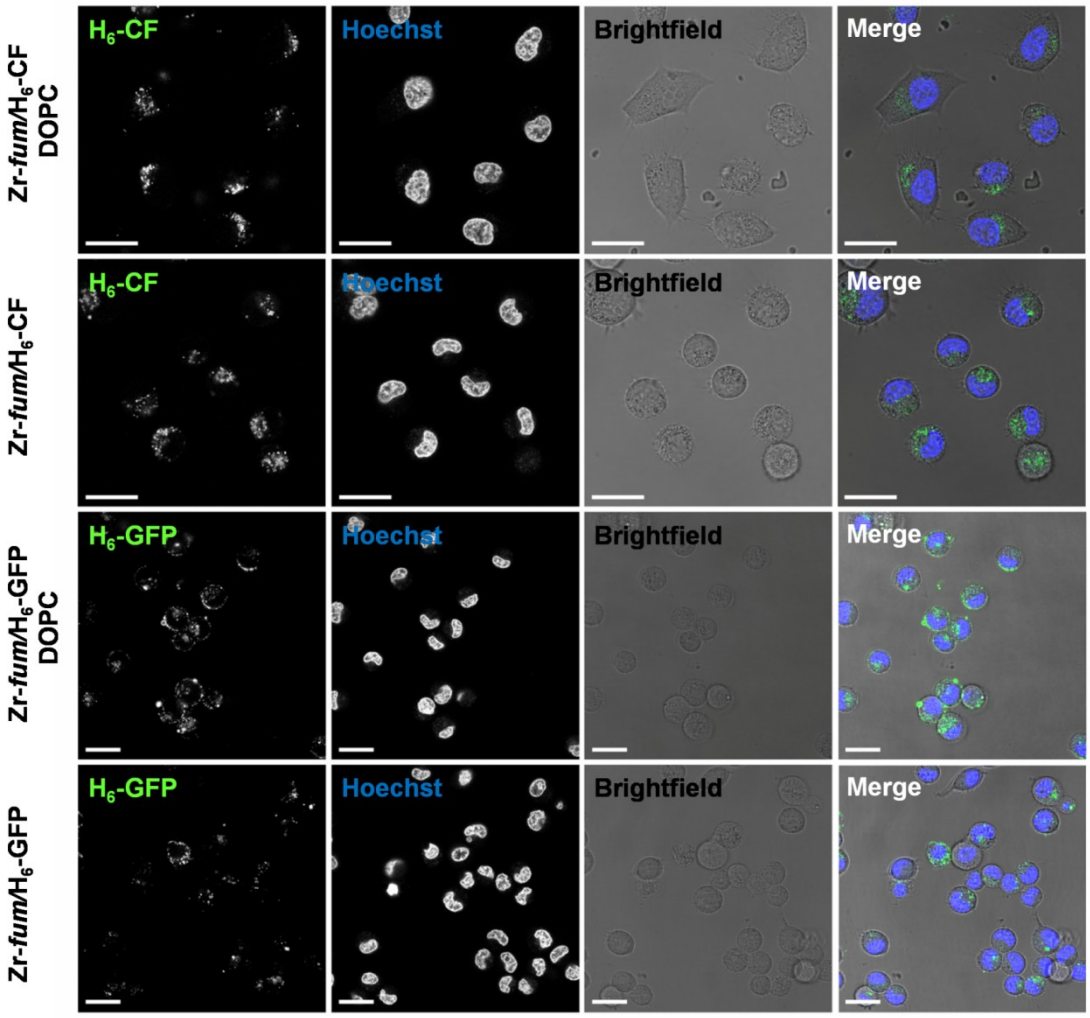

Figure 44: Analysis of the influence of the addition of DOPC to functionalized Zr-*fum* NPs on cellular uptake. After functionalization of 30 µg Zr-fum NPs with 0.22 nmol H_6-CF (first and second row) or H_6-GFP (third and fourth row), 10.8 nmol DOPC (first and third row; final concentration in the well 21.6 µM) were added to the solution. The samples were incubated on KB_*wt* cells for 24 h and images of live cells in PBS (pH 7.4) were taken by CLSM. First column: fluorescence of H_6-CF or H_6-GFP at 488 nm; second column: staining of nucleus using Hoechst dye; third column: brightfield images; fourth column: merge of all three channels. Scale bars: 25 µm.

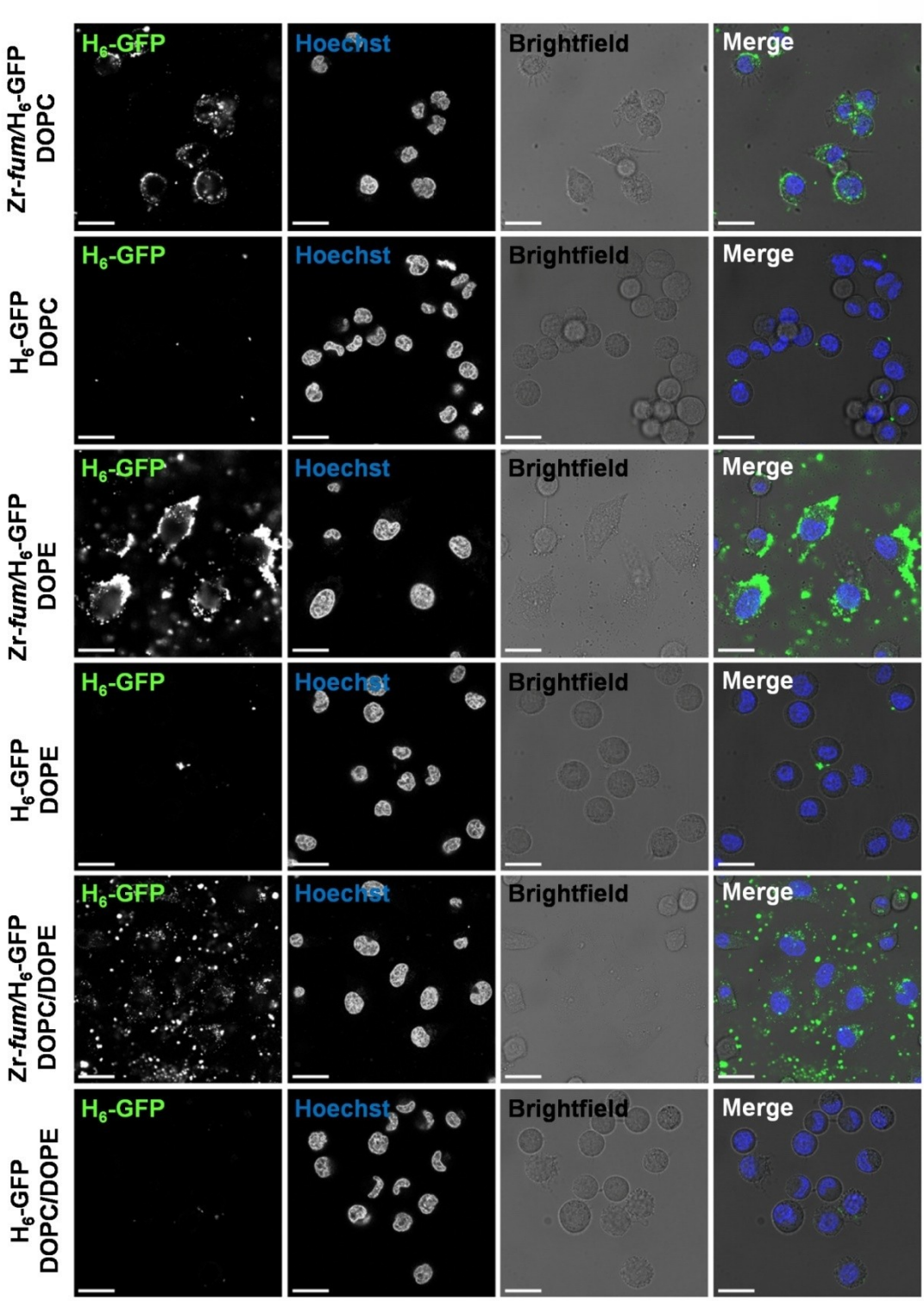

Figure 45: Analysis of the influence of the addition of DOPC and/ or DOPE to Zr-*fum*/H_6-GFP NPs on cellular uptake and endosomal escape. After functionalization of 30 µg Zr-*fum* NPs with 0.22 nmol H_6-GFP, 10.8 nmol DOPC (first row), 10.8 nmol DOPE (third row) or a mixture of 5.4 nmol DOPC and 5.4 nmol DOPE (fifth row) were added. Optionally mixturesH_6-GFP/ lipid mixtures were prepared without the addition of Zr-*fum* NPs (second, fourth, sixth row). The samples were incubated on KB_*wt* cells for 24 h and images of live cells in PBS (pH 7.4) were taken by CLSM. First column: fluorescence of H_6-GFP at 488 nm; second column: staining of nucleus using Hoechst dye; third column: brightfield images; fourth column: merge of all three channels. Scale bars: 25 µm.

CLSM images confirm the results of the flow cytometry experiments described above (Figure 43) in which the addition of DOPC enhanced cellular uptake of functionalized Zr-*fum* NPs.

Regarding the intracellular distribution of H_6-GFP or H_6-CF there is no significant difference between samples with or without DOPC.

Furthermore the addition of a second phospholipid, DOPE, was investigated. As described above DOPE is supposed to have endosomolytic properties. H_6-GFP carries a nuclear localization signal, thus after successful endosomal escape it should diffuse to the nucleus resulting in a distinct nuclear signal. Figure 45 depicts the investigation of the intracellular distribution of Zr-*fum*/H_6-GFP after the addition of DOPC, DOPE or a mixture of DOPC and DOPE. As a control, the effect of just mixing the phospholipids with H_6-GFP without the addition of Zr-*fum* NPs was evaluated. Compared to the addition of DOPC Figure 45 (first and second row), the addition of DOPE lead to agglomeration of Zr-*fum*/H_6-GFP Figure 45 (third row) without further enhancement of cellular uptake or visible change in intracellular distribution. This can probably be explained by the fact that DOPE tends to form non-bilayer structures under physiologic conditions and can destabilize membranes [167]. The agglomeration on the cellular surface could be reversed upon the addition of DOPC Figure 45 (fifth and sixth row). Contrary to the initial assumption that DOPE would enhance the endosomal escape, no change in intracellular distribution of H_6-GFP could be observed. Samples without Zr-*fum* NPs did not lead to any cellular uptake, demonstrating again that the MOFs are absolutely needed for successful cellular uptake of H_6-GFP.

3.2.10.2 Evaluation of different peptides to enhance endosomal escape

The endosomal escape seemed to be the main bottle neck when using different MOF NPs as carriers. Therefore, different His-tagged peptides were designed which were proposed to enhance the endosomal escape. An overview of the different peptides including their identification numbers is listed in Table 8.

To investigate their general feasibility for their usage in cell experiments, their influence on metabolic activity was investigated on HUH7_*wt* cells (Figure 46) after 48 h incubation. Up to a concentration of 5 µM none of the lytic peptides exhibited significant toxicity.

Table 8: Overview of lytic peptides

ID	Description
855	H_6-CMA-2
856	H_6-LauA
857	H_6-K$(OleA)_2$
858	H_6-$K_3$$(OleA)_2$
859	H_6-R_3-K$(OleA)_2$

ID: identification numbers; LauA: lauric acid; OleA: oleic acid, α-amino acids are abbreviated in one-letter code. Peptides were synthesized by Dr. Ulrich Lächelt (Pharmaceutical Biotechnology, LMU München).

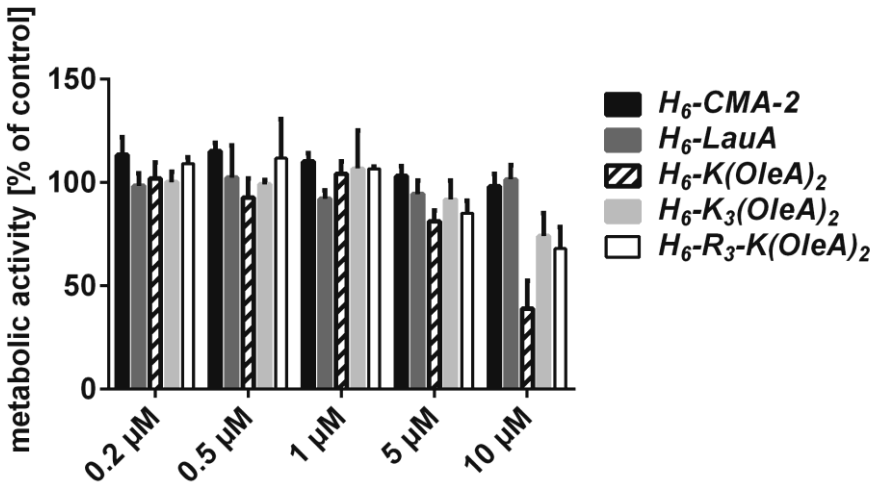

Figure 46: Evaluation of cytotoxicity of different lytic peptides. HUH7_*wt* cells were incubated with different concentrations of different lytic peptides for 48 h. Metabolic activity was determined by MTT assay. Data are presented as % metabolic activity of control cells, treated just with HBG. ± SD (n=5).

To evaluate the influence of the different lytic peptides on destabilizing the endosomal membrane and to compare their pH dependent lytic activity, an erythrocyte leakage assay was carried (Figure 47). CMA-2 (***855***: H_6 modified CMA-2) is a melittin derivative first synthesized by Boeckle *et al*. [169]. It was designed to shift the lytic activity of melittin at pH 7 leading to high toxicity including cell lysis, to the lower endosomal pH of 5. Therefore positively charged domains of melittin, which are important for its lytic activity were modified with glutamic acid residues or histidine residues. These residues are fully protonated at acidic pH restoring complete lytic activity of the peptides [169, 170]. ***856***-***859*** are newly designed peptides.

In hemolysis studies (Figure 47) all different peptides showed pH dependent lytic activity with the highest lytic potential at the late endosomal pH 5.5. H_6-CMA-2 exhibited the highest lytic activity, while H_6-LauA exhibited the lowest, but still showed pH dependency. Comparing the different oleic acid containing peptides,

incorporation of additional lysines (H_6-K_3-K($OleA)_2$) seemed to reduce pH specificity, while the additional three arginines (H_6-R_3-K($OleA)_2$) did not make any difference. Afterwards the effect of including these lytic peptides in cellular uptake experiments using Zr-*fum* MOF NPs as carrier to deliver H_6-GFP was evaluated (Figure 48).

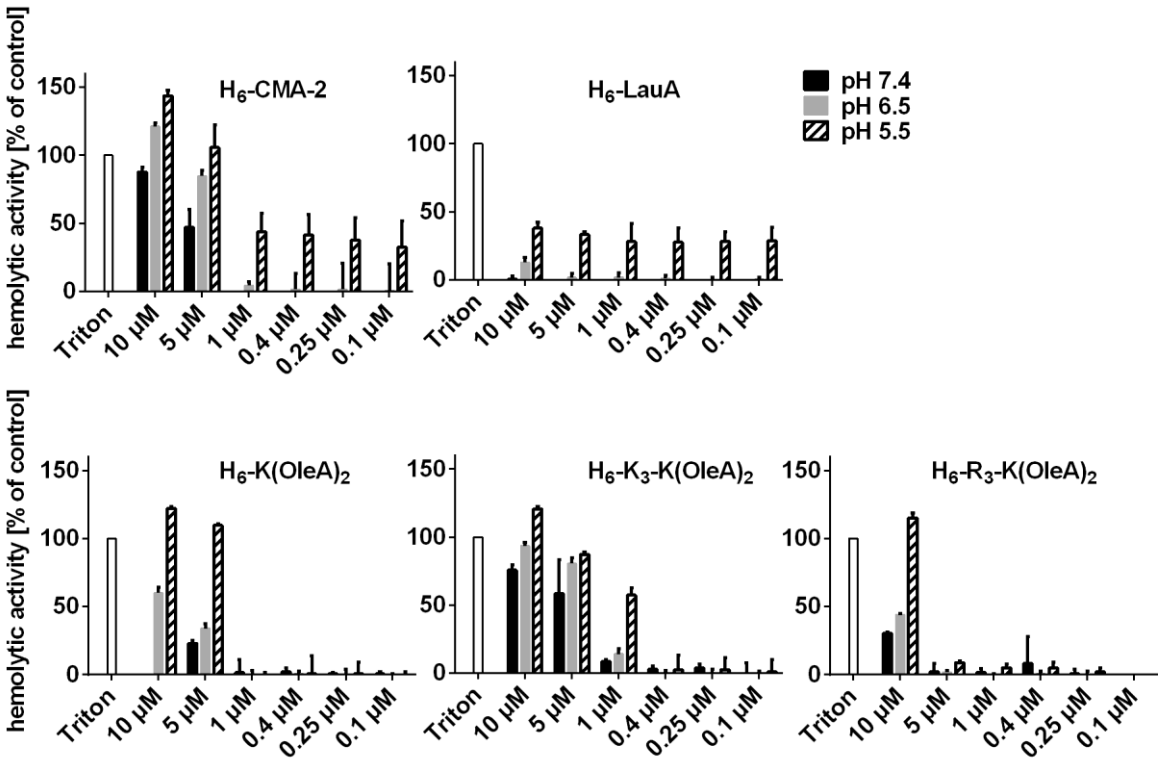

Figure 47: Erythrocyte leakage assay of different lytic peptides. Evaluation of lytic activity of His-tagged lytic peptides at physiological pH 7.4 (black), early endosomal pH 6.5 (grey) and late endosomal pH 5.5 (pattern). Data are presented as % of Triton treated cells ± SD (n=4).

H_6-peptides were mixed with H_6-GFP at a molar ratio of two (H_6-peptide; 0.148 nmol, H_6-GFP; 0.074 nmol) and incubated with 10 µg Zr-*fum* NPs before incubation on HUH7_*wt* cells for 24 h. Subsequently, the influence of the lytic peptides on the endosomal escape was evaluated by CLSM (Figure 48). 0.148 nmol H_6-peptide equals a final concentration of 0.5 µM in the well, which is far lower than the effective concentrations determined in the hemolysis study. Taking into consideration that the final endosomal concentrations might be much higher, the used concentrations are reasonable. Just mixing of H_6-GFP and H_6-peptide without the addition of Zr-*fum* MOF NPs did not lead to visible cellular uptake of H_6-GFP (data not shown). In summary, all Zr-*fum*/H_6-GFP + H_6-lytic peptide combinations resulted in slight cellular uptake, but coming along with agglomeration of H_6-GFP. In general, endosomal

escape was not visibly enhanced. Just in case of H_6-CMA-2 (Figure 48a) destruction of the cellular nucleus occurred, indicating endosomal escape, though H_6-GFP was still just visible in cellular vesicles.

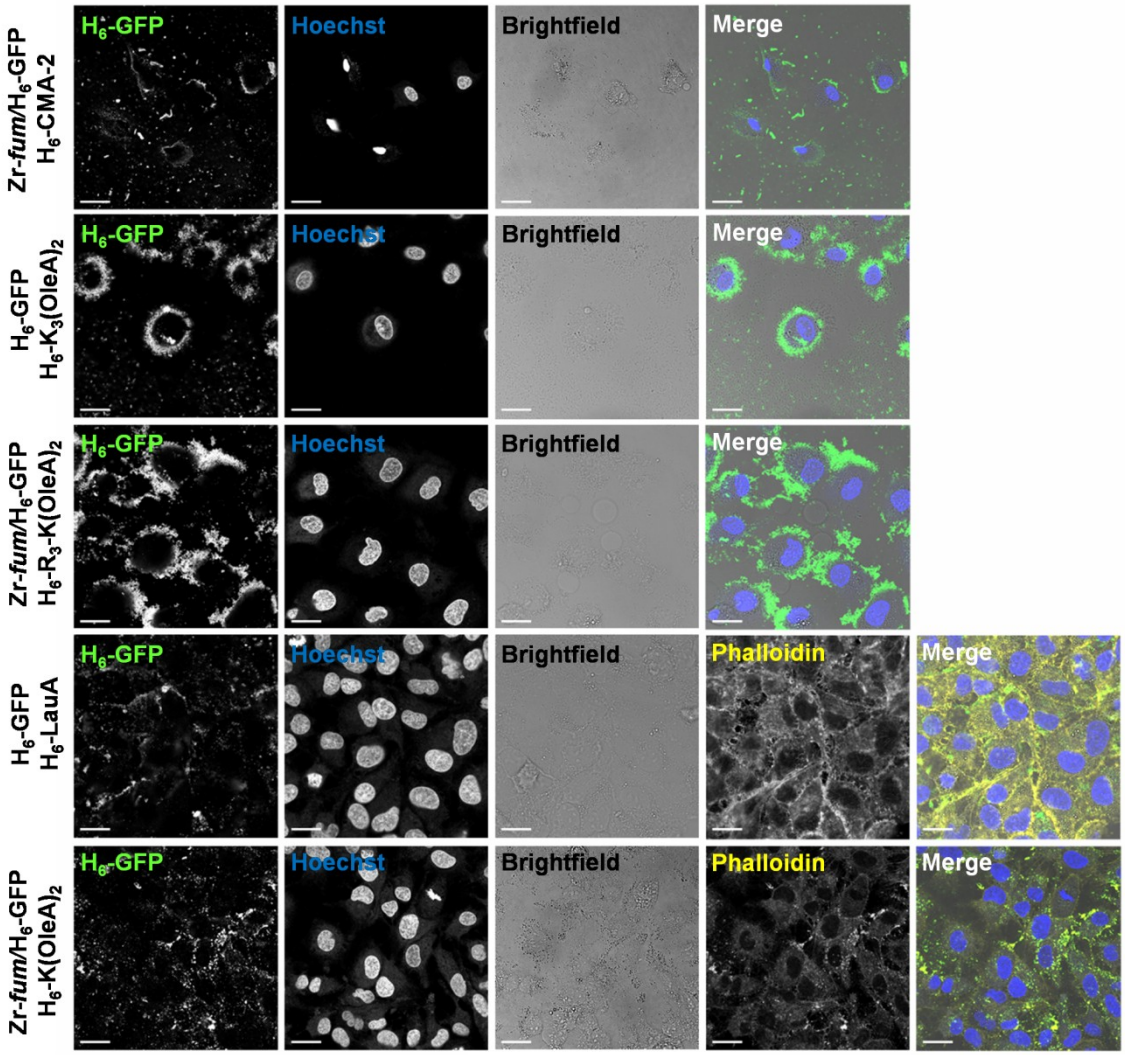

Figure 48: Cellular uptake of Zr-*fum*/H_6-GFP additionally functionalized with H_6-lytic peptides. After functionalization of 10 µg Zr-*fum* NPs with 0.074 nmol H_6-GFP, 0.148 nmol H_6-CMA-2 (first row), H_6-K_3(OleA)$_2$ (second row), H_6-R_3-K(OleA)$_2$ (third row), H_6-LauA (fourth row) or H_6-K(OleA)$_2$ (fifth row). The samples were incubated on HUH7_*wt* cells for 24 h and images of live cells in PBS (pH 7.4) were taken by CLSM. First column: fluorescence of H_6-GFP at 488 nm; second column: staining of nucleus using Hoechst dye; third column: brightfield images; fourth column (fourth and fifth row): F-Actin staining using phalloidin rhodamine; fourth or fifth column: merge of all three or four channels. Scale bars: 25 µm.

Samples containing 20 µg Zr-*fum* NPs were also evaluated but did not lead to enhanced cellular uptake or enhancement of endosomal escape. Functionalization with 1.5 times H_6-peptide (0.22 nmol) was investigated for H_6-CMA-2, H_6-K_3-(OleA)$_2$ and H_6-R_3-K(OleA)$_2$ resulting in all cases in agglomeration and extracellular binding of GFP, without cellular uptake.

3.2.10.3 Evaluation of the effect of DBCO-K-H_6-K(H_6-DBCO)$_2$ modified H_6-GFP on cellular uptake and endosomal escape

In another attempt to overcome the two particular barriers, the intracellular delivery and the endosomal escape. H_6-GFP was modified with DBCO-K-H_6-K(H_6-DBCO)$_2$ using the acid labile AzMMMan as a linker (Figure 49).

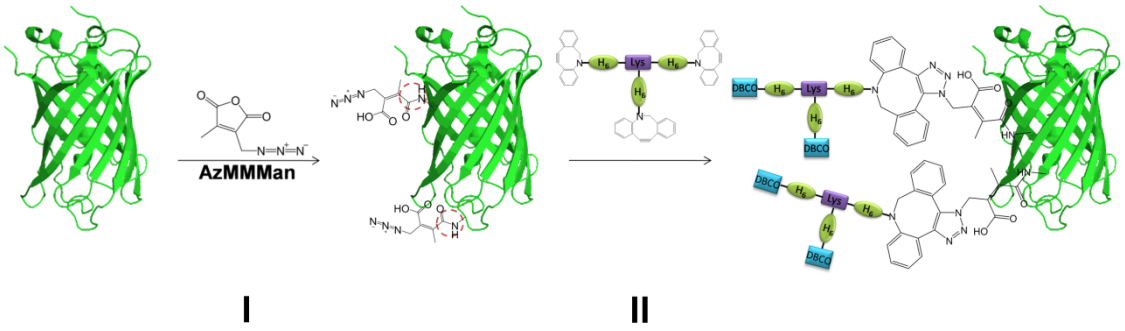

Figure 49. Modification of H_6-GFP with AzMMMan and DBCO-K-H_6-K(H_6-DBCO)$_2$. H_6-GFP was incubated with AzMMMan at a molar ratio of 1:8 for 2 h at 25 °C (I). After purification, DBCO-K-H_6-K(H_6-DBCO)$_2$ was added at a molar ratio of H_6-GFP : DBCO-K-H_6-K(H_6-DBCO)$_2$ of 1:25 (1:1 if calculated on the lysines of H_6-GFP) and incubated for 3 h at 37 °C (II).

The positive effect of the addition of histidines on overcoming these two barriers, has amongst others, been extensively investigated in our lab [141]. The addition of this huge amount of 18 histidines should on the one hand result in a high positive surface charge mediating unspecific interaction with negatively charged cell membranes and therefore enhance cellular uptake. More importantly, with a pKa of the imidazole groups around six, histidines offer high endosomal buffer capacity [171]. To investigate the effect of this modification, H_6-GFP was used as a model protein. To assure that after successful endosomal escape, the native protein can be regained, H_6-GFP was first modified with an acid labile linker (azidomethyl-methylmaleic anhydride, AzMMMan) (Figure 49, I), to which DBCO-K-H_6-K(H_6-DBCO)$_2$ could then be coupled via click-chemistry (Figure 49, II). The effective acid labile modification of proteins with this linker has first been shown by Maier *et al.* [54]. The AzMMMan linker was synthesized as has been described previously [107]. The successful modification of H_6-GFP with the AzMMMan linker was proven by further conjugation via click-chemistry to a DBCO-PEG_{5000}. This modification can be investigated on SDS PAGE. Successful modification is indicated by the retardation of H_6-GFP-

AzMMMan-DBCO- PEG_{5000} at the top of the gel (Figure 50a). Additionally the acid lability of this modification could be shown by incubation of the samples in PBS pH 4, pH 5, pH 6 and pH 8 for 2 h at 37 °C, followed by analysis on SDS PAGE (Figure 50b).To not destroy the labile AzMMMan linkage, the samples were loaded on the gel without prior boiling.

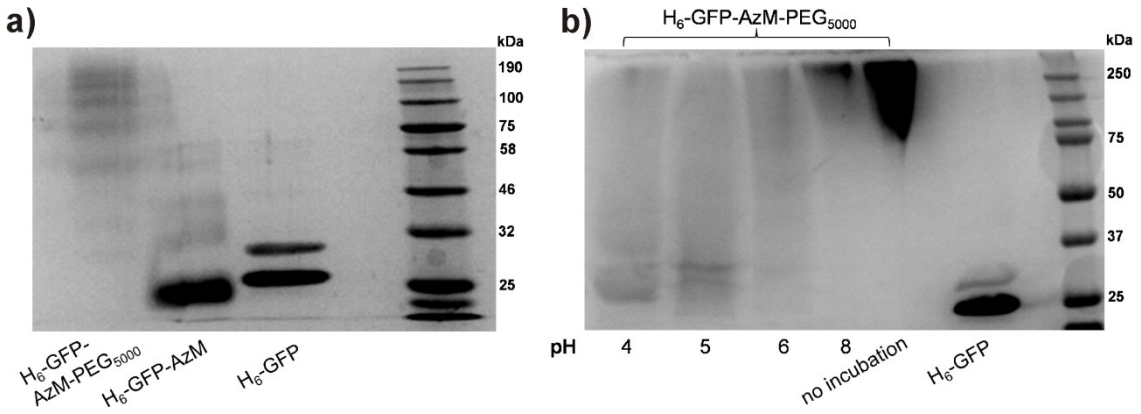

Figure 50: Acid labile modification of H_6-GFP. After modification of H_6-GFP with azidomethyl-methylmaleic anhydride (AzM), DBCO-PEG_{5000} was coupled to the linker via click-chemistry. Different samples were subjected to SDS PAGE without prior boiling. a) from left to right: H_6-GFP-AzM-PEG_{5000}, H_6-GFP-Azm, H_6-GFP, empty, Blue Prestained Protein Standard, Broad Range (NEB, Germany). b) pH dependent cleavage of AzM-PEG_{5000}. Samples containing GFP-Azm-PEG_{5000} were incubated with PBS at indicated pH for 2 h at 37 °C. From left to right: pH 4, pH 5, pH 6, pH 8, without incubation, pure H_6-GFP, empty, Precision Plus Protein standard (BioRad, USA).

The successful modification of H_6-GFP with PEG_{5000} is depicted in Figure 50a (first lane), indicated by the band at the top of the gel. Compared to PEG_{5000} modified H_6-GFP, AzMMMan modified H_6-GFP or pure H_6-GFP show bands at the GFP specific size of 26.9 kDa. The second visible band for pure H_6-GFP is probably a result of not boiling the sample. Secondary structures, which would otherwise be destroyed upon subjecting them to higher temperatures might be left intact. The pH lability of the modification is shown in Figure 50b. Bands at the top of the gel indicate freshly prepared samples, or samples which were incubated at pH 8. If samples are incubated at pH 6, bands start to smear, indicating a slight cleavage of AzMMMan-PEG_{5000} resulting in bands at the size of free GFP for the incubation at pH 4 and 5. After successful verification of the modification of H_6-GFP with AzMMMan, H_6-GFP-AzMMMan was modified with DBCO-K-H_6-K(H_6-DBCO)$_2$ (Figure 49, II). H_6-GFP-AzMMMan was incubated with DBCO-K-H_6-K(H_6-DBCO)$_2$ at a molar ratio of 1:25 (1:1 if calculated on the lysines of H_6-GFP) and incubated for 3 h at 37°C.

Afterwards, the effect on cellular uptake and escape of endolysosomal vesicles was investigated by CLSM. Therefore, 30 µg Zr-*fum* MOF NPs were functionalized with either 0.1 nmol, 0.3 nmol or 0.4 nmol of the modified H_6-GFP. Afterwards HeLa_*wt* cells were incubated with the functionalized Zr-*fum* NPs for 24 h followed by imaging of the live cells. Images of each condition are depicted in Figure 51.

The modification with 0.1 nmol H_6-GFP-AzMMMan-DBCO-K-H_6-K(H_6-DBCO)$_2$ did not lead to an enhancement neither in cellular uptake nor in the endolysosomal escape. The modification with 0.3 nmol H_6-GFP-AzMMMan-DBCO-K-H_6-K(H_6-DBCO)$_2$ lead to enhanced cellular uptake as well as endolysosomal escape (Figure 51a, second row). Although no visible endosomal escape occurred in the better part of the cells. The modification with 0.4 nmol H_6-GFP-AzMMMan-DBCO-K-H_6-K(H_6-DBCO)$_2$ (Figure 51a, third row) did not make an improvement, but rather lead to agglomerates. Incubation of cells without the addition of MOF NPs did not show any cellular uptake (Figure 51b), but in case of 0.4 nmol H_6-GFP-AzMMMan-DBCO-K-H_6-K(H_6-DBCO)$_2$, agglomerates are visible.

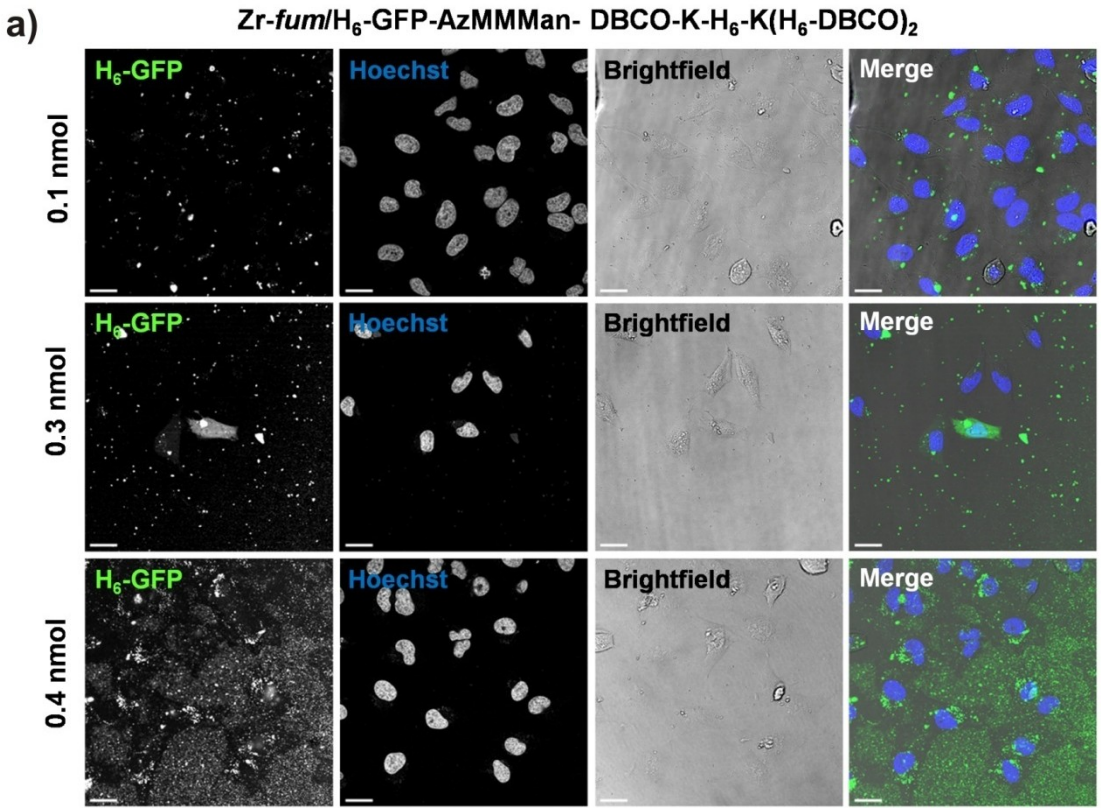

Figure 51 (first part): Cellular uptake of H_6-GFP-AzMMMan-DBCO-K-H_6-K(H_6-DBCO)$_2$ functionalized Zr-*fum* MOF NPs. After incubation of HeLa_*wt* cells with different samples for 24 h, CLSM images of live cells were taken in PBS (pH 7.4). a) Zr-*fum* NPs were functionalized with different amounts of H_6-GFP-AzMMMan-DBCO-K-H_6-K(H_6-DBCO)$_2$. Scale bars: 25 µm.

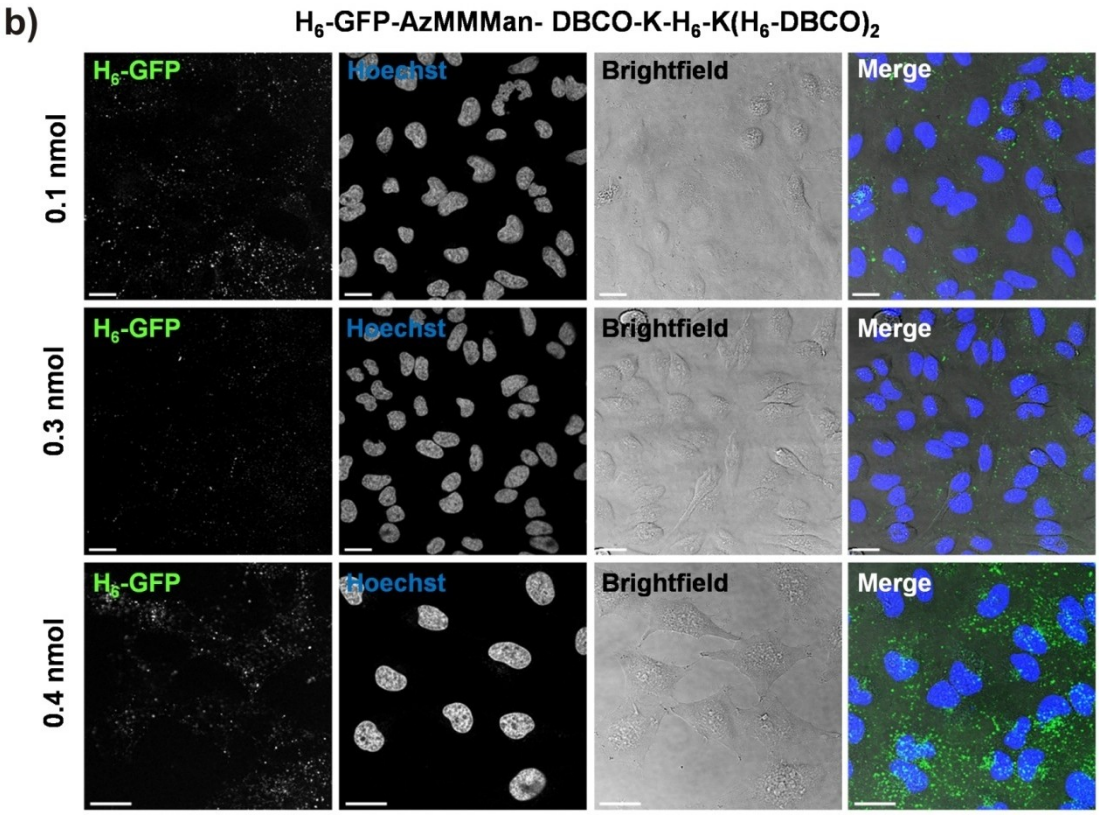

Figure 51 (continued): Cellular uptake of H_6-GFP-AzMMMan-DBCO-K-H_6-K(H_6-DBCO)$_2$ functionalized Zr-*fum* MOF NPs. After incubation of HeLa_*wt* cells with different samples for 24 h, CLSM images of live cells were taken in PBS (pH 7.4). b) Control incubations of HeLa_wt cells with different amounts of H_6-GFP-AzMMMan-DBCO-K-H_6-K(H_6-DBCO)$_2$ without the addition of Zr-*fum* NPs. Scale bars: 25 µm.

3.2.11 Investigation of cellular uptake using luciferase as a read-out system

The following short chapter is included to present the initial experiments to establish a luciferase based read-out system similar to the one which is used on a regular basis in our lab for the analysis of pDNA and siRNA transfections. The chapter points at the bottlenecks of the system laying the foundation for further improvements and applications.

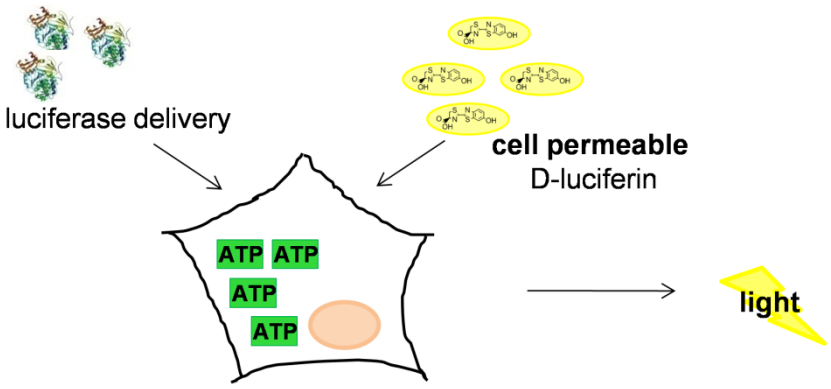

Figure 52: Delivery of luciferase. After delivery of luciferase, cell permeable D-luciferin is added. Successfully delivered luciferase is able to use endogenous ATP to react with D-luciferin resulting in light which can then be used for a read-out.

After successful purification and verification of functionality (3.2.2), binding of luciferase to MOF NPs was investigated. For the reasons described above, experiments were carried out using Zr-*fum* MOF NPs.

70 ng H_6-luciferase were incubated for 15 min with 50 µg Zr-*fum* NPs. Unbound H_6-luciferase was removed (centrifugation and removal of supernatant) and resulting functionalized MOF NPs were washed another three times with PBS (pH 7.4). After each step, samples of 10 µg functionalized MOF NPs were drawn. RLU/well were measured for all different samples, PBS (pH 7.4) and 14 ng H_6-luciferase.

Figure 53a shows a high H_6-luciferase activity for pure H_6-luciferase (white bar) which just slightly decreases after incubation with Zr-*fum* MOF NPs (black bar). After several washing steps (grey bars), measurable luciferase activity decreases a bit, indicating washing away of unbound H_6-luciferase, but all in all H_6-luciferase can be bound to Zr-*fum* MOF NPs without disturbance of its functionality.

Ahead of the transduction experiments (Figure 55), the potential of measuring intracellular luciferase activity by just adding D-luciferin to the buffer was evaluated in stable KB_eGFPLuc cells (Figure 53b).

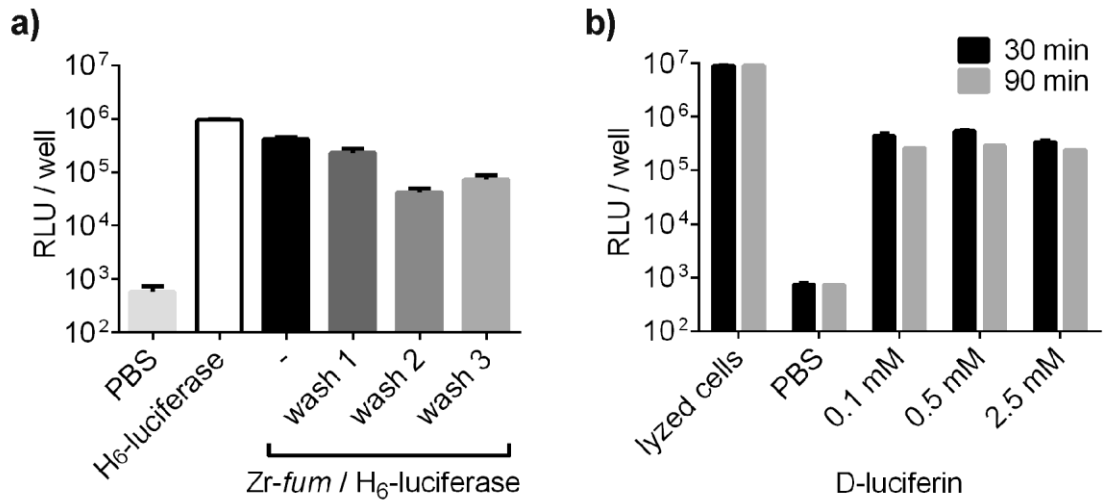

Figure 53: Evaluation of H_6-luciferase binding to Zr-*fum* MOF NPs and luciferase activity in live cells. a) 14 ng H_6-luciferase were incubated with 10 µg Zr-*fum* MOF NPs for 15 min. Functionalized Zr-*fum* NPs were washed three times with PBS. RLU/ well of PBS (light grey), 14 ng pure H_6-luciferase (white), Zr-*fum*/H_6-luciferase (black) and Zr-*fum*/H_6-luciferase after washing steps with PBS (Wash 1-3, different shades of grey) were measured ±SD (n=3). b) Evaluation of luciferase activity in live stable KB_eGFPLuc cells upon the addition of different amounts of D-luciferin, compared to the luciferase activity in lyzed cells measured with LAR buffer. ±SD (n=3). Luciferase activity was measured on a Centro LB 960 plate reader luminometer (Berthold Technologies, Bad Wildbad, Germany).

The initial idea was that intracellular delivered luciferase ought to be able to use endogenous ATP to react with D-luciferin. Therefore, successful delivered functional luciferase should be distinguishable from just extracellular bound luciferase. The luciferase signal in live cells was a bit lower than in lyzed cells. The concentration and incubation time of D-luciferin did not make any difference. 0.5 mM D-luciferin were chosen for further transduction experiments as it equals the amount of D-luciferin in LAR buffer (Table 2).

After successful modification of Zr-*fum* NPs with H_6-luciferase, and proving that intracellular luciferase can be measured in live cells, cellular uptake and cytotoxicity in KB_*wt* cells were investigated. Based on previous results (3.2.10) the effect of different additional functionalization units to enhance cellular uptake and endosomal escape was evaluated. To enhance cellular uptake, the experiment was either performed in serum free medium, or DOPC was added. The addition of DOPE, H_6-Inf, H_{20}-tag or incubation in medium containing the endolysosomotropic agent chloroquine, was supposed to enhance endosomal escape. As can be seen in Figure 54 none of the functionalization units or functionalized MOF NPs had an influence on the metabolic activity of the cells.

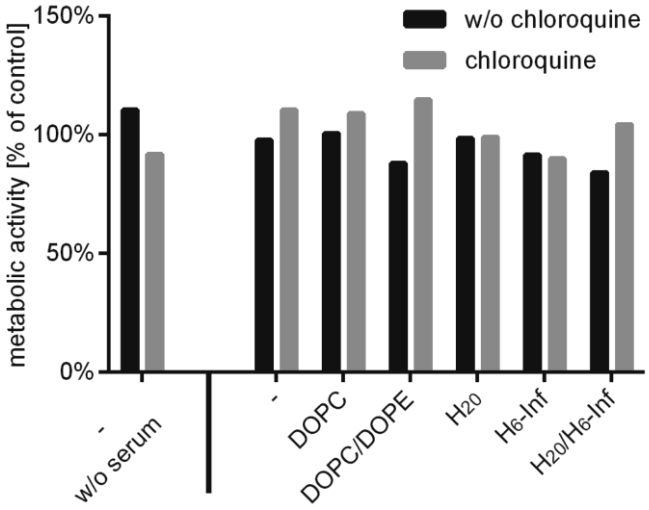

Figure 54: Evaluation of metabolic activity of transduction of luciferase into KB_*wt* cells. KB_*wt* cells were incubated with Zr-*fum*/H_6-luciferase (10 µg/500 ng, 0.008 nmol) including different additional functionalization units as indicated. 28.8 nmol DOPC; 14.4 nmol DOPC/14.4 nmol DOPE; 0.03 nmol H_{20}; 0.13 nmol H_6-Inf; 0.13 nmol H_{20}/0.13 nmol H_6-Inf; – describes the incubation just with Zr-*fum*/H_6-luciferase. Samples w/o chloroquine (black) were incubated for 48 h- samples with chloroquine (grey) for 4 h on the cells. Metabolic activity was determined by MTT assay. Data are presented as % metabolic activity of control cells, treated just with HBG. Samples were prepared in duplicates.

The results of the transduction experiments are depicted in Figure 55. Just measuring the activity of delivered H_6-luciferase in live cells by the addition of cell-permeable D-luciferin to the buffer did not result in any significant signal (Figure 55, black and white bar).

As no positive control was available the different steps of the delivery experiments were evaluated in a quick more detailed approach. To analyze if the cellular uptake simply did not work, or if the bottleneck was the endosomal escape, after measuring the extracellular luciferase signal (data not shown) the cells were lyzed and the total luciferase signal was measured. The signal of intracellular luciferase was then determined as the total luciferase signal minus the extracellular luciferase signal (Figure 55, dark grey and light grey bars).

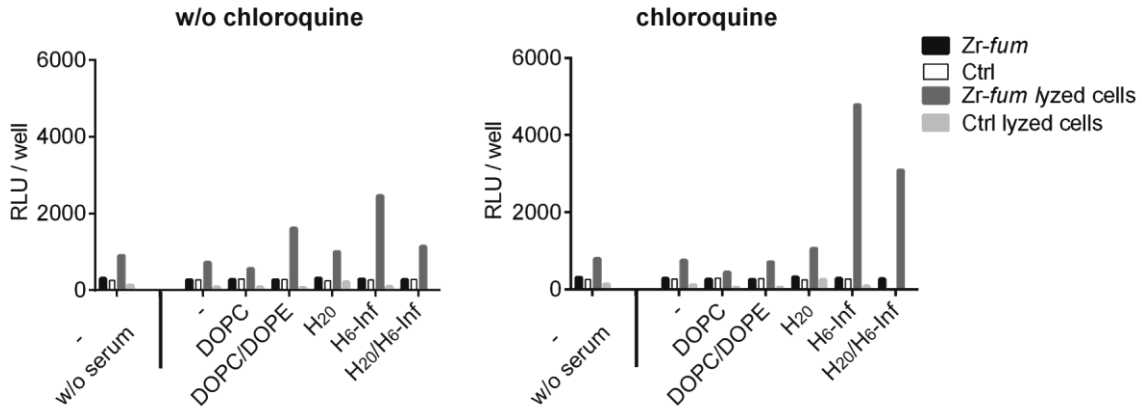

Figure 55: Transduction of luciferase into KB_*wt* cells. KB_*wt* cells were incubated with Zr-*fum*/H_6-luciferase (10 µg/500 ng, 0.008 nmol) including different additional functionalization units as indicated. 28.8 nmol DOPC;14.4 nmol DOPC/14.4 nmol DOPE; 0.03 nmol H_{20}; 0.13 nmol H_6-Inf; 0.13 nmol H_{20}/0.13 nmol H_6-Inf; – describes the incubation just with Zr-*fum*/H_6-luciferase. Samples w/o chloroquine (left) were incubated for 48 h - samples with chloroquine (right) for 4 h on the cells. As control (Ctrl), cells were incubated with H_6-luciferase and functionalization units without the addition of Zr-*fum* NPs. After incubation, intracellular luciferase was measured after the addition of 0.5 mM D-luciferin (black and grey). Dark grey and light grey: substraction of extracellular measured luciferase signal from luciferase signal of lyzed cells (measurements were carried out in LAR buffer). Samples were prepared in duplicates.

Just samples containing additional functional units to improve the endosomal escape resulted in an enhanced luciferase signal. The best result was obtained for samples containing the endosomolytic peptide H_6-Inf. If incubation was carried out in the presence of chloroquine luciferase signals could be enhanced. Samples in the presence of H_6-Inf and chloroquine exhibited the highest luciferase signal suggesting the main bottleneck being the endosomal escape. Another problem seems to be the transduction efficiency. Compared to measuring pure H_6-luciferase signal, the signal measured after transduction is very low. This in addition to the fact that the luciferase signal in live cells was in general lower than in lyzed cells adds up to an explanation why measuring a signal of transduced H_6-luciferase in live cells was quite hard.

3.2.12 Application of Zr-*fum* MOF NPs as a carrier system for apoptosis inducing peptides and cytochromeC

In regard to the intracellular distribution of internalized entities, the major limitation of the presented concept as delivery system seems to be the entrapment within cellular vesicles. To further evaluate the potential of Zr-*fum* MOF NPs as carrier system for cytosolic cargo release, transduction of membrane impermeable bioactive pro-apoptotic peptides (Bak, Bad, KLK) and mitochondrial cytochromeC (CytC) protein was investigated and cell killing was used as reporter for successful cytosolic delivery. H_6-Bak and H_6-Bad are two peptides derived from the BH3 domain of Bak and Bad proteins which promote apoptosis by inducing the mitochondrial mediated apoptosis pathway [172].

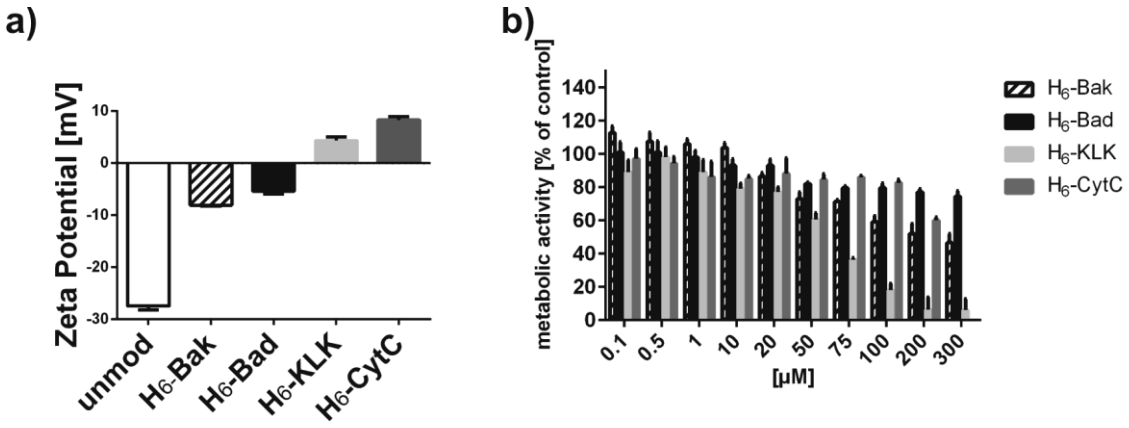

Figure 56: Evaluation of toxicity and binding to Zr-*fum* MOF NPs of apoptosis inducing H_6-peptides and H_6-CytC. a) H_6-Bak (pattern), H_6-Bad (black), H_6-KLK (light grey) or H_6-CytC (dark grey) were incubated with Zr-*fum* MOF NPs (Zr-*fum*/His-tag: 0.2 mg/nmol) for 15 min at room temperature. Samples were diluted to 0.1 mg Zr-*fum*/mL HBG (pH 7.4) and zeta potential was measured. Zeta potentials were calculated by the Smoluchowski equation, each sample was measured 3 times with 10 to 30 subruns at 25 °C. All samples differ significantly $p<0.0001$ from non-modified Zr-*fum* MOF NPs. White: unmodified Zr-*fum* MOF NPs, pattern: H_6-Bak, black: H_6-Bad, light grey: H_6-KLK, dark grey: H_6-CytC. b) After incubation of HeLa_*wt* cells with different peptide concentrations for 48 h, metabolic activity was determined by MTT assay. H_6-Bak (pattern), H_6-Bad (black), H_6-KLK (light grey) or H_6-CytC (dark grey). Data are presented as % metabolic activity of control cells ± SD (*n*=5). Please note that for H_6-CytC the highest concentration was 200 µM. Adapted from [158].

H_6-KLK is an artificial peptide designed to selectively kill bacteria [173]. It also disrupts mitochondrial membranes while showing low extracellular toxicity [174]. CytC is a small mitochondrial heme protein and a crucial player in the intrinsic mitochondrial apoptosis pathway. After its release from the mitochondrion it binds to apoptotic protease-activating factor 1, APAF-1, promoting assembly of the apoptosome and activation of cell death [175]. H_6-tags were chemically conjugated to

CytC or integrated at the N-terminus of the peptide sequences derived from the BH3 domain of Bak and Bad proteins [172] or the artificial KLK peptide [173, 174]. Binding of these pro-apoptotic factors to Zr-*fum* NPs was confirmed by measuring the change of zeta potential upon addition of the MOF NPs (Figure 56a). For biological evaluation, HeLa_*wt* cells were treated for 48 h with different concentrations of pure pro-apoptotic factors to evaluate their intrinsic cytotoxicity (Figure 56b). Changes in metabolic activity were evaluated by MTT assay. Up to a concentration of 20 µM all pro-apoptotic factors did not exhibit any detectable toxicity. Afterwards cells were treated for 48 h with functionalized Zr-*fum* NPs (Zr-*fum*/H_6-Bak, /H_6-Bad, /H_6-KLK or /H_6-CytC, 10 µM) and cell viability was assessed again by MTT assay (Figure 57).

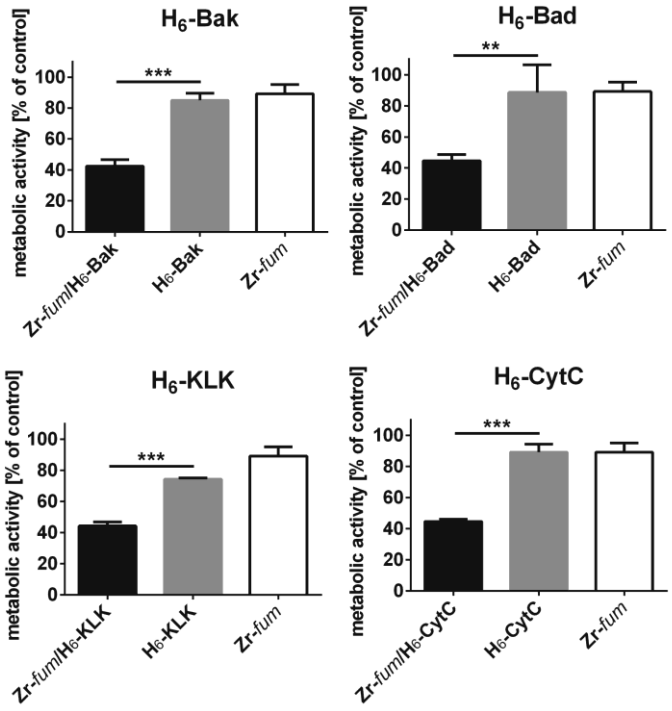

Figure 57: Induction of cell killing upon incubation with Zr-*fum* MOF NPs functionalized with pro-apoptotic factors. HeLa_*wt* cells were incubated for 48 h with Zr-*fum* NPs functionalized with different pro-apoptotic factors. Final concentration of H_6-Bak, H_6-Bad, H_6-KLK, H_6-CytC was 10 µM. Black bar: functionalized Zr-*fum* NPs, grey bar: pure pro-apoptotic factor, white bar: bare Zr-*fum* NPs. Data are presented as % metabolic activity of control cells ± SD (*n*=3) (MTT assay). *** p<0.0003, ** p<0.01. Adapted from [158].

Approximately 60 % cell killing could be detected in case of all functionalized Zr-*fum* NPs. These findings indicate that, despite the bottleneck of vesicular entrapment, significant fractions of cargo molecules were able to escape and induce biological effects in the cytosol.

4 Discussion

4.1 Delivery of nanobodies for imaging of target proteins

This chapter has been adapted from:

Intracellular Delivery of Nanobodies for Imaging of Target Proteins in Live Cells. Ruth Röder, Jonas Helma, Tobias Preiß, Joachim O. Rädler, Heinrich Leonhardt, Ernst Wagner. Pharmaceutical Research (2017), 34(1):161-174.

The intracellular delivery of nanobodies is of high research interest in the field of live cell imaging as well as for therapeutic approaches, but so far there is no effective delivery system available. In the current thesis, a library of sequence-defined oligoaminoamides was evaluated for their ability to efficiently transduce a GFP binding nanobody in different folic acid receptor expressing recombinant HeLa cell lines. Previous protein delivery experiments from our lab were based on the bioreversible covalent modification of proteins with oligomers [52-54]. The current work aimed at non-covalent formulation, where nanoparticles are formed through mixing nanobody and oligomers. An initial oligomer library screen identified two oligomers (***735*** and ***734***) which upon incubation with a GFP binding nanobody lead to stable nanoparticle formation, resulting in efficient intracellular delivery and specific co-localization of labeled nanobody with GFP-tagged target proteins. These two oligomers differ only by the presence (***735***) or absence (***734***) of folate as possible targeting ligand. They were initially described by He *et al*. [142] for testing receptor-mediated delivery of pDNA and siRNA, contain a PEG molecule for nanoparticle shielding and prevention of unspecific aggregations, optionally linked with folic acid as receptor-targeting ligand, attached to a four-arm core oligoaminoamide structure comprising a repeating sequence pattern of four cationizable Stp units (assumed to facilitate endosomal escape) and one terminal cysteine per arm (for disulfide formation between neighboring oligomers). According to our initial screening experiments, comparing these two oligomers ***735*** or ***734*** with the others, the relatively larger size and topology seems to be critical for effective nanobody/oligomer nanoparticle formation. In this setup especially the inclusion of cysteines within the oligomeric structure was proven as absolutely necessary for the generation of stable nanoparticles by disulfide crosslinkage upon cysteine oxidation during the four hours incubation after nanobody/oligomer mixing. Blocking of the

terminal cysteine mercapto groups by maleimide prevented stable particle formation. Oligomer disulfide formation before nanobody complexation was also unsuccessful (data not shown).This is consistent with previous work which demonstrated favorable effects of disulfide crosslinkage on siRNA polyplex formation [48, 50, 176, 177]. As the R_H of the nanobodies used in this study is comparable to the R_H of siRNA of 2.2 nm [178, 179] but with a far lower negative charge density the requirement of cysteines for stable nanoparticle formation fits well with the aforesaid findings. Altogether the findings suggest that the oligomers are first non-covalently bound to the surface of nanobodies where disulfide formation between oligomers triggers the formation of stable nanoparticles.

Oligomer ***735*** contains folic acid as targeting ligand. We could show that upon short-time incubation nanoparticles containing oligomer ***735*** exhibit higher cellular uptake compared to particles formed with the non-targeted oligomer ***734***. Cellular internalization was shown to be blocked upon pre-incubation of the cells with free folic acid, suggesting receptor-dependent cellular uptake. Nanoparticles containing oligomer ***734*** however also lead to quite high uptake efficiency when cellular uptake was investigated after 24 h. There are two possible explanations for this; one is the positive charge of the protein/oligomer complexes. In contrast to almost neutral polyplexes formed with highly negatively charged nucleic acids, nanobodies do not effectively neutralize the cationic charges of the oligomer, exhibiting a zeta potential of ~+15 mV for all nanobody/oligomer formulations. Therefore positively charged nanobody/oligomer nanoparticles may interact with cells either via the folate receptor or directly with negative charged cell membranes, leading to receptor independent cellular uptake. Moreover, FCS data indicate formation of slightly more nanobody nanoparticles for ***734*** than for ***735***, resulting in more nanobody cargo being available for non-specific cellular uptake.

The escape from endolysosomal cellular vesicles is suggested to be the major bottleneck for cytosolic delivery of macromolecules. Therefore it is not surprising to observe a significant fraction of internalized labeled nanobody remaining localized in intracellular vesicles. The four arm oligomer ***735*** contains a significant number of sixteen cationizable Stp [46] units (sixty-four aminoethylene units) per oligomer which by endosomal acidification should be sufficient to trigger endosomal escape analogously to the ‘proton sponge effect’ as observed for polyethylenimine [19, 180]. It has to be noted that according to the oligomer screen by He *et al.* [142] as well as

related work on pDNA delivery [47, 141], ***735*** and analogous oligomers did not possess optimized proton sponge activity and require the presence of the endolysomotropic agent chloroquine for effective endosomal escape. In this respect the successful protein delivery at slightly higher doses of incorporated ***735*** carrier is encouraging, but the persistent endosomal bottleneck for this oligomer also suggests an important direction for further optimization of oligomers.

To broaden our delivery technology towards a universal nanobody transduction system, we also applied it for a lamin binding nanobody. After successful delivery of α-lamin-Nb, we were able to visualize nuclear lamin, an endogenous target, and to follow it through the whole cell cycle in living cells. As nanobodies have a quite conserved structure and differ mostly in their complementarity determining regions, their properties in terms of oligomer binding ought to be quite similar. Thus this system should be transferable to many kinds of nanobodies- being able to target a huge variety of intracellular molecular targets.

4.2 MOF nanoparticles as a defined carrier system for His-tagged functional units

This chapter has been adapted from:

Multifunctional nanoparticles by coordinative self-assembly of His-tagged units with metal-organic frameworks. Ruth Röder, Tobias Preiß, Patrick Hirschle, Benjamin Steinborn, Andreas Zimpel, Miriam Höhn, Joachim O. Rädler, Thomas Bein, Ernst Wagner, Stefan Wuttke and Ulrich Lächelt. Journal of the American Chemical Society (2017), 139(6): 2359-2368.

MOFs are quite new compounds with their fields of application ranging from their usage as catalysts [84, 131-135], over absorption and storage of various materials [82, 83, 123] to their use in biomedical applications such as drug delivery [85, 86, 125, 136, 137] or imaging [121]. In the work at hand, a new functionalization concept of MOF nanoparticles (NPs) which was developed by Dr. Ulrich Lächelt (Group Leader, Pharmaceutical Biotechnology, LMU München) was to be evaluated referring to its use as possible carrier for the cellular delivery of various His-tagged compounds. The strategy uses the coordinate interaction such as the imidazole function of histidine acting as Lewis base and coordinatively unsaturated metal sites

present on the external surface of MOF NPs acting as Lewis acid, to assemble different functional units.

The binding via coordination interactions has already been shown in different contexts [44, 149, 156, 157]. Here it was applied to generate multifunctional core-shell MOF NPs for efficient delivery, taking on the one hand advantage of the fact that the metal binding sites are naturally abundant and homogeneously distributed within the MOFs, and on the other hand of the inherent His-tag of many recombinant proteins. The same interaction is routinely used for the purification of recombinant proteins by immobilized metal ion chromatography [154, 155]. If not, His-tags can easily be integrated into peptides or proteins by synthetic, recombinant or bioconjugation techniques.

At first, the general feasibility of the selected MOF NPs, MIL-88A, HKUST-1 and Zr-*fum*, was evaluated by MTT assay. MIL-88A and Zr-*fum* MOF NPs exhibited good bio-compatibility. Just HKUST-1 showed a decrease in metabolic activity, which could be overcome by shortening the incubation time.

Secondly, the theory of the acid labile assembly of MOF NPs and His-tags was investigated. The acid labile release is of special importance, if a shielding and targeting layer has to be released to expose novel often endosomolytic activity. It can additionally be applied to free a cargo from its carrier. These investigations were carried out using Zr-*fum* MOF NPs as carrier and H_6-A647N as cargo. FCS measurements as well as photometric evaluations showed pH dependent disassembly of His-tag and MOF in both irrespective experiments.

The long-term stability as well as stability under cell culture conditions of His-tag functionalized MOF NPs was also investigated by photometric detection and FCS measurements. Photometric detections revealed stable association of Zr-*fum*/H_6-A647N for 24 h in aqueous solution at pH 7.4. FCS, measurements showed stable association of Zr-*fum*/H_6-A647N in DMEM media containing 10 % FBS.

In the following, cellular uptake could be observed using all three different MOF NPs and H_6-CF or H_6-GFP as cargo molecule. In case of HKUST-1 and MIL88-A agglomerations were clearly visible in CLSM images, confirming what had been observed in FCS and DLS measurements (data not shown). Therefore for further delivery experiments we focused on Zr-*fum* MOF NPs as a carrier.

A distinct advantage of the self-assembly concept demonstrated in this work is the one-step multifunctionalization of MOF NPs by simultaneously mixing different His-

tagged compounds with bare MOF NPs, being able to easily introduce efficient shielding and multifunctional targeting units as well as different small molecule therapeutics at the same time, without the need of complex further modifications. This assumption was first evaluated by FCCS measurements using two His-tagged proteins, H_6-GFP and Atto647N labeled H_6-Transferrin (H_6-Tf*) with distinct fluorescence spectra. The analysis of the cross-correlation showed a high ratio of co-localization of both proteins which was interpreted as attachment of H_6-GFP and H_6-Tf* to the surface of the same MOF NP. In accordance with the FCCS measurements, cellular uptake experiments in HeLa_*wt* cells using these double functionalized Zr-*fum* MOF NPs showed considerable intracellular co-localization of H_6-GFP and H_6-Tf*. However, H_6-Tf* was also take up on its own. This can be explained by the fact that HeLa_*wt* cells express the transferrin receptor leading to MOF independent uptake of H_6-Tf*. Although a higher uptake could be observed in the presence of MOF NPs suggesting simultaneous uptake of several H_6-Tf* coupled to the same MOF NP.

To elucidate the cellular uptake pathway, of the functionalized MOF NPs, we investigated the endocytotic process using different cellular uptake inhibitors. The results indicated an energy dependent uptake route which seemed to be dominated by macropinocytosis as amiloride showed the greatest inhibitory effect on cellular uptake of Zr-*fum*/H_6-GFP MOF NPs. A minor effect of genestein suggested that caveloae mediated endocytosis might also be involved to some extend. Recently, Orellana- Tavra *et al.* [181] investigated the endocytosis mechanism of UiO-66 (Zr^{4+}/terephtalate) MOF NPs. Consistently with the data presented here, they also showed that cellular uptake of UiO-66 is energy dependent with distinct involvement of macropinocytosis. However they identified clathrin- mediated endocytosis having a major contribution [181], too.

To evaluate the potential of Zr-*fum* MOF NPs as carrier system for cytosolic cargo release, delivery of membrane impermeable bioactive pro-apoptotic peptides (Bak, Bad, KLK) and mitochondrial cytochromeC (CytC) protein was investigated. Notably, for the purification of H_6-CytC carrying a H_6-tag after chemical conjugation, immobilized metal-ion chromatography was used which is based on the same principle as the binding to the MOF NPs. The utilization of the same interaction for isolation and subsequent attachment to the carrier system is considered a very convenient and robust manufacturing process. Binding of these pro-apoptotic factors

to Zr-*fum* NPs was confirmed by measuring the change in zeta potential upon addition of MOF NPs. Assessing cell viability in HeLa_*wt* cells, approximately 60 % cell killing could be detected for Zr-*fum* MOF NPs functionalized with all four different pro-apoptotic factors. Without the addition of MOF-NPs, all pro-apoptotic factors did not exhibit any detectable toxicity up to a concentration of 20 µM. These findings indicate that, despite the bottleneck of vesicular entrapment, significant fractions of cargo molecules were able to escape and induce biological effects in the cytosol.

In summary, the simultaneous assembly of different functional units with Zr-*fum* MOF NPs as well as transport into living cells indicated the successful creation of multifunctional programmable MOF NP interfaces capable of manipulating cellular processes.

5 Summary

Targeted nanoparticles holding different bioresponsive functional units can be used as carriers in biomedical applications, for the intracellular delivery of therapeutic compounds such as nucleic acids or proteins and for related purposes such as bioimaging. Nanobodies, similar to antibodies, have a conserved core sequence and variations occur mostly in their complementary determining regions. An efficient carrier for one nanobody should be generally applicable to all kinds of nanobodies. In the first part of the thesis, such a universal carrier for nanobodies was developed. For establishing a system for the efficient delivery of nanobodies into living cells, a broad screening experiment was conducted evaluating different targeted and non-targeted sequence-defined oligoaminoamide carriers from our lab, for their potential to efficiently transduce a GFP binding nanobody into living HeLa_PCNA-GFP cells. The screening resulted in two related sequence-defined oligoaminoamide carriers, ***735*** and ***734*** with and without folic acid as receptor targeting ligand. These two oligomers additionally contain sixteen Stp units to interact with the nanobody and enhance endosomal escape, cysteines to enhance oligomer crosslinking leading to the formation of stable nanoparticles and PEG as hydrophilic shielding agent. Mixing of nanobodies with these two oligomers and incubation for air-oxidation of cysteines lead to nanoparticles with a small size around 20 nm. They were suitable to efficiently deliver different labeled nanobodies into cells, as evidenced by interaction of nanobodies with their target proteins. This delivery approach was evaluated in two additional recombinant cell lines, HeLa_Actin-GFP and HeLa_Tubulin-GFP cells proving that the transduction of a GFP binding nanobody works in different cell lines. Furthermore, this delivery concept was extended to a lamin binding nanobody broadening the scope to direct imaging of an endogenous target.This demonstrates that due to the conserved structure and size of nanobodies, the evaluated sequence-defined oligomers can be used to deliver nanobodies with diverse intracellular targets.

Delivery systems are often optimized for the delivery of one class of compounds. It would be a great advancement to have a carrier system for multiple simultaneous cargos, which can be adapted to any application without intensive further investigations. The described multifunctionalization concept of metal-organic frameworks (MOFs) is one step into this direction.

In the second part of the thesis, the suitability of MOFs as carriers for various His-tagged cargos was to be investigated. The inherent properties of the individual compounds (metal ions or metal oxide clusters of MOF nanoparticles (NPs), His-tag containing functional units) and the reversible nature of the His-tag-MOF interaction account for the strength of this approach. The used MOFs, MIL-88A, HKUST-1 and Zr-*fum* did not exhibit any cytotoxicity under the used conditions. Furthermore, cellular uptake of H_6-GFP or H_6-carboxyfluorescein functionalized MOF NPs was evaluated. All MOFs exhibited efficient cellular uptake, although MIL-88A and HKUST-1 showed high agglomerations compared to Zr-*fum*. Therefore further experiments were carried out with Zr-*fum* MOF NPs only. Co-delivery of H_6-GFP and Atto647N labeled H_6-transferrin demonstrated the possible one-step multifunctionalization of the MOF NPs by simply simultaneously mixing different His-tagged units with bare MOF NPs. This shows the great advantage of the presented carrier system, as diverse functional compounds, just having a His-tag in common can be delivered at the same time without further modifications. The delivery of three pro-apoptotic peptides, Bad, Bak and KLK and the mitochondrial protein cytochromeC led to approximately 60 % cell killing, demonstrating the versatility for possible biomedical applications.

6 Appendix

6.1 Abbreviations

5ANV	Fmoc-5-azido-L-norvaline
Acr	Acridine
APAF-1	Apoptotic protease-activating factor 1
APC	Allophycocyanin
AzMMMan	Azidomethyl-methylmaleic anhydride
BrMMan	3-(Bromomethyl)-4-methyl-2,5-furandione
CDR	Complementarity determining region
CF	Carboxyfluorescein
Cit	Citraconic acid amide
CLSM	Confocal laser scanning microscopy
CPP	Cell penetrating peptide
CUS	Unsaturated metal sites
CytC	CytochromeC
DAPI	4′,6-Diamidino-2-phenylindole
DBCO	Dibenzocyclooctyl
DMMan	Dimethylmaleic anhydride
DIPEA	N,N-Diisopropylethylamine
DMF	Dimethylformamide
DMSO	Dimethylsulfoxide
DNA	Desoxyribonucleic acid
DOPC	1,2-Dioleoyl-*sn*-glycero-3-phosphocholine
DOPE	1,2-dioleoyl-*sn*-glycero-3-phosphoethanolamine
EDTA	Ethylenediaminetetraacetic acid
GFP	Green fluorescence protein
FBS	Fetal bovine serum
FCCS	Fluorescence cross-correlation spectroscopy
FCS	Fluorescence correlation spectroscopy
FITC	Fluorescein isothiocyanate
FolA	Folic acid
GBP	GFP binding protein
Gtp	Glutaroyl tetraethylene pentamine

H_6	Hexahistidine
HBG	Hepes-buffered glucose
HBTU	N,N,N′,N′-Tetramethyl-O-(1H-benzotriazol-1-yl)uranium hexa-fluorophosphate
HcAb	Heavy-chain only camelid antibodies
HEPES	2-(4-(2-Hydroxyethyl)-1-piperazinyl)-ethansulfonic acid
HGFR	Hepatocyte growth factor receptor
His-tags	Oligohistidine- tags
HKUST-1	Hong Kong University of Science Technology -1
HOBt	1-Hydroxy-benzotriazole
iPS	Induced pluripotent stem cells
IPTG	Isopropyl β-D-1-thiogalactopyranoside
IR	Infrared spectroscopy
LauA	Lauric acid
Luc	Luciferase
MIL-88A	Materials from Institute Lavoisier -88A
MOF	Metal-organic framework
mRNA	Messenger ribonucleic acid
MTBE	Methyl *tert*-butyl ether
MTT	3-(4,5-Dimethylthia-zol-2-yl)-2,5-diphenyltetrazolium bromide
MWCO	Molecular weight cut-off
Nb	Nanobody
NEM	N-Ethylmaleimide
NHS	N-Hydroxysuccinimide
NLS	Nuclear localization signal
NMP	N-Methyl-2-pyrrolidone
NP	Nanoparticle
NTA	Nitrilotriacetic acid
OleA	Oleic acid
PAMAM	Polyamidoamine
PBS	Phosphate buffered saline
PCNA	Proliferating-Cell-Nuclear-Antigen
pDNA	Plasmid desoxyribonucleic acid
PEG	Polyethyleneglycol

PEI	Polyethyleneimine
PFA	Paraformaldehyde
PIC	Polyion complex
Ptp	Phtaloly tetraethylene pentamine
Pybop	(Benzotriazol-1-yloxy)-tripyrrolidinophosphonium hexafluoro-phosphate
RNA	Ribonucleic acid
SBU	Secondary building unit
SDS-PAGE	Sodium dodecyl sulfate polyacrylamide gel electrophoresis
SEC	Size exclusion chromatography
siRNA	Small interfering ribonucleic acid
SMCC	Succinimidyl 4-(N-maleimidomethyl)cyclohexane-1-carboxylate
SPDP	N-Succinimidyl 3-(2-pyridyldithio)propionate
Sph	Succinoyl pentaethylene hexamine
Stp	Succinoyl tetraethylene pentamine
TALENs	Transcription activator-like effector nucleases
Tf	Transferrin
TFA	Trifluoroacetic acid
Tis	Triisopropylsilane
TNF	Tumor necrosis factor
V_{HH}	Single domain antibody fragments
Zr-*fum*	Zirconium-fumaric acid

6.2 Gene and protein sequences

6.2.1 Sequence of EGFPLuc Gene

pET28A / Coding Region

ATGGGCAGCAGCCATCATCATCATCATCACAGCAGCGGCCTGGTGCCGCGCGG
CAGCCATATGGCTAGCATGACTGGTGGACAGCAAATGGGTCGCGGATCCGAAT
TCGAAGACGCCAAAAACATAAAGAAAGGCCCGGCGCCATTCTATCCGCTGGAA
GATGGAACCGCTGGAGAGCAACTGCATAAGGCTATGAAGAGATACGCCCTGGT
TCCTGGAACAATTGCTTTTACAGATGCACATATCGAGGTGGACATCACTTACGCT
GAGTACTTCGAAATGTCCGTTCGGTTGGCAGAAGCTATGAAACGATATGGGCTG
AATACAAATCACAGAATCGTCGTATGCAGTGAAAACTCTCTTCAATTCTTTATGC
CGGTGTTGGGCGCGTTATTTATCGGAGTTGCAGTTGCGCCCGCGAACGACATTT
ATAATGAACGTGAATTGCTCAACAGTATGGGCATTTCGCAGCCTACCGTGGTGT
TCGTTTCCAAAAAGGGGTTGCAAAAAATTTTGAACGTGCAAAAAAAGCTCCCAAT
CATCCAAAAAATTATTATCATGGATTCTAAAACGGATTACCAGGGATTTCAGTCG
ATGTACACGTTCGTCACATCTCATCTACCTCCCGGTTTTAATGAATACGATTTTG
TGCCAGAGTCCTTCGATAGGGACAAGACAATTGCACTGATCATGAACTCCTCTG
GATCTACTGGTCTGCCTAAAGGTGTCGCTCTGCCTCATAGAACTGCCTGCGTGA
GATTCTCGCATGCCAGAGATCCTATTTTTGGCAATCAAATCATTCCGGATACTGC
GATTTTAAGTGTTGTTCCATTCCATCACGGTTTTGGAATGTTTACTACACTCGGA
TATTTGATATGTGGATTTCGAGTCGTCTTAATGTATAGATTTGAAGAAGAGCTGT
TTCTGAGGAGCCTTCAGGATTACAAGATTCAAAGTGCGCTGCTGGTGCCAACCC
TATTCTCCTTCTTCGCCAAAAGCACTCTGATTGACAAATACGATTTATCTAATTTA
CACGAAATTGCTTCTGGTGGCGCTCCCCTCTCTAAGGAAGTCGGGGAAGCGGT
TGCCAAGAGGTTCCATCTGCCAGGTATCAGGCAAGGATATGGGCTCACTGAGA
CTACATCAGCTATTCTGATTACACCCGAGGGGGATGATAAACCGGGCGCGGTC
GGTAAAGTTGTTCCATTTTTTGAAGCGAAGGTTGTGGATCTGGATACCGGGAAA
ACGCTGGGCGTTAATCAAAGAGGCGAACTGTGTGTGAGAGGTCCTATGATTATG
TCCGGTTATGTAAACAATCCGGAAGCGACCAACGCCTTGATTGACAAGGATGGA
TGGCTACATTCTGGAGACATAGCTTACTGGGACGAAGACGAACACTTCTTCATC
GTTGACCGCCTGAAGTCTCTGATTAAGTACAAAGGCTATCAGGTGGCTCCCGCT
GAATTGGAATCCATCTTGCTCCAACACCCCAACATCTTCGACGCAGGTGTCGCA
GGTCTTCCCGACGATGACGCCGGTGAACTTCCCGCCGCCGTTGTTGTTTTGGA

GCACGGAAAGACGATGACGGAAAAAGAGATCGTGGATTACGTCGCCAGTCAAG
TAACAACCGCGAAAAAGTTGCGCGGAGGAGTTGTGTTTGTGGACGAAGTACCG
AAAGGTCTTACCGGAAAACTCGACGCAAGAAAAATCAGAGAGATCCTCATAAAG
GCCAAGAAGGGCGGAAAGATCGCCGTGTAA

6.2.2 Amino acid sequence of H_6-luciferase

Luciferase amino acid sequence (pET28a expression)

MGSSHHHHHHSSGLVPRGSHMASMTGGQQMGRGSEFEDAKNIKKGPAPFYPLED
GTAGEQLHKAMKRYALVPGTIAFTDAHIEVDITYAEYFEMSVRLAEAMKRYGLNTNH
RIVVCSENSLQFFMPVLGALFIGVAVAPANDIYNERELLNSMGISQPTVVFVSKKGLQ
KILNVQKKLPIIQKIIIMDSKTDYQGFQSMYTFVTSHLPPGFNEYDFVPESFDRDKTIA
LIMNSSGSTGLPKGVALPHRTACVRFSHARDPIFGNQIIPDTAILSVVPFHHGFGMFT
TLGYLICGFRVVLMYRFEEELFLRSLQDYKIQSALLVPTLFSFFAKSTLIDKYDLSNLH
EIASGGAPLSKEVGEAVAKRFHLPGIRQGYGLTETTSAILITPEGDDKPGAVGKVVPF
FEAKVVDLDTGKTLGVNQRGELCVRGPMIMSGYVNNPEATNALIDKDGWLHSGDIA
YWDEDEHFFIVDRLKSLIKYKGYQVAPAELESILLQHPNIFDAGVAGLPDDDAGELPA
AVVVLEHGKTMTEKEIVDYVASQVTTAKKLRGGVVFVDEVPKGLTGKLDARKIREILI
KAKKGGKIAV

6.3 Analytical data

6.3.1 Analytics of BrMMan and AzMMMan

^{1}H proton NMR spectra (400 MHz, $CDCl_3$)

3-(Bromomethyl)-4-methyl-2,5-furandione

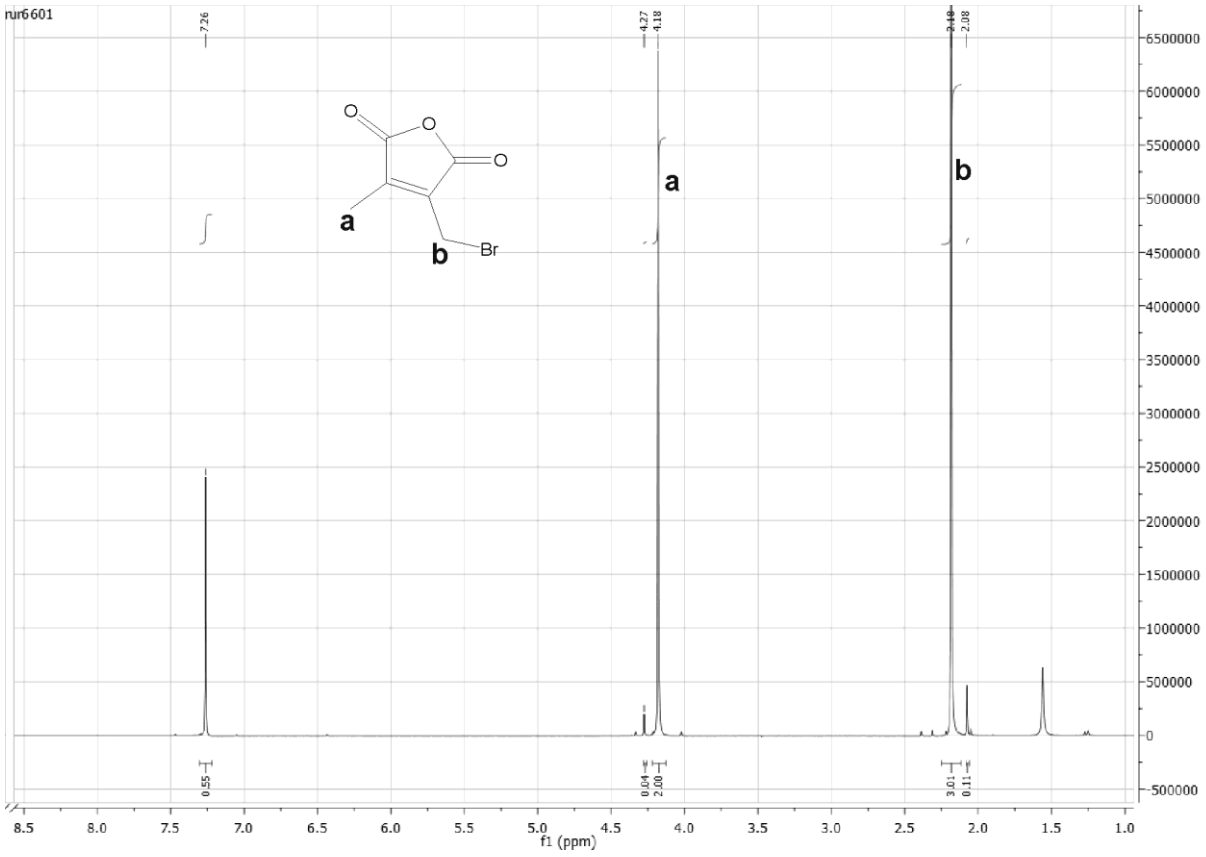

BrMMan: 4.17 (s 2H), 2.17 (s 3H).

DiBrMMan: 4.27 (s 4H)

DMMan: 2.07 (s 6H)

3-(Azidomethyl)-4-methyl-2,5-furandione

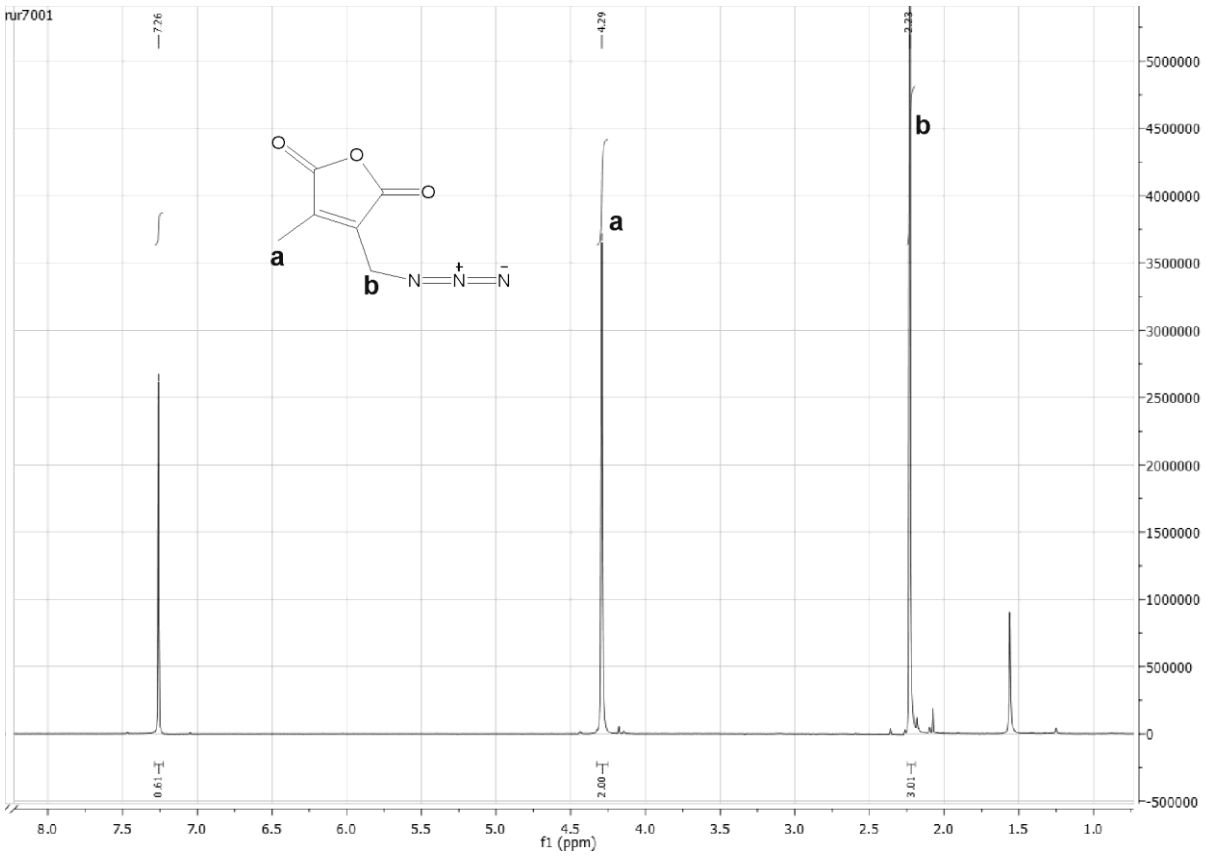

AzMMMan: 4.29 (s, 2H), 2.22 (s, 3H)

6.3.2 Analytics of apoptotic peptides

$\underline{H_6\text{-Bak}}$

Sequence: H_6-GGQVGRQLAIIGDDINR-NH_2

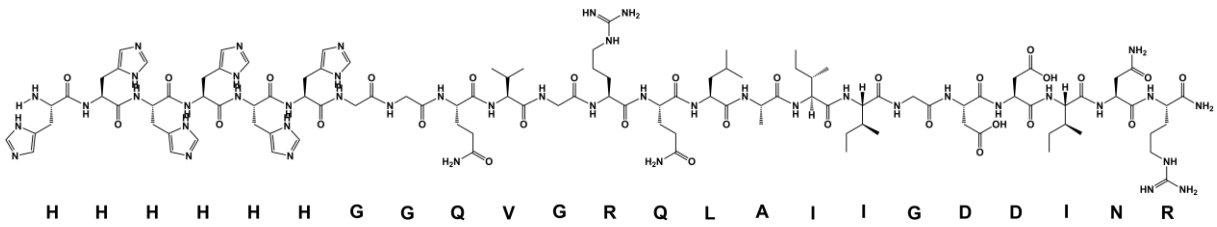

H H H H H H G G Q V G R Q L A I I G D D I N R

Chemical Formula: $C_{110}H_{171}N_{45}O_{30}$
Exact Mass: 2602,3238

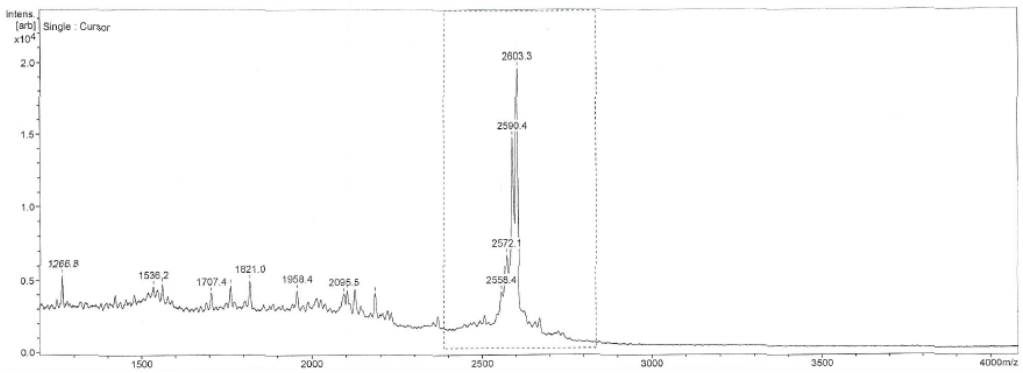

Mass found: 2603.3 $[M+H]^+$

$\underline{H_6\text{-Bad}}$

Sequence: H_6-GNLWAAQRYGRELRRMSDEFVD-NH_2

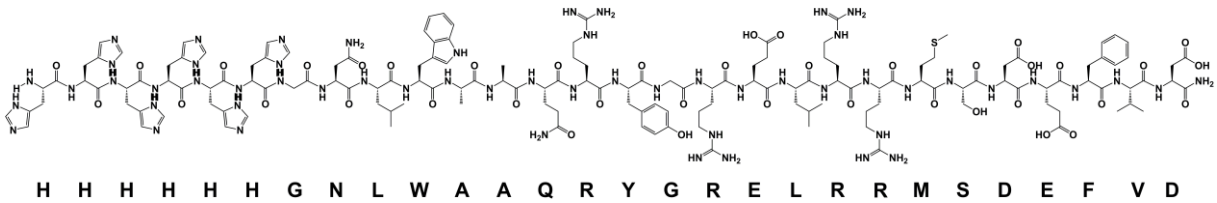

H H H H H H G N L W A A Q R Y G R E L R R M S D E F V D

Chemical Formula: $C_{151}H_{220}N_{56}O_{40}S$
Exact Mass: 3489,6623

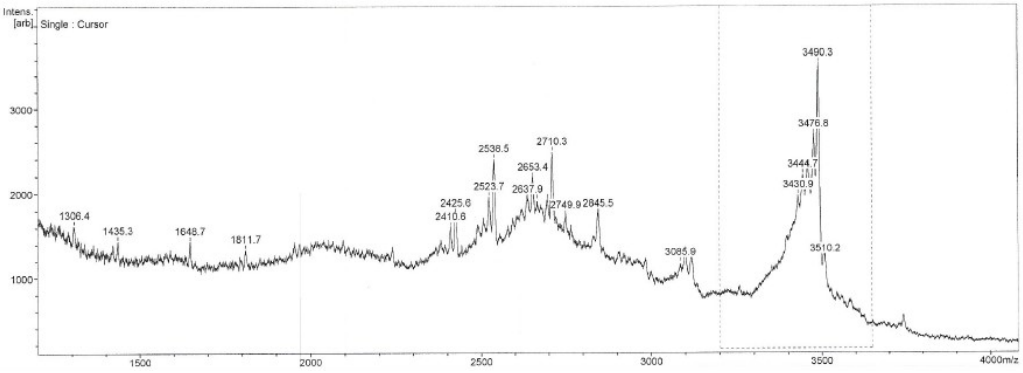

Mass found: 2490.3 $[M+H]^+$

$\underline{H_6\text{-KLK}}$

Sequence: H_6-GGKLAKLAKKLAKLAK-NH_2

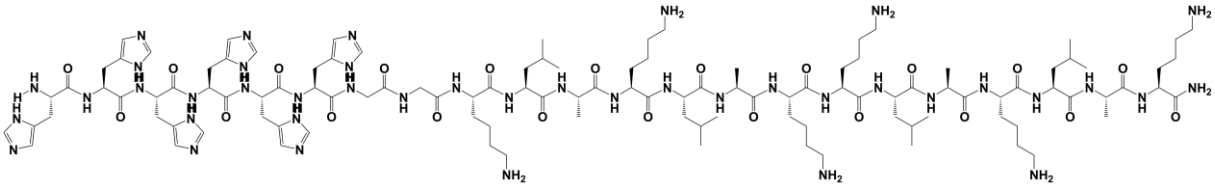

H H H H H H G G K L A K L A K K L A K L A K

Chemical Formula: $C_{112}H_{187}N_{41}O_{22}$
Exact Mass: 2458,4774

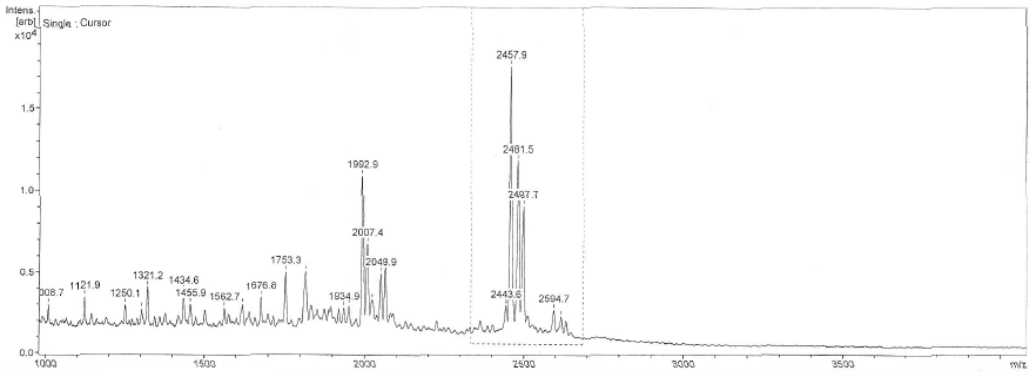

Mass found: 2457.9 $[M+H]^+$, 2481.5 $[M+Na]^+$, 2497.7 $[M+K]^+$

6.4 Publications

6.4.1 Original articles

Ruth Röder, Tobias Preiß, Patrick Hirschle, Benjamin Steinborn, Andreas Zimpel, Miriam Höhn, Joachim O. Rädler, Thomas Bein, Ernst Wagner, Stefan Wuttke and Ulrich Lächelt. (2017) *Multifunctional nanoparticles by coordinative self-assembly of His-tagged units with metal-organic frameworks*. Journal of the American Chemical Society, 139(6): 2359-2368.

Ruth Röder, Jonas Helma, Tobias Preiß, Joachim O. Rädler, Heinrich Leonhardt, Ernst Wagner. (2017) *Intracellular Delivery of Nanobodies for Imaging of Target Proteins in Live Cells.* Pharmaceutical Research, 34(1): 161-174 (Cover).

Andreas Zimpel, Tobias Preiß, **Ruth Röder**, Hanna Engelke, Michael Ingrisch, Michael Peller, Joachim O. Rädler, Ernst Wagner, Thomas Bein, Ulrich Lächelt and Stefan Wuttke. (2016) *Imparting Functionality to MOF nanoparticles by external surface selective covalent attachment of polymers.* Chemistry of Materials, 28(10): 3318-26.

Peng Zhang, Dongsheng He, Philipp Michael Klein, Xiaowen Liu, **Ruth Röder**, Markus Döblinger, Ernst Wagner. (2015) *Enhanced intracellular protein transduction by sequence defined tetra oleoyl-oligoaminoamides targeted for cancer therapy*. Advanced Functional Materials, 25(42): 6627–36.

Andreia F. Jorge, **Ruth Röder**, Petra Kos, Rita S. Dias, Ernst Wagner, Alberto A.C.C. Pais. (2015) *Combining polyethylenimine and Fe(III) for mediating pDNA transfection.* Biochimica et Biophysica Acta (BBA), General Subjects, 1850(6): 1325-35.

6.4.2 Review

Ruth Röder and Ernst Wagner. (2014*) Sequence-defined shuttles for targeted nucleic acid and protein delivery.* Therapeutic Delivery, 5(9): 1025–1045.

6.4.3 Poster presentation and abstract

Linda Beckert and **Ruth Röder**, Jennifer Altomonte, Libor Kostka, Tomas Etrych, Ernst Wagner, *Traceless pH-sensitive coating of viral and non-viral vectores*. CeNS Workshop Venice "Walk and Talk at the Nanoscale" and <Interact> 2015, Munich (Poster prize, 2nd place).

Jennifer Altomonte, **Ruth Röder**, Kim Agnes Munoz Álvarez, D Gunert, Ernst Wagner, Oliver Ebert. (2015) *Development of delivery, targeting, and imaging strategies to improve oncolytic vesicular stomatitis virus therapy for hepatocellular carcinoma*. Zeitschrift für Gastroenterology 53(01).

6.5 Copyright

7 References

1. Wirth T, Parker N, Yla-Herttuala S. History of gene therapy. Gene. 2013;525(2):162-9.
2. Salmon F, Grosios K, Petry H. Safety profile of recombinant adeno-associated viral vectors: focus on alipogene tiparvovec (Glybera((R))). Expert Rev Clin Pharmacol. 2014;7(1):53-65.
3. Semple SC, Akinc A, Chen J, Sandhu AP, Mui BL, Cho CK, et al. Rational design of cationic lipids for siRNA delivery. Nat Biotech. 2010;28(2):172-6.
4. Hatakeyama H, Akita H, Harashima H. A multifunctional envelope type nano device (MEND) for gene delivery to tumours based on the EPR effect: A strategy for overcoming the PEG dilemma. Adv Drug Del Rev. 2010;63(3)152-60.
5. Zhang S, Zhi D, Huang L. Lipid-based vectors for siRNA delivery. J Drug Target. 2012;20(9):724-35.
6. Tagalakis AD, Kenny GD, Bienemann AS, McCarthy D, Munye MM, Taylor H, et al. PEGylation improves the receptor-mediated transfection efficiency of peptide-targeted, self-assembling, anionic nanocomplexes. J Control Release. 2014;174:177-87.
7. Pack DW, Hoffman AS, Pun S, Stayton PS. Design and development of polymers for gene delivery. Nat Rev Drug Discov. 2005;4(7):581-93.
8. Boussif O, Lezoualc'h F, Zanta MA, Mergny MD, Scherman D, Demeneix B, et al. A versatile vector for gene and oligonucleotide transfer into cells in culture and in vivo: polyethylenimine. Proc Natl Acad Sci USA. 1995;92(16):7297-301.
9. Zintchenko A, Philipp A, Dehshahri A, Wagner E. Simple Modifications of Branched PEI Lead to Highly Efficient siRNA Carriers with Low Toxicity. Bioconjug Chem. 2008;19(7):1448-55.
10. Haensler J, Szoka FC, Jr. Polyamidoamine cascade polymers mediate efficient transfection of cells in culture. Bioconjug Chem. 1993;4:372-9.
11. Gunther M, Lipka J, Malek A, Gutsch D, Kreyling W, Aigner A. Polyethylenimines for RNAi-mediated gene targeting in vivo and siRNA delivery to the lung. Eur J Pharm Biopharm. 2011;77(3):438-49.
12. Troiber C, Wagner E. Nucleic Acid Carriers Based on Precise Polymer Conjugates. Bioconj Chem. 2011;22(9):1737-52.
13. Hauswirth WW, Aleman TS, Kaushal S, Cideciyan AV, Schwartz SB, Wang L, et al. Treatment of leber congenital amaurosis due to RPE65 mutations by ocular subretinal injection of adeno-associated virus gene vector: short-term results of a phase I trial. Hum Gene Ther. 2008;19(10):979-90.
14. Nathwani AC, Tuddenham EG, Rangarajan S, Rosales C, McIntosh J, Linch DC, et al. Adenovirus-associated virus vector-mediated gene transfer in hemophilia B. N Engl J Med. 2011;365(25):2357-65.
15. Aiuti A, Cattaneo F, Galimberti S, Benninghoff U, Cassani B, Callegaro L, et al. Gene therapy for immunodeficiency due to adenosine deaminase deficiency. N Engl J Med. 2009;360(5):447-58.
16. Palfi S, Gurruchaga JM, Ralph GS, Lepetit H, Lavisse S, Buttery PC, et al. Long-term safety and tolerability of ProSavin, a lentiviral vector-based gene therapy for Parkinson's disease: a dose escalation, open-label, phase 1/2 trial. Lancet. 2014;383(9923):1138-46.
17. Wagner E. Polymers for siRNA Delivery: Inspired by Viruses to be Targeted, Dynamic, and Precise. Acc Chem Res. 2012;45(7):1005-13.

18. Akinc A, Thomas M, Klibanov AM, Langer R. Exploring polyethylenimine-mediated DNA transfection and the proton sponge hypothesis. J Gene Med. 2005;7(5):657-63.
19. Behr JP. The proton sponge: A trick to enter cells the viruses did not exploit. Chimia. 1997;51(1-2):34-6.
20. Scholz C, Wagner E. Therapeutic plasmid DNA versus siRNA delivery: Common and different tasks for synthetic carriers. J Control Release. 2012;161(2):554-65.
21. Thorp HH. The importance of being r: greater oxidative stability of RNA compared with DNA. Chem Biol. 2000;7(2):R33-6.
22. Peacock H, Kannan A, Beal PA, Burrows CJ. Chemical modification of siRNA bases to probe and enhance RNA interference. J Org Chem. 2011;76(18):7295-300.
23. Wilson RC, Doudna JA. Molecular mechanisms of RNA interference. Annu Rev Biophys. 2013;42:217-39.
24. Remaut K, Symens N, Lucas B, Demeester J, De Smedt SC. Cell division responsive peptides for optimized plasmid DNA delivery: The mitotic window of opportunity? J Control Release. 2014;179:1-9.
25. Hacein-Bey-Abina S, Von Kalle C, Schmidt M, McCormack MP, Wulffraat N, Leboulch P, et al. LMO2-associated clonal T cell proliferation in two patients after gene therapy for SCID-X1. Science. 2003;302(5644):415-9.
26. Kaczmarczyk SJ, Sitaraman K, Young HA, Hughes SH, Chatterjee DK. Protein delivery using engineered virus-like particles. Proc Natl Acad Sci U S A. 2011;108(41):16998-7003.
27. Mendez J, Morales Cruz M, Delgado Y, Figueroa CM, Orellano EA, Morales M, et al. Delivery of chemically glycosylated cytochrome c immobilized in mesoporous silica nanoparticles induces apoptosis in HeLa cancer cells. Mol Pharm. 2014;11(1):102-11.
28. Schlossbauer A, Sauer AM, Cauda V, Schmidt A, Engelke H, Rothbauer U, et al. Cascaded photoinduced drug delivery to cells from multifunctional core-shell mesoporous silica. Adv Healthc Mater. 2012;1(3):316-20.
29. Ray M, Tang R, Jiang Z, Rotello VM. Quantitative Tracking of Protein Trafficking to the Nucleus Using Cytosolic Protein Delivery by Nanoparticle-Stabilized Nanocapsules. Bioconjug Chem. 2015;26(6):1004-7.
30. Lee Y, Ishii T, Kim HJ, Nishiyama N, Hayakawa Y, Itaka K, et al. Efficient delivery of bioactive antibodies into the cytoplasm of living cells by charge-conversional polyion complex micelles. Angew Chem Int Ed Engl. 2010;49(14):2552-5.
31. Lee Y, Ishii T, Cabral H, Kim HJ, Seo JH, Nishiyama N, et al. Charge-conversional polyionic complex micelles-efficient nanocarriers for protein delivery into cytoplasm. Angew Chem Int Ed Engl. 2009;48(29):5309-12.
32. Kim A, Miura Y, Ishii T, Mutaf OF, Nishiyama N, Cabral H, et al. Intracellular Delivery of Charge-Converted Monoclonal Antibodies by Combinatorial Design of Block/Homo Polyion Complex Micelles. Biomacromolecules. 2016;17(2):446-53.
33. Sarker SR, Hokama R, Takeoka S. Intracellular delivery of universal proteins using a lysine headgroup containing cationic liposomes: deciphering the uptake mechanism. Mol Pharm. 2014;11(1):164-74.
34. Saalik P, Elmquist A, Hansen M, Padari K, Saar K, Viht K, et al. Protein cargo delivery properties of cell-penetrating peptides. A comparative study. Bioconjug Chem. 2004;15(6):1246-53.

35. Nischan N, Herce HD, Natale F, Bohlke N, Budisa N, Cardoso MC, et al. Covalent attachment of cyclic TAT peptides to GFP results in protein delivery into live cells with immediate bioavailability. Angew Chem Int Ed Engl. 2015;54(6):1950-3.
36. Erazo-Oliveras A, Najjar K, Dayani L, Wang TY, Johnson GA, Pellois JP. Protein delivery into live cells by incubation with an endosomolytic agent. Nat Methods. 2014;11(8):861-7.
37. Frankel AD, Pabo CO. Cellular uptake of the tat protein from human immunodeficiency virus 214. Cell. 1988;55:1189-93.
38. Derossi D, Joliot AH, Chassaing G, Prochiantz A. The third helix of the Antennapedia homeodomain translocates through biological membranes 160. J Biol Chem. 1994;269:10444-50.
39. Sawant R, Torchilin V. Intracellular transduction using cell-penetrating peptides. Mol Biosyst. 2010;6(4):628-40.
40. Madani F, Lindberg S, Langel U, Futaki S, Graslund A. Mechanisms of cellular uptake of cell-penetrating peptides. J Biophys. 2011;2011:414729.
41. Kim D, Kim CH, Moon JI, Chung YG, Chang MY, Han BS, et al. Generation of human induced pluripotent stem cells by direct delivery of reprogramming proteins. Cell Stem Cell. 2009;4(6):472-6.
42. Yu M, Lian S, Han H, Yu K, Li G, Lian Z, et al. Four recombinant pluripotency transcriptional factors containing a protein transduction domain maintained the in vitro pluripotency of chicken embryonic stem cells. Sci China Life Sci. 2013;56(1):40-50.
43. Liu J, Gaj T, Patterson JT, Sirk SJ, Barbas Iii CF. Cell-Penetrating Peptide-Mediated Delivery of TALEN Proteins via Bioconjugation for Genome Engineering. PLoS One. 2014;9(1):e85755.
44. June RK, Gogoi K, Eguchi A, Cui XS, Dowdy SF. Synthesis of a pH-Sensitive Nitrilotriacetic Linker to Peptide Transduction Domains To Enable Intracellular Delivery of Histidine Imidazole Ring-Containing Macromolecules. J Am Chem Soc. 2010;132(31):10680-2.
45. Hartmann L, Krause E, Antonietti M, Borner HG. Solid-phase supported polymer synthesis of sequence-defined, multifunctional poly(amidoamines). Biomacromolecules. 2006;7(4):1239-44.
46. Schaffert D, Badgujar N, Wagner E. Novel Fmoc-polyamino acids for solid-phase synthesis of defined polyamidoamines. Org Lett. 2011;13(7):1586-9.
47. Martin I, Dohmen C, Mas-Moruno C, Troiber C, Kos P, Schaffert D, et al. Solid-phase-assisted synthesis of targeting peptide-PEG-oligo(ethane amino)amides for receptor-mediated gene delivery. Org Biomol Chem. 2012;10(16):3258-68.
48. Schaffert D, Troiber C, Salcher EE, Frohlich T, Martin I, Badgujar N, et al. Solid-phase synthesis of sequence-defined T-, i-, and U-shape polymers for pDNA and siRNA delivery. Angew Chem Int Ed Engl. 2011;50(38):8986-9.
49. Wojcik F, Mosca S, Hartmann L. Solid-phase synthesis of asymmetrically branched sequence-defined poly/oligo(amidoamines). J Org Chem. 2012;77(9):4226-34.
50. Fröhlich T, Edinger D, Kläger R, Troiber C, Salcher E, Badgujar N, et al. Structure-activity relationships of siRNA carriers based on sequence-defined oligo (ethane amino) amides. J Control Release. 2012;160(3):532-41.
51. Salcher EE, Kos P, Frohlich T, Badgujar N, Scheible M, Wagner E. Sequence-defined four-arm oligo(ethanamino)amides for pDNA and siRNA delivery: Impact of building blocks on efficacy. J Control Release. 2012;164(3):380-6.
52. Maier K, Martin I, Wagner E. Sequence Defined Disulfide-Linked Shuttle for Strongly Enhanced Intracellular Protein Delivery. Mol Pharm. 2012;9(12):3560-8.

53. Zhang P, He D, Klein PM, Liu X, Röder R, Döblinger M, et al. Enhanced Intracellular Protein Transduction by Sequence Defined Tetra-Oleoyl Oligoaminoamides Targeted for Cancer Therapy. Adv Funct Mater. 2015;25(42):6627–36.
54. Maier K, Wagner E. Acid-labile traceless click linker for protein transduction. J Am Chem Soc. 2012;134(24):10169-73.
55. Lee Y, Fukushima S, Bae Y, Hiki S, Ishii T, Kataoka K. A protein nanocarrier from charge-conversion polymer in response to endosomal pH. J Am Chem Soc. 2007;129(17):5362-3.
56. Muyldermans S., Atarhouch T., Saldanha J., Barbosa J.A., Hamers R. Sequence and structure of VH domain from naturally occurring camel heavy chain immunoglobulins lacking light chains. Protein Eng. 1994;7(9):1129-35.
57. Hamers-Casterman C, Atarhouch T, Muyldermans S, Robinson G, Hamers C, Songa EB, et al. Naturally occurring antibodies devoid of light chains. Nature. 1993;363(6428):446-8.
58. Siontorou CG. Nanobodies as novel agents for disease diagnosis and therapy. Int J Nanomedicine. 2013;8:4215-27.
59. Röder R, Helma J, Preiss T, Radler JO, Leonhardt H, Wagner E. Intracellular Delivery of Nanobodies for Imaging of Target Proteins in Live Cells. Pharm Res. 2017;34(1):161-174.
60. Broisat A, Hernot S, Toczek J, De Vos J, Riou LM, Martin S, et al. Nanobodies targeting mouse/human VCAM1 for the nuclear imaging of atherosclerotic lesions. Circ Res. 2012;110(7):927-37.
61. Bleck M, Itano MS, Johnson DS, Thomas VK, North AJ, Bieniasz PD, et al. Temporal and spatial organization of ESCRT protein recruitment during HIV-1 budding. Proc Natl Acad Sci U S A. 2014;111(33):12211-6.
62. Rajan M, Mortusewicz O, Rothbauer U, Hastert FD, Schmidthals K, Rapp A, et al. Generation of an alpaca-derived nanobody recognizing gamma-H2AX. FEBS Open Bio. 2015;5:779-88.
63. Kirchhofer A, Helma J, Schmidthals K, Frauer C, Cui S, Karcher A, et al. Modulation of protein properties in living cells using nanobodies. Nat Struct Mol Biol. 2010;17(1):133-8.
64. Rothbauer U, Zolghadr K, Tillib S, Nowak D, Schermelleh L, Gahl A, et al. Targeting and tracing antigens in live cells with fluorescent nanobodies. Nat Methods. 2006;3(11):887-9.
65. Helma J, Cardoso MC, Muyldermans S, Leonhardt H. Nanobodies and recombinant binders in cell biology. J Cell Biol. 2015;209(5):633-44.
66. Dmitriev OY, Lutsenko S, Muyldermans S. Nanobodies as Probes for Protein Dynamics in Vitro and in Cells. J Biol Chem. 2015;291(8):3767-75.
67. Arbabi-Ghahroudi M, Tanha J, MacKenzie R. Prokaryotic expression of antibodies. Cancer Metastasis Rev. 2005;24(4):501-19.
68. Lauwereys M, Arbabi Ghahroudi M, Desmyter A, Kinne J, Holzer W, De Genst E, et al. Potent enzyme inhibitors derived from dromedary heavy-chain antibodies. EMBO J. 1998;17(13):3512-20.
69. Lisy MR, Goermar A, Thomas C, Pauli J, Resch-Genger U, Kaiser WA, et al. In vivo near-infrared fluorescence imaging of carcinoembryonic antigen-expressing tumor cells in mice. Radiology. 2008;247(3):779-87.
70. Rothbauer U, Zolghadr K, Muyldermans S, Schepers A, Cardoso MC, Leonhardt H. A versatile nanotrap for biochemical and functional studies with fluorescent fusion proteins. Mol Cell Proteomics. 2008;7(2):282-9.

71. Heukers R, Altintas I, Raghoenath S, De Zan E, Pepermans R, Roovers RC, et al. Targeting hepatocyte growth factor receptor (Met) positive tumor cells using internalizing nanobody-decorated albumin nanoparticles. Biomaterials. 2014;35(1):601-10.
72. Ekstrand MI, Nectow AR, Knight ZA, Latcha KN, Pomeranz LE, Friedman JM. Molecular profiling of neurons based on connectivity. Cell. 2014;157(5):1230-42.
73. Leduc C, Si S, Gautier J, Soto-Ribeiro M, Wehrle-Haller B, Gautreau A, et al. A highly specific gold nanoprobe for live-cell single-molecule imaging. Nano Lett. 2013;13(4):1489-94.
74. Caussinus E, Kanca O, Affolter M. Fluorescent fusion protein knockout mediated by anti-GFP nanobody. Nat Struct Mol Biol. 2012;19(1):117-21.
75. Peyvandi F, Scully M, Kremer Hovinga JA, Cataland S, Knobl P, Wu H, et al. Caplacizumab for Acquired Thrombotic Thrombocytopenic Purpura. N Engl J Med. 2016;374(6):511-22.
76. Fleischmann R, Nayiager S, Louw I, Rojkovich B, Fu C, Udata C, et al. A Multiple Ascending Dose/Proof of Concept Study of ATN-103 (ozoralizumab) in Rheumatoid Arthritis Subjects on a Background of Methotrexate. [abstract] Arthritis Rheum. 2011;63(10):2630.
77. Hoskins B, Robson R. Infinite polymeric frameworks consisting of three dimensionally linked rod-like segments. J Am Chem Soc. 1989;15(111):5962-4.
78. Ferey G. Hybrid porous solids: past, present, future. Chemical Society Reviews. 2008;37(1):191-214.
79. Furukawa H, Cordova KE, O'Keeffe M, Yaghi OM. The Chemistry and Applications of Metal-Organic Frameworks. Science. 2013;341(6149).
80. Cook TR, Zheng YR, Stang PJ. Metal-organic frameworks and self-assembled supramolecular coordination complexes: comparing and contrasting the design, synthesis, and functionality of metal-organic materials. Chem Rev. 2013;113(1):734-77.
81. Cui Y, Yue Y, Qian G, Chen B. Luminescent functional metal-organic frameworks. Chem Rev. 2012;112(2):1126-62.
82. Ferey G, Serre C, Devic T, Maurin G, Jobic H, Llewellyn PL, et al. Why hybrid porous solids capture greenhouse gases? Chem Soc Rev. 2011;40(2):550-62.
83. He Y, Zhou W, Qian G, Chen B. Methane storage in metal-organic frameworks. Chem Soc Rev. 2014;43(16):5657-78.
84. Liu J, Chen L, Cui H, Zhang J, Zhang L, Su CY. Applications of metal-organic frameworks in heterogeneous supramolecular catalysis. Chem Soc Rev. 2014;43(16):6011-61.
85. Horcajada P, Gref R, Baati T, Allan PK, Maurin G, Couvreur P, et al. Metal-organic frameworks in biomedicine. Chem Rev. 2012;112(2):1232-68.
86. Wuttke S, Braig S, Preiss T, Zimpel A, Sicklinger J, Bellomo C, et al. MOF nanoparticles coated by lipid bilayers and their uptake by cancer cells. Chem Commun (Camb). 2015;51(87):15752-5.
87. Schlesinger M, Schulze S, Hietschold M, Mehring M. Evaluation of synthetic methods for microporous metal–organic frameworks exemplified by the competitive formation of [Cu2(btc)3(H2O)3] and [Cu2(btc)(OH)(H2O)]. Microporous Mesoporous Mater. 2010;132:121–7.
88. Serra-Crespo P, Ramos-Fernandez EV, Gascon J, Freek K. Synthesis and Characterization of an Amino Functionalized MIL-101(Al): Separation and Catalytic Properties. 2011;23:2565–72.

89. Hintz H, Wuttke S. Postsynthetic modification of an amino-tagged MOF using peptide coupling reagents: a comparative study. Chem Commun (Camb). 2014;50(78):11472-5.
90. Ingleson MJ, Barrio JP, Guilbaud JB, Khimyak YZ, Rosseinsky MJ. Framework functionalisation triggers metal complex binding. Chem Commun (Camb). 2008(23):2680-2.
91. Goesmann H, Feldmann C. Nanoparticulate functional materials. Angew Chem Int Ed Engl. 2010;49(8):1362-95.
92. Sanvicens N, Marco MP. Multifunctional nanoparticles--properties and prospects for their use in human medicine. Trends Biotechnol. 2008;26(8):425-33.
93. Jia F, Liu X, Li L, Mallapragada S, Narasimhan B, Wang Q. Multifunctional nanoparticles for targeted delivery of immune activating and cancer therapeutic agents. J Control Release. 2013;172(3):1020-34.
94. Calandra P, Caschera D, Turco Liveri V, Lombardo D. How self-assembly of amphiphilic molecules can generate complexity in the nanoscale. Colloids Surf Physicochem Eng Aspects. 2015;484:164-83.
95. Torchilin VP. Micellar nanocarriers: pharmaceutical perspectives. Pharm Res. 2007;24(1):1-16.
96. Nishiyama N, Matsumura Y, Kataoka K. Development of polymeric micelles for targeting intractable cancers. Cancer science. 2016.
97. Discher BM, Won YY, Ege DS, Lee JC, Bates FS, Discher DE, et al. Polymersomes: tough vesicles made from diblock copolymers. Science. 1999;284(5417):1143-6.
98. Nomoto T, Fukushima S, Kumagai M, Machitani K, Arnida, Matsumoto Y, et al. Three-layered polyplex micelle as a multifunctional nanocarrier platform for light-induced systemic gene transfer. Nat Commun. 2014;5:3545.
99. Tockary TA, Osada K, Motoda Y, Hiki S, Chen Q, Takeda KM, et al. Rod-to-Globule Transition of pDNA/PEG-Poly(l-Lysine) Polyplex Micelles Induced by a Collapsed Balance Between DNA Rigidity and PEG Crowdedness. Small. 2016;12(9):1193-200.
100. Park IK, von Recum HA, Jiang S, Pun SH. Supramolecular assembly of cyclodextrin-based nanoparticles on solid surfaces for gene delivery. Langmuir. 2006;22(20):8478-84.
101. Davis ME. The first targeted delivery of siRNA in humans via a self-assembling, cyclodextrin polymer-based nanoparticle: from concept to clinic. Mol Pharm. 2009;6(3):659-68.
102. Cutler JI, Auyeung E, Mirkin CA. Spherical nucleic acids. J Am Chem Soc. 2012;134(3):1376-91.
103. Rothemund PW. Folding DNA to create nanoscale shapes and patterns. Nature. 2006;440(7082):297-302.
104. Andersen ES, Dong M, Nielsen MM, Jahn K, Subramani R, Mamdouh W, et al. Self-assembly of a nanoscale DNA box with a controllable lid. Nature. 2009;459(7243):73-6.
105. Schreiber R, Do J, Roller EM, Zhang T, Schuller VJ, Nickels PC, et al. Hierarchical assembly of metal nanoparticles, quantum dots and organic dyes using DNA origami scaffolds. Nat Nanotechnol. 2014;9(1):74-8.
106. Mirkin CA, Letsinger RL, Mucic RC, Storhoff JJ. A DNA-based method for rationally assembling nanoparticles into macroscopic materials. Nature. 1996;382(6592):607-9.

107. Beckert L, Kostka L, Kessel E, Levacic AK, Kostkova H, Etrych T, et al. Acid-labile pHPMA modification of four-arm oligoaminoamide pDNA polyplexes balances shielding and gene transfer activity in vitro and in vivo. Eur J Pharm Biopharm. 2016;105:85-96.
108. Muller K, Kessel E, Klein PM, Hohn M, Wagner E. Post-PEGylation of siRNA Lipo-oligoamino Amide Polyplexes Using Tetra-glutamylated Folic Acid as Ligand for Receptor-Targeted Delivery. Mol Pharm. 2016;13(7)2332-45.
109. Zimpel A, Preiß T, Röder R, Engelke H, Ingrisch M, Peller M, et al. Imparting Functionality to MOF Nanoparticles by External Surface Selective Covalent Attachment of Polymers. Chem Mater. 2016;28(10):3318–26.
110. Shih YH, Lo SH, Yang NS, Singco B, Cheng YJ, Wu CY, Chang L, Huang HY, Lin CH. Trypsin-Immobilized Metal−Organic Framework as a Biocatalyst In Proteomics Analysis. Chem Plus Chem. 2012;77:982−6.
111. Jung S, Kim Y, Kim SJ, Kwon TH, Huh S, Park S. Bio-functionalization of metal-organic frameworks by covalent protein conjugation. Chem Commun (Camb). 2011;47(10):2904-6.
112. Moller K, Muller K, Engelke H, Brauchle C, Wagner E, Bein T. Highly efficient siRNA delivery from core-shell mesoporous silica nanoparticles with multifunctional polymer caps. Nanoscale. 2016;8(7):4007-19.
113. Niedermayer S, Weiss V, Herrmann A, Schmidt A, Datz S, Muller K, et al. Multifunctional polymer-capped mesoporous silica nanoparticles for pH-responsive targeted drug delivery. Nanoscale. 2015;7(17):7953-64.
114. Qi X, Rui Y, Fan Y, Chen H, Ma N, Wu Z. Galactosylated chitosan-grafted multiwall carbon nanotubes for pH-dependent sustained release and hepatic tumor-targeted delivery of doxorubicin in vivo. Colloids Surf B Biointerfaces. 2015;133:314-22.
115. Cai L, Wang X, Wang W, Qiu N, Wen J, Duan X, et al. Peptide ligand and PEG-mediated long-circulating liposome targeted to FGFR overexpressing tumor in vivo. Int J Nanomedicine. 2012;7:4499-510.
116. Kibria G, Hatakeyama H, Ohga N, Hida K, Harashima H. Dual-ligand modification of PEGylated liposomes shows better cell selectivity and efficient gene delivery. J Control Release. 2011;153(2):141-8.
117. Baati T, Horcajada P, Gref R, Couvreur P, Serre C. Quantification of fumaric acid in liver, spleen and urine by high-performance liquid chromatography coupled to photodiode-array detection. J Pharm Biomed Anal. 2011;56(4):758-62.
118. Ferey G. Hybrid porous solids: past, present, future. Chem Soc Rev. 2008;37(1):191-214.
119. Xu WT, Ma L, Ke F, Peng FM, Xu GS, Shen YH, et al. Metal-organic frameworks MIL-88A hexagonal microrods as a new photocatalyst for efficient decolorization of methylene blue dye. Dalton Trans. 2014;43(9):3792-8.
120. Li K-YA, Chang H-A, Hsu C-J. Iron-based metal organic framework, MIL-88A, as a heterogeneous persulfate catalyst for decolorization of Rhodamine B in water. RCS Advances. 2015;5:32520–30.
121. Horcajada P, Chalati T, Serre C, Gillet B, Sebrie C, Baati T, et al. Porous metal-organic-framework nanoscale carriers as a potential platform for drug delivery and imaging. Nat Mater. 2010;9(2):172-8.
122. Chui SS, Lo SM, Charmant JP, Orpen AG, Williams ID. A chemically functionalizable nanoporous material. Science. 1999;283(5405):1148-50.
123. Mueller U, Schubert M, Teich F, Puetter H, Schierle-Arndt K, Pastré J. Metal–organic frameworks—prospective industrial applications. J Mater Chem. 2006;16:626-36

124. Conde-Gonzalez JE, Pena-Mendez EM, Rybakova S, Pasan J, Ruiz-Perez C, Havel J. Adsorption of silver nanoparticles from aqueous solution on copper-based metal organic frameworks (HKUST-1). Chemosphere. 2016;150:659-66.
125. Ke F, Yuan Y-P, Qiu L-G, Shen Y-H, Xie A-J, Zhu J-F, et al. Facile fabrication of magnetic metal–organic framework nanocomposites for potential targeted drug deliver. J Mater Chem. 2010;21:3843–384.
126. Xu Q, Li S, Huang H, Wen J. Key technologies for the industrial production of fumaric acid by fermentation. Biotechnol Adv. 2012;30(6):1685-96.
127. Cavka JH, Jakobsen S, Olsbye U, Guillou N, Lamberti C, Bordiga S, et al. A new zirconium inorganic building brick forming metal organic frameworks with exceptional stability. J Am Chem Soc. 2008;130(42):13850-1.
128. Schaate A, Roy P, Godt A, Lippke J, Waltz F, Wiebcke M, et al. Modulated synthesis of Zr-based metal-organic frameworks: from nano to single crystals. Chemistry (Easton). 2011;17(24):6643-51.
129. Wißmann G, Schaate A, Lilienthal S, Bremer I, Schneider AM, Behrens P. Modulated Synthesis of Zr-fumarate MOF. Microporous Mesoporous Mater. 2012;152: 64-70
130. Wang B, Lv XL, Feng D, Xie LH, Zhang J, Li M, et al. Highly Stable Zr(IV)-Based Metal-Organic Frameworks for the Detection and Removal of Antibiotics and Organic Explosives in Water. J Am Chem Soc. 2016;138(19):6204-16.
131. Wang C, Xie Z, deKrafft KE, Lin W. Doping metal-organic frameworks for water oxidation, carbon dioxide reduction, and organic photocatalysis. J Am Chem Soc. 2011;133(34):13445-54.
132. Aoning W, Yingjie Z, Zhoulu W, Miao C, Luyi S, Xiang L. Titanium incorporated with UiO-66(Zr)-type Metal–Organic Framework (MOF) for photocatalytic application. RSC Adv. 2016;6:3671-9
133. Lin Q, Bu X, Kong A, Mao C, Zhao X, Bu F, et al. New heterometallic zirconium metalloporphyrin frameworks and their heteroatom-activated high-surface-area carbon derivatives. J Am Chem Soc. 2015;137(6):2235-8.
134. Rasero-Almansa AM, Corma A, Iglesias M, Sánchez F. Post-functionalized iridium – Zr-MOF as a promising recyclable catalyst for the hydrogenation of aromatics. Green Chem. 2014;16:3522-7.
135. Vermoortele F, Bueken B, Le Bars G, Van de Voorde B, Vandichel M, Houthoofd K, et al. Synthesis modulation as a tool to increase the catalytic activity of metal-organic frameworks: the unique case of UiO-66(Zr). J Am Chem Soc. 2013;135(31):11465-8.
136. Zhu X, Gu J, Wang Y, Li B, Li Y, Zhao W, et al. Inherent anchorages in UiO-66 nanoparticles for efficient capture of alendronate and its mediated release. Chem Commun (Camb). 2014;50(63):8779-82.
137. Filippousi M, Turner S, Leus K, Siafaka PI, Tseligka ED, Vandichel M, et al. Biocompatible Zr-based nanoscale MOFs coated with modified poly(epsilon-caprolactone) as anticancer drug carriers. Int J Pharm. 2016;509(1-2):208-18.
138. Leonhardt H, Rahn HP, Weinzierl P, Sporbert A, Cremer T, Zink D, et al. Dynamics of DNA replication factories in living cells. J Cell Biol. 2000;149(2):271-80.
139. Chalati T, Horcajada P, Gref R, Couvreur P. Optimisation of the synthesis of MOF nanoparticles made of flexible porous iron fumarate MIL-88A. J Mater Chem. 2011;21:2220-7.
140. Huo J, Brightwell M, Hankari ES, Garai A, Bradshaw D. A versatile, industrially relevant, aqueous room temperature synthesis of HKUST-1 with high space-time yield. J Mater Chem. 2013;1:15220–3.

141. Lachelt U, Kos P, Mickler FM, Herrmann A, Salcher EE, Rodl W, et al. Fine-tuning of proton sponges by precise diaminoethanes and histidines in pDNA polyplexes. Nanomedicine. 2014;10(1):35-44.
142. He D, Muller K, Krhac Levacic A, Kos P, Lachelt U, Wagner E. Combinatorial Optimization of Sequence-Defined Oligo(ethanamino)amides for Folate Receptor-Targeted pDNA and siRNA Delivery. Bioconjug Chem. 2016;27(3):647-59.
143. He D. Combinatorial optimization of nucleic acid carriers for folate-targeted delivery: LMU München; 2016.
144. Schwille P, Meyer-Almes FJ, Rigler R. Dual-color fluorescence cross-correlation spectroscopy for multicomponent diffusional analysis in solution. Biophys J. 1997;72(4):1878-86.
145. Foo YH, Naredi-Rainer N, Lamb DC, Ahmed S, Wohland T. Factors affecting the quantification of biomolecular interactions by fluorescence cross-correlation spectroscopy. Biophys J. 2012;102(5):1174-83.
146. Wu B, Chen Y, Muller JD. Fluorescence correlation spectroscopy of finite-sized particles. Biophys J. 2008;94(7):2800-8.
147. Vincke C, Muyldermans S. Introduction to heavy chain antibodies and derived Nanobodies. Methods Mol Biol. 2012;911:15-26.
148. Scholz C, Kos P, Wagner E. Comb-like oligoaminoethane carriers: change in topology improves pDNA delivery. Bioconjug Chem. 2014;25(2):251-61.
149. Chiu HY, Deng W, Engelke H, Helma J, Leonhardt H, Bein T. Intracellular chromobody delivery by mesoporous silica nanoparticles for antigen targeting and visualization in real time. Sci Rep. 2016;6:25019.
150. Magde D, Elson E, Webb W.W. Thermodynamic Fluctuations in a Reacting System-Measurement by Fluorescence Correlation Spectroscopy. Phys Rev Lett. 1972;29(11):707-8.
151. Zhu H, Derksen R, Krause C, Fox R, Brazee R, Ozkan H. Fluorescent Intensity of Dye Solutions under Different pH Conditions. ASTM International. 2005;2(6):1-7.
152. Zhou HC, Kitagawa S. Metal-organic frameworks (MOFs). Chem Soc Rev. 2014;43(16):5415-8.
153. Zhou HC, Long JR, Yaghi OM. Introduction to metal-organic frameworks. Chem Rev. 2012;112(2):673-4.
154. Block H, Maertens B, Spriestersbach A, Brinker N, Kubicek J, Fabis R, et al. Immobilized-metal affinity chromatography (IMAC): a review. Methods Enzymol. 2009;463:439-73.
155. Hochuli E, Bannwarth W, Döbeli H, Gentz R, D S. Genetic Approach to Facilitate Purification of Recombinant Proteins with a Novel Metal Chelate Adsorben. Nat Biotechnol. 1988;6:1321 - 5.
156. Wieneke R, Laboria N, Rajan M, Kollmannsperger A, Natale F, Cardoso MC, et al. Live-cell targeting of his-tagged proteins by multivalent N-nitrilotriacetic acid carrier complexes. J Am Chem Soc. 2014;136(40):13975-8.
157. Postupalenko V, Desplancq D, Orlov I, Arntz Y, Spehner D, Mely Y, et al. Protein Delivery System Containing a Nickel-Immobilized Polymer for Multimerization of Affinity-Purified His-Tagged Proteins Enhances Cytosolic Transfer. Angew Chem Int Ed Engl. 2015;54(36):10583-6.
158. Röder R, Preiss T, Hirschle P, Steinborn B, Zimpel A, Hohn M, et al. Multifunctional Nanoparticles by Coordinative Self-Assembly of His-Tagged Units with Metal-Organic Frameworks. J Am Chem Soc. 2017;139(6):2359-68.

159. Dietl C, Hintz H, Ruhle B, Schmedt Auf der Gunne J, Langhals H, Wuttke S. Switch-On Fluorescence of a Perylene-Dye-Functionalized Metal-Organic Framework through Postsynthetic Modification. Chemistry (Easton). 2015;21(30):10714-20.
160. Wuttke S, Dietl C, Hinterholzinger FM, Hintz H, Langhals H, Bein T. Turn-on fluorescence triggered by selective internal dye replacement in MOFs. Chem Commun (Camb). 2014;50(27):3599-601.
161. Martin R, Edsall J. The Association of Divalent Cations with Acylated Histidine Derivatives. J Am Chem Soc. 1960;82(5):1107–11.
162. Bangham AD, Standish MM, Watkins JC. Diffusion of univalent ions across the lamellae of swollen phospholipids. J Mol Biol. 1965;13(1):238-52.
163. Gabizon A, Shmeeda H, Barenholz Y. Pharmacokinetics of pegylated liposomal Doxorubicin: review of animal and human studies. Clin Pharmacokinet. 2003;42(5):419-36.
164. Allen TM, Cullis PR. Liposomal drug delivery systems: from concept to clinical applications. Adv Drug Deliv Rev. 2013;65(1):36-48.
165. Yingchoncharoen P, Kalinowski DS, Richardson DR. Lipid-Based Drug Delivery Systems in Cancer Therapy: What Is Available and What Is Yet to Come. Pharmacol Rev. 2016;68(3):701-87.
166. Vemuri S, Rhodes CT. Preparation and characterization of liposomes as therapeutic delivery systems: a review. Pharm Acta Helv. 1995;70(2):95-111.
167. Ellens H, Bentz J, Szoka FC. Fusion of phosphatidylethanolamine-containing liposomes and mechanism of the L alpha-HII phase transition. Biochemistry. 1986;25(14):4141-7.
168. Simoes S, Slepushkin V, Duzgunes N, Pedroso de Lima MC. On the mechanisms of internalization and intracellular delivery mediated by pH-sensitive liposomes. Biochim Biophys Acta. 2001;1515(1):23-37.
169. Boeckle S, Fahrmeir J, Roedl W, Ogris M, Wagner E. Melittin analogs with high lytic activity at endosomal pH enhance transfection with purified targeted PEI polyplexes. J Control Release. 2006;112(2):240-8.
170. Werkmeister JA, Hewish DR, Kirkpatrick A, Rivett DE. Sequence requirements for the activity of membrane-active peptides. J Pept Res. 2002;60(4):232-8.
171. Midoux P, Monsigny M. Efficient gene transfer by histidylated polylysine/pDNA complexes. Bioconjug Chem. 1999;10(3):406-11.
172. Li R, Boehm AL, Miranda MB, Shangary S, Grandis JR, Johnson DE. Targeting antiapoptotic Bcl-2 family members with cell-permeable BH3 peptides induces apoptosis signaling and death in head and neck squamous cell carcinoma cells. Neoplasia. 2007;9(10):801-11.
173. Javadpour MM, Juban MM, Lo WC, Bishop SM, Alberty JB, Cowell SM, et al. De novo antimicrobial peptides with low mammalian cell toxicity. J Med Chem. 1996;39(16):3107-13.
174. Ellerby HM, Arap W, Ellerby LM, Kain R, Andrusiak R, Rio GD, et al. Anti-cancer activity of targeted pro-apoptotic peptides. Nat Med. 1999;5(9):1032-8.
175. Bratton SB, Salvesen GS. Regulation of the Apaf-1-caspase-9 apoptosome. J Cell Sci. 2010;123(Pt 19):3209-14.
176. Frohlich T, Edinger D, Russ V, Wagner E. Stabilization of polyplexes via polymer crosslinking for efficient siRNA delivery. Eur J Pharm Sci. 2012;47(5):914-20.
177. Taratula O, Garbuzenko OB, Kirkpatrick P, Pandya I, Savla R, Pozharov VP, et al. Surface-engineered targeted PPI dendrimer for efficient intracellular and intratumoral siRNA delivery. J Control Release. 2009;140(3):284-93.

178. Dohmen C, Edinger D, Frohlich T, Schreiner L, Lachelt U, Troiber C, et al. Nanosized Multifunctional Polyplexes for Receptor-Mediated SiRNA Delivery. ACS nano. 2012;6(6):5198-208.
179. Troiber C, Kasper JC, Milani S, Scheible M, Martin I, Schaubhut F, et al. Comparison of four different particle sizing methods for siRNA polyplex characterization. Eur J Pharm Biopharm. 2013;84(2):255-64.
180. Lachelt U, Wagner E. Nucleic Acid Therapeutics Using Polyplexes: A Journey of 50 Years (and Beyond). Chem Rev. 2015;115(19):11043-78.
181. Orellana-Tavra C, Mercado SA, Fairen-Jimenez D. Endocytosis Mechanism of Nano Metal-Organic Frameworks for Drug Delivery. Adv Healthc Mater. 2016;5(17):2261-70.

8 Acknowledgements

Over the past years many people in and outside of the lab contributed to the success of this thesis.

First I want to thank Prof. Dr. Ernst Wagner, for giving me the opportunity to work on my thesis in his group. I very much appreciate his professional guidance, scientific support and trust. Encouraging me to gain expertise in various disciplines, especially to also broaden my chemical horizon.

A special thank you to Prof. Dr. Heinrich Leonhardt and Dr. Jonas Helma, for the collaboration with the nanobody project.

A big thank you to Dr. Ulrich Lächelt for the great productive collaboration in the MOF project and the plenty of helpful discussions. I would also like to thank Dr. Stefan Wuttke and the other members of the “MOF team”, Tobias Preiß, Patrick Hirschle, Benjamin Steinborn and Andreas Zimpel, for the many afternoons spend together in hot tempered, but always fruitful scientific discussions.

Special thanks to Tobi for the afternoons spend together measuring FCS and being happy to change colours in diagrams immediately no matter how many times I asked.

Many thanks to Philipp K. and the former lab members Dongsheng, Claudia and Edith for their supply with oligomers, without which, the nanobody project would not have been possible.

My gratitude goes to Wolfgang for solving every technical problem immediately, no matter how busy he was. Thank you to Miriam, for introducing me to the confocal microscope teaching me more patience. Also thank you for the almost weekly maintenance of the FACS machine.

Many thanks to Dr. Martina Rüffer for the organization of hiking trips, “Weißwurstfrühstück”, great Christmas parties and the chocolate at Nicolaus.

A big thank you to Ursual, Anna and Melinda for keeping the lab running and distraction from the daily routine always putting a smile on my face.

Thank you to Linda, for climbing Mount AzMMMan with me, learning how to use the kugelrohr destille by youtube and spending many happy hours in and outside of the lab.

Special thanks to Katharina, for not only becoming a good colleague and lab neighbour, but also a dear friend outside of the lab. I hope our sporting and hiking trips will continue!

I also want to thank my other lab neighbours Philipp H., Petra, Ana and Adam for the great working atmosphere. A big thank you of course also goes to all the other old, new and newer members of the AK Wagner. I really had a great time with all of you in and outside of the lab!!

Most of all I have to thank Ludwig and all my other friends outside of the lab for always being there for me, listening to more or less boring research stories but still giving great advice and supporting me. Last but not least my deepest gratitude goes to my parents who have always supported me. Without you this would not have been possible!